Graduate School ETD Form 9
(Revised 12/07)

PURDUE UNIVERSITY
GRADUATE SCHOOL
Thesis/Dissertation Acceptance

This is to certify that the thesis/dissertation prepared

By KAI LIU

Entitled
CONCURRENT TOPOLOGY OPTIMIZATION OF STRUCTURES AND MATERIALS

For the degree of Master of Science in Engineering

Is approved by the final examining committee:

Andrés Tovar
Chair

Khosrow Nematollahi

Sarah Koskie

To the best of my knowledge and as understood by the student in the *Research Integrity and Copyright Disclaimer (Graduate School Form 20)*, this thesis/dissertation adheres to the provisions of Purdue University's "Policy on Integrity in Research" and the use of copyrighted material.

Approved by Major Professor(s): Andrés Tovar

Approved by: Sohel Anwar 07/15/2013
Head of the Graduate Program Date

CONCURRENT TOPOLOGY OPTIMIZATION OF STRUCTURES AND MATERIALS

A Thesis

Submitted to the Faculty

of

Purdue University

by

Kai Liu

In Partial Fulfillment of the

Requirements for the Degree

of

Master of Science in Engineering

August 2013

Purdue University

Indianapolis, Indiana

To my beloved Kai-Wen Chiu, who is always supportive and radiantly beautiful.

ACKNOWLEDGMENTS

I owe my deepest appreciation to my advisor, Professor Andrés Tovar, who has the attitude and the substance of a genius: he constantly and convincingly conveyed a spirit of adventure in regard to research and scholarship, and an enjoyment in regard to teaching. Without his guidance and persistent help this dissertation would not have been possible.

I would like to thank my committee members, Professor Sarah Koskie and Professor Khosrow Nematollahi serving as my committee members. I also want to thank you for letting my defense be a pleasant moment, and for your brilliant comments and suggestions, thanks to you.

I am indebted to my many colleagues, Mr. Satyajeet Shinde, Mr. Kunal R. Khadke, Mr. Joshua J. Israel, Ms. Anahita Emami and Dr. Weigang An, who supported me this year.

Moreover, a special thank to Mr. Frank M. Smith IV from University Writing Center, who help me with the grammar and language usage in this dissertation.

Last but not least, I cannot find words to express my gratitude to my parents who have given me the opportunity of an education from the best institutions and support throughout my life.

TABLE OF CONTENTS

Page

LIST OF TABLES

LIST OF FIGURES

LIST OF SYMBOLS

$\mathbf{B}$	macro-scale finite element strain-displacement matrix
$\mathbf{b}$	meso-scale finite element strain-displacement matrix
C_{ijkl}	elastic tensor
C^{H}_{ijkl}	effective elastic tensor
$\mathbf{C}$	constitutive matrix
$\mathbf{C}^{\mathrm{H}}$	effective stiffness matrix
$[\mathbf{C}^{\mathrm{H}}]^0$	homogenized effective tensor with unit elastic modulus
E_0	base materials elastic modulus
$\mathrm{E}_i(x_i)$	modified PAMP interpolation scheme
E_j	element elastic modulus
$\mathrm{E}_j(y_j)$	modified SIMP interpolation scheme
$\mathrm{E}_{\min}$	stiffness of soft (void) materials
e	element index
$\mathbf{F}$	body force
f_{in}	input load
f_Y	meso-scale volume fraction
f_Ω	macro-scale volume fraction
$\mathbf{f}^{kl}$	force vector corresponding to the homogenization procedure
$g(\cdot)$	unequally constraint
$\mathbf{K}^{\mathrm{H}}$	homogenized global stiffness matrix
$\mathbf{K}^{\mathrm{H}}_i$	homogenized element stiffness matrix
$[\mathbf{K}^{\mathrm{H}}_i]^0$	homogenized element stiffness matrix with unit elastic modulus
k	iteration number
$\mathbf{k}$	global stiffness matrix on meso-scale
$\mathbf{k}_j$	element stiffness matrix on meso-scale

$L_e^{(k)}$	lower asymptotes for element e at iteration k
$\mathbf{L}$	unit length vector with zeros in all dimensions except for one at the output port
M_{nd}	measure of discreteness
N	number of element used to discritize the macro-scale design domain
n	number of element used to discritize the meso-scale design domain
$\text{OBJ}_{\text{multi}}$	multi-level design objective value
OBJ_{uni}	uni-level design objective value
p	penalization power of PAMP
$p^{\max}$	maximum penalization power
$r_{\min}$	filter size
s_0	distance of the asymptotes from current point
$\mathbf{t}$	body traction
U	kinematically admissible displacement fields
$U_e^{(k)}$	upper asymptotes for element e at iteration k
$\mathbf{U}$	displacement fields on macro-scale
$\mathbf{U}_d$	virtual displacement field caused by the dummy load
$\mathbf{U}_{di}$	element virtual displacement field caused by the dummy load
$\mathbf{U}_i$	element displacement vector
u_{out}	output port displacement
V_Y	total amount of base materials in meso-scale
V_Ω	total amount of composite materials in macro-scale
v_i	volume of each element on macro-scale
v_j	volume of each element on meso-scale
$\bar{X}_e$	physical density
$\tilde{X}_e$	standard density filter
$\mathbf{X}$	design variables of optimization problem
x_i	macro-scale element density

$\bar{x}$	upper boundary of macro-scale design varialbes
$\underline{x}$	lower boundary of macro-scale design variables
$\mathbf{x}^{(k)}$	macro-scale design domain of k^{th} iteration
Y	meso-scale design domain
Y_0	volume of meso-scale design domain
Y_e	final volume occupying the meso-scale design domain
$\bar{Y}$	upper boundary on the volume fraction of meso-scale design domain
y_j	meso-scale element density
$\underline{y}$	lower boundary of meso-scale design variables
$\mathbf{y}^i$	meso-scale design variables
$\mathbf{y}^{(k)}$	meso-scale design domain of k^{th} iteration
β	smothing parameter
$\beta_{\max}$	maximum value of smoothing parameter
$\boldsymbol{\chi}^{0(kl)}$	displacement corresponding to the test strains
$\boldsymbol{\chi}^{kl}$	characteristic displacement field
$\epsilon(\cdot)$	linearized strains
$\epsilon^{0(kl)}$	test strains corresponding to the homogenization procedure
ε	the ratio of meso-scale dimension to macro-scale dimension
η	penalization power of SIMP
ν	base materials Poisson's ratio
Ω	macro-scale design domain
Ω_0	volume of macro-design domain
Ω_e	final volume occupying the macro-scale design domain
$\bar{\Omega}$	upper boundary on the volume fraction of macro-scale design domain
ω	weight factor
σ	the stress field due to input load
σ_d	the stress field produced by a unit dummy load

$\mathcal{A}$	finite element assembly operator
$\mathcal{I}$	information from macro-scale
$\mathcal{P}$	structure properties
$\mathcal{P}_i$	element properties
$\mathcal{S}$	quad-4 element shape function

LIST OF ABBREVIATIONS

BESO	Bidirectional Evolutionary Structural Optimization
ESO	Evolutionary Structural Optimization
FE	Finite Elements
FEA	Finite Elements Analysis
FGM	Functionally Graded Materials
FMO	Free Material Optimization
GA	Genetic Algorithms
HCA	Hybrid Cellular Automation
MBB	Messerschmitt-Bölkow-Blohm
MMA	Method of Moving Asymptotes
MPE	Mutual Potential Energy
Obj.	Objective value
OC	Optimality Criteria
PAMP	Porous Anisotropic Material with Penalization
RTPDEM	Robust Topological Preliminary Design Exploration Method
SA	Simulated Annealing
SE	Strain Energy
SIMP	Solid Isotropic Material with Penalization

ABSTRACT

Liu, Kai. M.S.E., Purdue University, August 2013. Concurrent Topology Optimization of Structures and Materials. Major Professor: Andrés Tovar.

Topology optimization allows designers to obtain lightweight structures considering the binary distribution of a solid material. The introduction of cellular material models in topology optimization allows designers to achieve significant weight reductions in structural applications. However, the traditional topology optimization method is challenged by the use of cellular materials. Furthermore, increased material savings and performance can be achieved if the material and the structure topologies are concurrently designed. Hence, multi-scale topology optimization methodologies are introduced to fulfill this goal. The objective of this investigation is to discuss and compare the design methodologies to obtaining optimal macro-scale structures and the corresponding optimal meso-scale material designs in continuum design domains. These approaches make use of homogenization theory to establish communication bridges between both material and structural scales. The periodicity constraint makes such cellular materials manufacturable while relaxing the periodicity constraint to achieve major improvements of structural performance. Penalization methods are used to obtain binary solutions in both scales. The proposed methodologies are demonstrated in the design of stiff structure and compliant mechanism synthesis. The multiscale results are compared with the traditional structural-level designs in the context of Pareto solutions, demonstrating benefits of ultra-lightweight configurations. Errors involved in the mult-scale topology optimization procedure are also discussed. Errors are mainly classified as mesh refinement errors and homogenization errors. Comparisons between the multi-level designs and uni-level designs of solid structures, structures using periodic cellular materials and non-periodic cellular

materials are provided. Error quantifications also indicate the superiority of using non-periodic cellular materials rather than periodic cellular materials.

1. INTRODUCTION

1.1 Justifications

Any structure designer with responsibility and wisdom understands that 'the lighter, the better'. For example, comparisons a box girder bridge made of concrete, a truss bridge welded bars, and a suspension bridge with tensioned cables, we can instantaneously realize that a suspension bridge is the lightest. The following discusses why lightweight structures are worth the effort studying and improving before we consider how to design lightweight structures:

- From an ecological point of view: lightweight structures efficiently use all materials. Thus no materials are wasted.
- From a social point of view: implementing lightweight structures can provide more job opportunities. The design of filigree structures requirements of the labor-intensive careful design in the details spent a lot of expense during preparation and manufacturing.
- From a cultural point of view: using lightweight structures may greatly contribute to the enrichment of architecture. Lightweight structures bring more pleasure through the availability of creating innovation structures than heavy, bulky structures. These lightweight structures may help us to escape from the tedium of today's duplicated engineering structures, which is an important component of the architectural culture.

1.2 State of the Art

Structural optimization can be categorized into three classes: size optimization, shape optimization and topology optimization. Size optimization is aimed at finding

an ideal set of component parameters, such as material properties and dimensions (thickness, width, height, moment of inertia, torsional constant of cross-section). According to the performance target and the boundary conditions, it is targeted to determine the desired thickness of materials expected to be placed on the component. Shape optimization derives the optimal geometric structure in that it minimizes a certain objective function while satisfying prescribed constraints. Typically, the solution of the objective function given by the solution of a given variable domain is defined on partial differential equations. Topology optimization finds the optimal material distribution within a prescribed design domain. For a given set of boundary and loading conditions, topology optimization drives the material distribution process to a structural layout that maximizes performance objectives and satisfies design constraints. In comparison with size and shape optimization, topology optimization is more efficient to design and may generate the optimum structure layout requisite in the stage of initial design. In an optimization process, size optimization and/or shape optimization are fine tuned for performance and manufacturability. Engineers using topology optimization can not only reduce design development time and overall cost, but also improve structure performance.

1.2.1 Topology Optimization

Topology optimization distributes the materials within a design domain that minimizing a certain cost function while satisfying a given set of boundary conditions. The initial work in topology optimization can be tracked back in the seminal work proposed by Bendsøe et al. [2], which is referred to as micro- structure or homogenization based approach. In their work, the recommended strategy was to consider simple square voids at the micro-scale in the context of minimum compliance design. Similar approach was extended to other applications, such as design of the compliant mechanism by Nishiwaki et al. [3]. Another approach is called the density based approach. In this approach, the topology optimization problem is parameterized by the

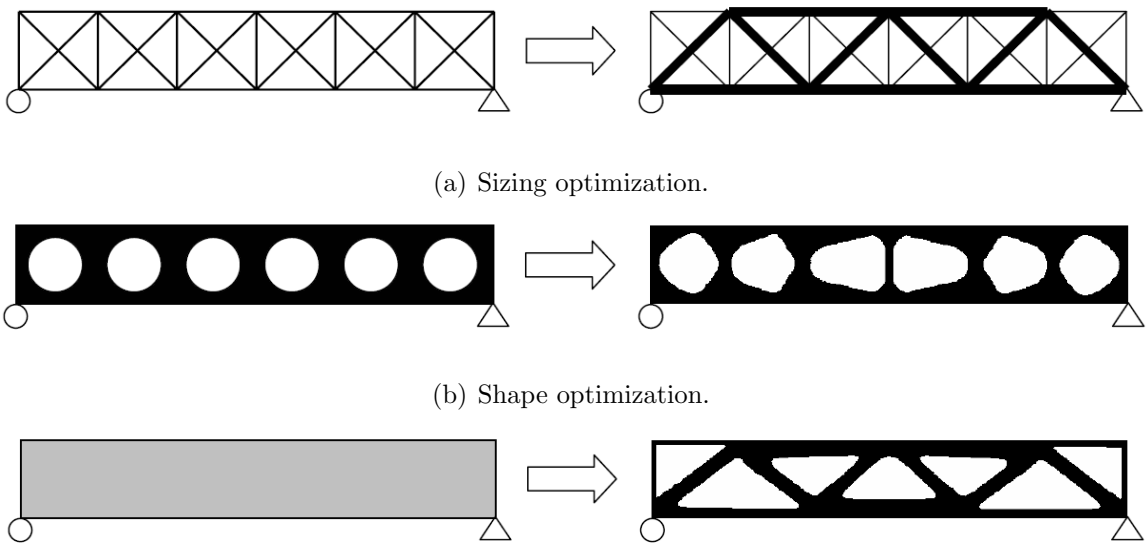

(a) Sizing optimization.

(b) Shape optimization.

(c) Topology optimization.

Figure 1.1. Categories of structural optimization [1].

elastic modulus E_j of the discretized design domain. At the end of the optimization, designers are hoping to achieve black-and-white structures. Those regions with materials have elastic modulus $E_j = E_0$ and regions without materials (with soft materials) have elastic modulus $E_j = E_{\min} \approx 0$. The intermediate value for the elastic modulus is penalized to be close to either 0 or 1. One of the most efficient and widely used techniques is the so-called Solid Isotropic Material with Penalization (SIMP) method which will be briefly reviewed in the next chapter.

Topology optimization usually involves innumerable design variables. Even for a small-scale problem, leads to a very large combinational problem, which is difficult to solve. For example, for a small number of elements used to discretize the design domain with 50 elements, and each element can be either 0 or 1, then the number of combinations would be $2^{50} = 1.13 \times 10^{15}$. In some cases, the penalization method (SIMP) does not apply, which means the element densities could be any number in the range over $]0, 1]$, so the combinations would be astronomical. Conventional optimization algorithms may not solve this type of problem efficiently within a suitable

time. Therefore, using random search methods such as Genetic Algorithms (GA) or Simulated Annealing (SA) methods to solve those problems is impossible. But if the sensitivity of the objective function with respect to (w.r.t) the design variables can be expressed analytically, mathematical programming methods can solve this type of problem efficiently. Several algorithms have been proposed to solve topology optimization problems, such as Method of Moving Asymptotes (MMA) [4, 5], Optimality Criteria (OC) method [6], Evolutionary Structural Optimization (ESO) or Bidirectional Evolutionary Structural Optimization (BESO) [7, 8], level set methods [9,10], and Hybrid Cellular Automation (HCA) method [11,12]. The final goal of the optimization is to choose optimal element densities either 1 or 0; in other words, black-and-white topology.

Topology optimization in composite materials design acts as an important alternative to classic materials design procedures. The structural design is closely related to the design of meso-structural composites via the direct homogenization theory [13,14]. In contrast, the inverse homogenization is a topology optimization procedure, that obtains material distribution of micro-/meso-scale with desired homogenized or effective material properties. Since it has been proposed by Sigmund [15], the inverse homogenization method has been applied for numerous different applications, such as maximum stiffness/minimum compliance [1,16,17], thermal/electrical conduction, dielectrics, magnetic diffusion and gas/fluidic permeation [18–21], material with negative Poisson's ration [15, 22, 23], etc. Functionally Graded Materials (FGM), which are continuously graded in one or more specified directions [24, 25], and has been adapted for multi-functional composites design recently (c.f. [26], [27] and references therein).

1.2.2 Multi-scale Topology Optimization

Generally, there are two scales involved in multi-scale topology optimization: macro-scale and meso/micro-scale, e.g. Fig. 1.2: an example of hierarchical 3D topol-

ogy optimization [28]. The macro-scale (structural design) corresponds to finding the optimal material distribution on the macroscopic level for a prescribed design space and a given set of boundary and loading conditions. On the other hand, the meso/micro-scale (material design) is targeted to find the optimal material meso/micro-structures. The basic concept of multi-scale topology optimization is shwon in Fig. 1.3, assuming the design variable of a macro-structure is $\mathbf{x}$ and the property(-ies) $\mathcal{P}$ of a macro-structure, that information is given to the meso/micro-scale as targets. In the meso/micro-scale, the objectives are to minimize the differences between meso/micro-structure properties and targets. Finally, the optimized meso/micro-structure properties are sent back to the macro-scale. In the example shown in Fig. 1.2, designers want to minimize the structural compliance. The target $\mathcal{P}^*$ in this case is the minimum value of compliance, which is zero compliant. The respond from micro-scale is the optimized elemental compliance.

Many researchers are working on the multi-scale material design aim to find better material design for structural performance. For example, Seepersad [29] who introduced a Robust Topological Preliminary Design Exploration Method (RTPDEM) for heat exchanger and combustor liner design, the optimal material meso-structure achieved by the ground structure topology optimization, and the optimized topology satisfied the predefined multi-functional performance goals and requirements. Also in Wang's works [30], a unit truss cell approach was proposed for lightweight structure and compliant mechanism. Stolpe et al. [31], minimized structural weight under displacement and microscopic stress constraints. Most recently Schury et al. [32] proposed an efficient hierarchical topology optimization procedure with manufacturable constraint. Andreasen et al. [33] proposed a design methodology for optimal poroelastic actuators. Xu et al. [34] introduced a two-scale design optimization for the filtration and chemical engineering industry whose objective is to optimize structural compliance with prescribed seepage flow rate and material porosity constraints. One should note that the multi-scale optimization methods mentioned above are actually micro-/meso-scale material structure design optimization problems using macro-scale

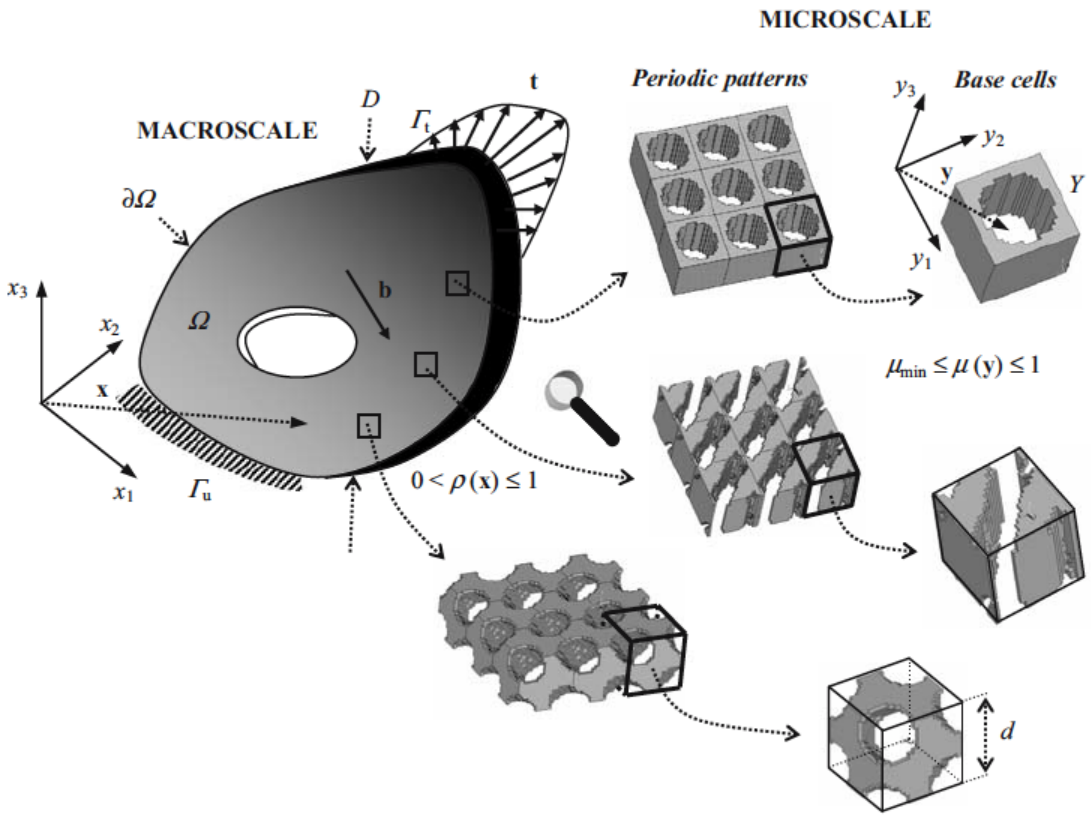

Figure 1.2. Multi-scale topology optimization example in [28].

objective function. However, higher material savings and increased performance can be achieved if the structure and the cellular topologies are concurrently optimized.

Multi-scale design of structural and material has been considered with the use of porous materials in the seminal work by Bendsøe et al. [2] who recommend considering simple square voids at the micro-scale in the context of minimum compliance design. A similar approach was extended to compliant mechanism design by Nishiwaki et al. [3]. Rodrigues et al. [35] proposed a hierarchical topology optimization method in which the micro-structure was no longer limited to a specific type (e.g., rectangular or square hole or ranked laminates). The proposed method was based on Free Material Optimization (FMO) [36] and an iterative approach presented by Theo-

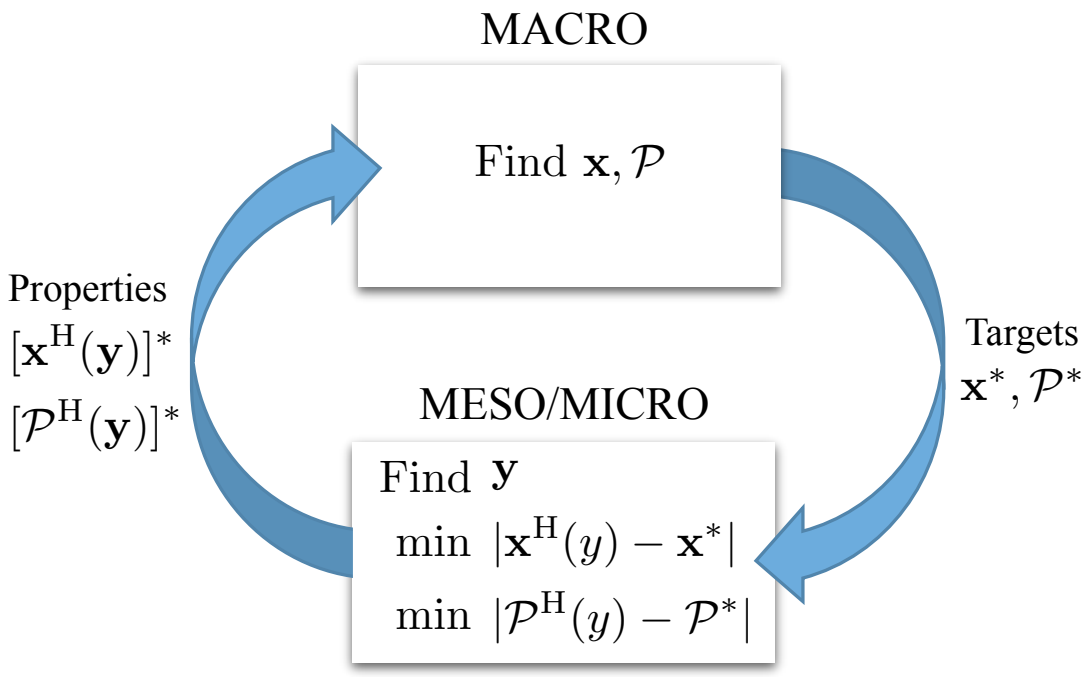

Figure 1.3. Concept of the multi-scale topology optimization.

caris et al. [37], it decoupled the topology optimization into two related sub problems. The drawback of this methodology is that it contains sub problems, which need to be solved that will lower efficiency of optimization procedure. Based on the works of Rodrigues et al. [35], hierarchical topology optimization with similar approach had been extended on many different areas including minimization a compliance problem for 3D [28] and bone remodeling [38] were proposed by Coelho. Design of material structure in micro-scale in energy wave management was suggested by Le et al. [39]. The hierarchical optimization that had also been adapted on static and dynamic design was discussed by Liu et al. [40]. More recent publications in multi-scale topology optimization address multi-scale topology optimization assuming a periodic cellular meso-structure, for which the periodic homogenization approaches were well established [41]. The optimum structures and material meso-structures for minimum compliance were achieved simultaneously. This method was further developed by

Niu et al. [42] working on the structure with optimum dynamic performance with maximum structural fundamental frequency and multi-objective concurrent topology optimization of thermoelastic structures by Deng et al. [43].

1.3 Motivation and Objectives

In this section we motivate and state the objectives of this study.

1.3.1 Preliminary Experimental Results

Traditionally, lightweight concept designs have been obtained using homogeneous materials. Figure 1.4(a) shows the design domain of a Messerschmitt-Bölkow-Blohm (MBB) beam problem as in [1], in which a concentrated vertical force is loaded at center of the top edge and the structure is supported horizontally in the lower right corner. A general topology optimization problem is stated in Eq. 1.1. Figure 1.4(b) is its topology optimized beam using the 99 line topology optimization code written in MATLAB® by Sigmund [44]. The mass fraction of this example is prescribed to be 0.50, which means only 50% of the design domain is filled with materials.

$$\begin{aligned} \text{minimize} &: \text{design objective} \\ \text{variables} &: \text{element densities} \\ \text{subject to} &: \text{equilibrium equations} \\ &\quad \text{constraints on mass fraction} \\ &\quad \text{bounds on design variables.} \end{aligned} \tag{1.1}$$

However, this approach is challenged by the use of low volume fraction/mass fraction. As can be seen in Fig. 1.5(a), when the mass fraction is low, e.g. 0.20, the final topology has lots of gray elements which is an undesirable result in topology optimization, because the ultimate goal of topology optimization is to achieve black-and-white solution. If the finite element mesh is made finer, we could see that, though

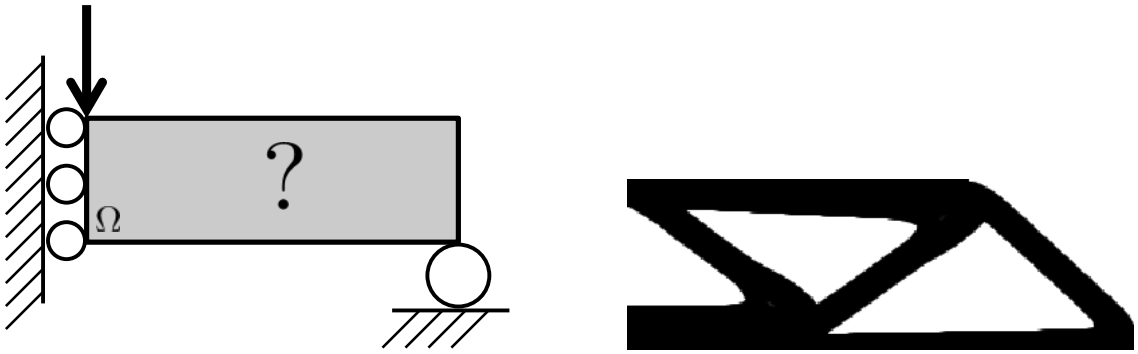

(a) Initial design domain for MBB-beam. (b) Resulting topology optimized beam.

Figure 1.4. Initial design domain for MBB-beam and its optimal solution.

the structure performance has little increase, some gray areas still show up in the final topology as shown in Fig. 1.5(b). When making the finite element mesh size even finer as in Fig. 1.5(c), the result from our cluster is out of memory. The traditional topology optimization method fails with only 270k (900x300) elements. There are many ways to overcome the out of memory issue in MATLAB®, for example: assigning more memory to MATLAB®, upgrading the hardware device, or using an iterative solver [45] instead of a direct solver to solve the equilibrium equation and so on. Even if this large-scale problem can be solved by MATLAB® successfully, the final topology will still be undesirable with tons of gray. The end of topology optimization is to derive a black-and-white structure. It is essential for us to find some other ways to fulfill the goal. Among those, we leverage cellular materials to achieve more reliable results. Cellular materials are commonly selected from a set of commercially available layouts, e.g., triangular, cubic, and honeycomb. However, the standard approach is challenged by the use of cellular materials. The use of cellular materials in topology optimization results in multi-scale arrangements are referred to as ultra-lightweight structures. Ultra-light structures are characterized by a high strength-to-weight ratio, and are desired in automobile, aerospace, and aircraft design due to their high performance and the reduced energy consumption involved.

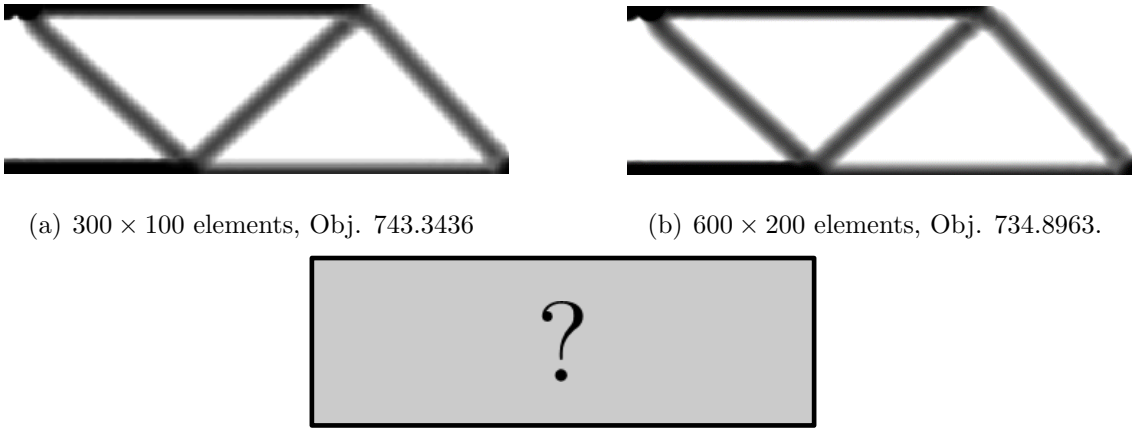

(a) 300 × 100 elements, Obj. 743.3436

(b) 600 × 200 elements, Obj. 734.8963.

(c) 900 × 300 elements, Out of Memory.

Figure 1.5. SIMP method applied on low mass fraction constraints.

1.3.2 Objectives

Although multi-scale topology optimization methods are well-studied by various authors as is the fact that cellular materials have high stiffness/strength-to-weight ratio, a systematic comparison between homogenous materials, periodic cellular materials and non-periodic materials barely exists. Clearly, there are several questions that need to be answered. For example, what exactly are the advantages of using cellular materials? Under what circumstances should we use cellular materials? Are cellular materials always be better than homogenous materials?

This investigation is devoted to providing systematic comparisons of structural performances with homogenous materials, periodic cellular materials and non-periodic materials. Errors involved in the multi-scale topology optimization procedure are also quantified in this investigation. We describe the results of our investigation as follows: in Chapter 2, periodic cellular materials are considered at meso-scale in light of current manufacturing practice, and numerical implementation issues (e.g. starting guess, penalization methods, homogenization, sensitivity analysis and regularization techniques) are discussed. Chapter 3 describes in the non-periodic meso-structures to pursue better structural performance on ultra-lightweight structure design. Error

quantifications of the multi-scale topology optimization processes are developed in Chapter 4. Final remarks and recommendations of this investigation are given in Chapter 5.

2. PERIODIC MESO-STRUCTURES

Multi-scale topology optimization methodology for structures with periodic cellular materials in continuum design domains is discussed in this chapter. The meso-structure is considered to be periodic on the macro-scale per current manufacturing experience and to reduce the cost of manufacturing structures with meso-structure.

In the spirit of the Rodrigues et al. [35], the multi-scale topology optimization problem for periodic meso-structure in the case of single loading can be stated as

$$\max_{\substack{0\leqslant\mathbf{x}\leqslant 1\\ \int_\Omega \mathbf{x}d\Omega\leqslant V_\Omega}} \min_{\mathbf{U}\in U}\left[\frac{1}{2}\times\int_\Omega \Phi(\rho,\mathbf{U})d\Omega-\left(\int_\Omega \mathbf{F}\cdot\mathbf{U}d\Omega+\int_{\Gamma_T}\mathbf{t}\cdot\mathbf{U}ds\right)\right], \tag{2.1}$$

$$\Phi(x,\mathbf{U})=\max_{\substack{\mathbf{y}\\ 0\leqslant\mathbf{y}\leqslant 1\\ \int_Y \mathbf{y}dY=V_Y}} C^{\mathrm{H}}_{ijpq}(\mathbf{y})\epsilon_{ij}(\mathbf{U})\epsilon_{pq}(\mathbf{U}). \tag{2.2}$$

Here $\mathbf{x}$ and $\mathbf{y}$ are the vectors of macro- and meso-scale design variables (i.e. the element densities). V_Ω is the total amount of composites in the macro-scale design domain Ω and V_Y is the total amount of base materials in the meso-scale design domain Y. The vector $\mathbf{F}$ represents the body forces, and $\mathbf{t}$ represents the boundary tractions. U is the space of kinematically admissible displacement fields $\mathbf{U}$, and $\epsilon(\mathbf{U})$ are the corresponding linearized strains. $C^{\mathrm{H}}_{ijpq}(\mathbf{y})$ is the effective stiffness tensor.

Equation 2.1 is the macro(outer) problem that distributes the composites on the macro-structure, and Eq. 2.2 is the meso (inner) problem that is involved in finding the optimal periodic meso-structure. However, this method needs to solve sub-problems, which will lower the efficiency of the optimization procedure. A novel method of solving this type of problem was proposed by Liu et al. [41]. In their method, the optimization problems were solved concurrently without solving the individual sub-problems; greatly reducing the computational cost is greatly reduced. Their method was originally developed to solve minimum compliance problems. In this chapter, we

will follow the method suggested in [41]; instead of only solving minimum compliance problems in [41], a more generalized form of optimization problem is given.

2.1 Problem Statement

This section discusses the individual parts of the optimization problem defined in Eq. 1.1.

2.1.1 Objective Function

The objective function expresses the structure property(-ies) $\mathcal{P}$. Those properties could include effective stiffness tensor, Strain Energy (SE), Mutual Potential Energy (MPE), fundamental frequency, etc. Specify expressions of objective functions will be given later.

2.1.2 Design Variables

The macro-scale design domain Ω was discretized into N elements and the meso-scale design domain Y was discretized into n elements. The design variables $\mathbf{x}$ on the macro-scale and $\mathbf{y}$ on the meso-scale refer to the element densities. Those design variables can be chosen from the lower boundary $\underline{x}$ to the upper boundary $\bar{x}$ and lower boundary $\underline{y}$ to 1, for reasons which will be discussed later.

2.1.3 Equilibrium Equations

When applying the principle of virtual work, i.e. that the stress, body force and traction are in equilibrium if and only if the internal virtual work equals the external virtual work for every virtual displacement field, on a general elasticity problem, as shown in Fig. 2.1, the virtual displacement equation can be constructed as

$$\int_{\Omega} C^{\mathrm{H}}_{ijkl}(\mathbf{x},\mathbf{y})\epsilon_{ij}(\mathbf{U})\epsilon_{kl}(\mathbf{v})d\Omega = \int_{\Omega} \mathbf{F}\cdot\mathbf{U}d\Omega + \int_{\Gamma_T} \mathbf{t}\cdot\mathbf{U}ds, \tag{2.3}$$

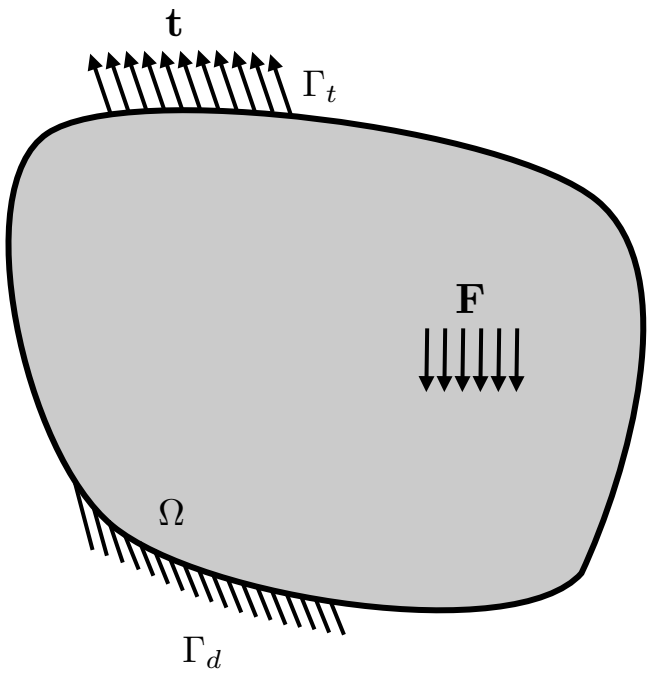

Figure 2.1. General elasticity problem.

with the linearized strains $\epsilon_{ij}(\mathbf{U}) = \frac{1}{2}(\frac{\partial u_i}{\partial x_j} + \frac{\partial u_j}{\partial x_i})$ and C^{H}_{ijkl} is the homogenized elastic tensor which will be discussed later.

The computational approach to solve problems in the form of Eq. 2.3 is to discretize the problem using Finite Elements (FE). We can write the discrete form of Eq. 2.3 as

$$\mathbf{K}^{\mathrm{H}}(\mathbf{x}, \mathbf{y})\mathbf{U} = \mathbf{F}, \tag{2.4}$$

where $\mathbf{K}^{\mathrm{H}}$ is the homogenized global stiffness matrix dependent on both macro- and meso-scale and can be assembled from the homogenized element stiffness matrices. This will be discussed later.

2.1.4 Constraints on Volume Fraction

The material volumes of macro-scale and meso-scale can be found as

$$\text{Macro} = \int_{\Omega} \mathbf{x} d\Omega, \tag{2.5}$$

$$\text{Meso} = \int_Y \mathbf{y} dY. \tag{2.6}$$

Having defined the design variables $\mathbf{x}$ and $\mathbf{y}$, and assuming that the design domain Ω and Y have been discretized by N and n equally sized FEs of volume[1] Ω_e and Y_e. The volume fractions of the two scales can be calculated as the sums

$$f_\Omega = \frac{1}{\Omega_0} \sum_{i=1}^{N} x_i v_i, \tag{2.7}$$

$$f_Y = \frac{1}{Y_0} \sum_{j=1}^{n} y_j v_j, \tag{2.8}$$

where Ω_0 and Y_0 are volume of design domains, and v_i and v_j are the volumes of each element. When the FEs are all equally sized, v_i and v_j are the same for each element and can therefore be moved in front of the summation symbol, and expressed as volume fractions

$$f_\Omega = \frac{\Omega_e}{\Omega_0} \sum_{i=1}^{N} x_i, \tag{2.9}$$

$$f_Y = \frac{Y_e}{Y_0} \sum_{j=1}^{n} y_j. \tag{2.10}$$

For a specific design problem, we might want to constrain the volume fractions of the design domains. This can be done by defining two volume fraction constraints as

$$g_1(\mathbf{x}) = \frac{\Omega_e}{\Omega_0} \sum_{i=1}^{N} x_i - \bar{\Omega} \leqslant 0, \tag{2.11}$$

$$g_2(\mathbf{y}) = \frac{Y_e}{Y_0} \sum_{j=1}^{n} y_j - \bar{Y} \leqslant 0, \tag{2.12}$$

where $\bar{\Omega}$ and $\bar{Y}$ are the upper boundaries on the volume fractions of the design domains Ω and Y.

[1]Note that volume is understood to refer to *area* $\times$ 1 in the 2D domain.

2.1.5 Boundary Constraints on Design Variables

Typically, the lower boundaries $\underline{x}$ and $\underline{y}$ on design variables x_i and y_j are set to a very small number (1×10^{-3}) instead of 0 to avoid the singularity of the stiffness matrix in the finite element formulation. However, with the implementation of the modified SIMP method in this investigation, the lower limits can be set to 0. The upper boundary of design variable x_i is no longer 1 since the composite materials are applied on the macro-structure. Then the bounds on the design variables can be given as $0 \leqslant x_i \leqslant \bar{Y}$, $(i = 1, \ldots, N)$ for macro-scale and $0 \leqslant y_j \leqslant 1$, $(j = 1, \ldots, n)$ for meso-scale.

2.1.6 The Final Optimization Problem

An optimization problem including all the features mentioned above can be written as

$$\begin{aligned} \text{find} \quad & \mathbf{X} = \{\mathbf{x}, \mathbf{y}\} \\ \min \quad & \mathcal{P}(\mathbf{x}, \mathbf{y}) \\ \text{subject to} \quad & \mathbf{K}^{\mathrm{H}}(\mathbf{x}, \mathbf{y})\ \mathbf{U} = \mathbf{F} \\ & g_1(\mathbf{x}) = \frac{\Omega_e}{\Omega_0} \sum_{i=1}^{N} x_i - \bar{\Omega} \leqslant 0 \\ & g_2(\mathbf{y}) = \frac{Y_e}{Y_0} \sum_{j=1}^{n} y_j - \bar{Y} \leqslant 0 \\ & 0 \leqslant x_i \leqslant \bar{Y}, \quad i = 1, \ldots, N \\ & 0 \leqslant y_j \leqslant 1, \quad j = 1, \ldots, n \end{aligned} \tag{2.13}$$

where $\mathbf{x}$ is the N-vector containing the design variables (element densities) of macro-scale, and $\mathbf{y}$ is the n-vector containing the design variables (element densities) of meso-scale.

2.2 Numerical Implementation Issues

In this section, the numerical implementation of the multi-scale topology optimization method for periodic cellular materials is discussed. A flow chart of the programming algorithm is shown in Fig. 2.2 and each individual step of the algorithm is described in the following subsections.

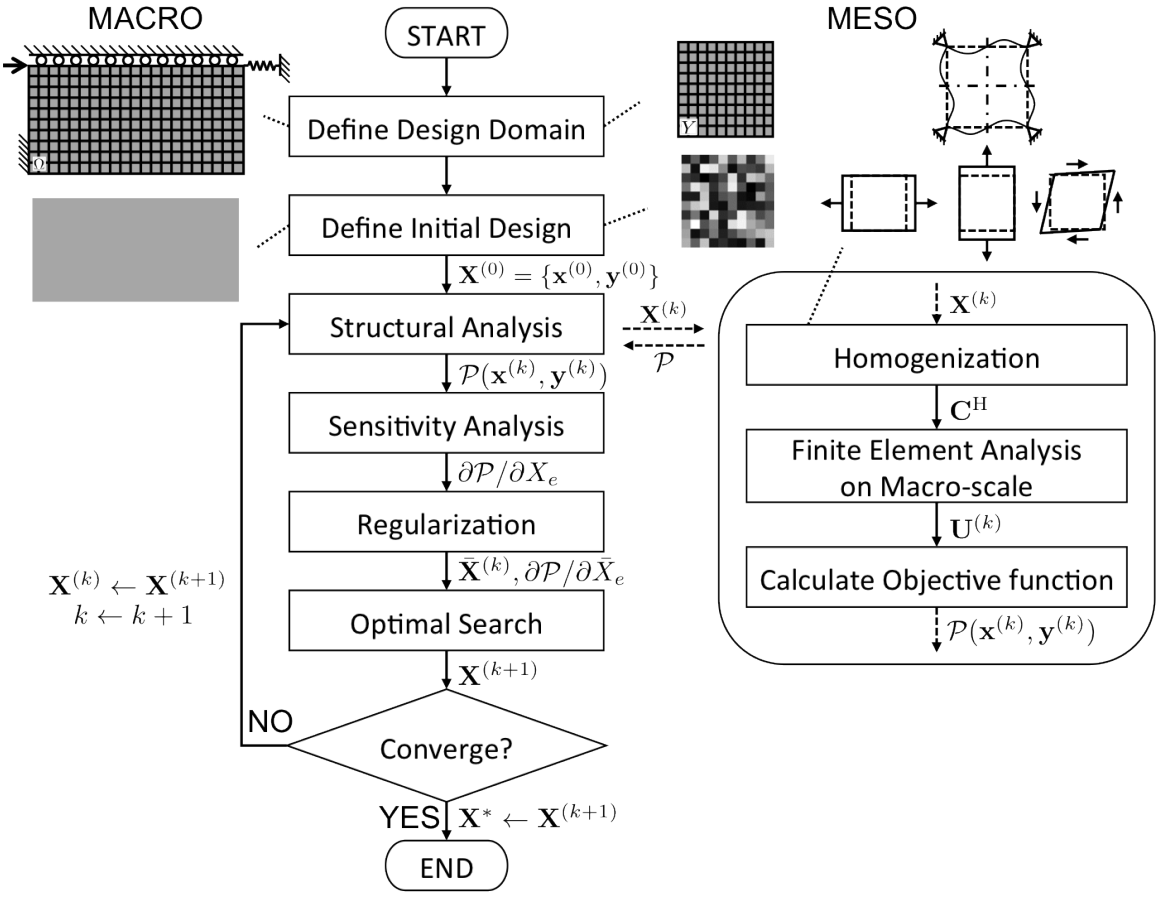

Figure 2.2. Programming flow chart.

2.2.1 Initialization

The macro-scale design domain Ω is discretized into N elements and the meso-scale design domain Y is discretized into n elements. Define the boundary conditions and the loading conditions of structure. Provide the base material properties: Elastic modulus E_0 and Poisson's ratio ν.

2.2.2 Starting Guess

The initial points of macro-scale design variables $\mathbf{x}^{(0)}$ can be set uniform with the value of macro-scale volume fraction $\bar{\Omega}$.

The initial points of meso-scale design variables $\mathbf{y}^{(0)}$ must be chosen from a random density distribution. First, one of the solutions (local minima) of this problem is homogeneous materials. In addition, the initial uniform design variables could cause the gradients corresponding to all design variables in meso-scale to have equal values, and thus, the optimization procedure would not have a good direction for starting the optimum search. One should note that the final meso-structures are highly dependent on the initial design due to the uncertainty of the starting guess [15].

2.2.3 Penalization Methods

This paper is based on the standard "density-based approach to topology optimization'' formalized by Bendsøe and Sigmund [13]. In this approach, the topology optimization problem is parameterized by the elastic modulus E_j of the discretized design domain. At the end of the optimization, designers are hoping to achieve black-and-white structures. Those regions with materials have elastic modulus $E_j = E_0$ and regions without materials (with soft materials) have elastic modulus $E_j = E_{\min} \approx 0$. The intermediate value for the elastic modulus is penalized to be close to either 0 or 1 using the modified SIMP [46].

We now consider the base material of an element j in meso-scale is linear isotropic so the constitutive matrix in Hooke's law is given as

$$\mathbf{C}(y) = \frac{E(y)}{1-\nu^2}\begin{bmatrix} 1 & \nu & 0 \\ \nu & 1 & 0 \\ 0 & 0 & \dfrac{1-\nu}{2} \end{bmatrix}. \tag{2.14}$$

Because the elastic modulus is a function of the design variables y_j, and is given by the modified SIMP interpolation scheme

$$E_j(y_j) = \mathrm{E}_{\min} + y_j^{\eta}(\mathrm{E}_0 - \mathrm{E}_{\min}), \quad y_j \in [0,1], \tag{2.15}$$

where η is the penalization power, $\mathrm{E}_{\min}$, which is set to 10^{-9}, is the stiffness of the soft (void) material. $\mathrm{E}_{\min}$ is set to a non-zero number in order to avoid singularity of the stiffness matrix. E_0 is the stiffness of base material.

The SIMP model can be used as a material model if the penalization power η satisfies (c.f. [47] for details)

$$\eta \geqslant \max\left\{\frac{2}{1-\nu}, \frac{4}{1+\nu}\right\}, \quad \text{(in 2D)}, \tag{2.16}$$

$$\eta \geqslant \max\left\{15\frac{1-\nu}{7-5\nu}, \frac{3(1-\nu)}{2(1-2\nu)}\right\}, \quad \text{(in 3D)}. \tag{2.17}$$

With a typical value of $\nu = 0.30$, Eqs. 2.16 and 2.17 yield $\eta \geqslant \max\{2.857, 3.077\}$ in 2D and $\eta \geqslant \max\{1.909, 2.625\}$ in 3D.

The working principle of the penalization power is best illustrated by means of Fig. 2.3: values of $y_j = 0.5$ and $\eta = 1.0$ result in a (linear) elastic modulus of $\mathrm{E}_0/2$, whereas $\eta = 3$ results in a contribution of less than 0.13. Penalization power therefore underestimates intermediate densities, driving them to values that represent void (soft) ≈ 0 densities.

The chance of achieving anisotropic material is very high when the meso-structure is obtained through topology optimization, especially if no isotropy or square symmetry constraints are applied. An equivalent version referred to as Porous Anisotropic

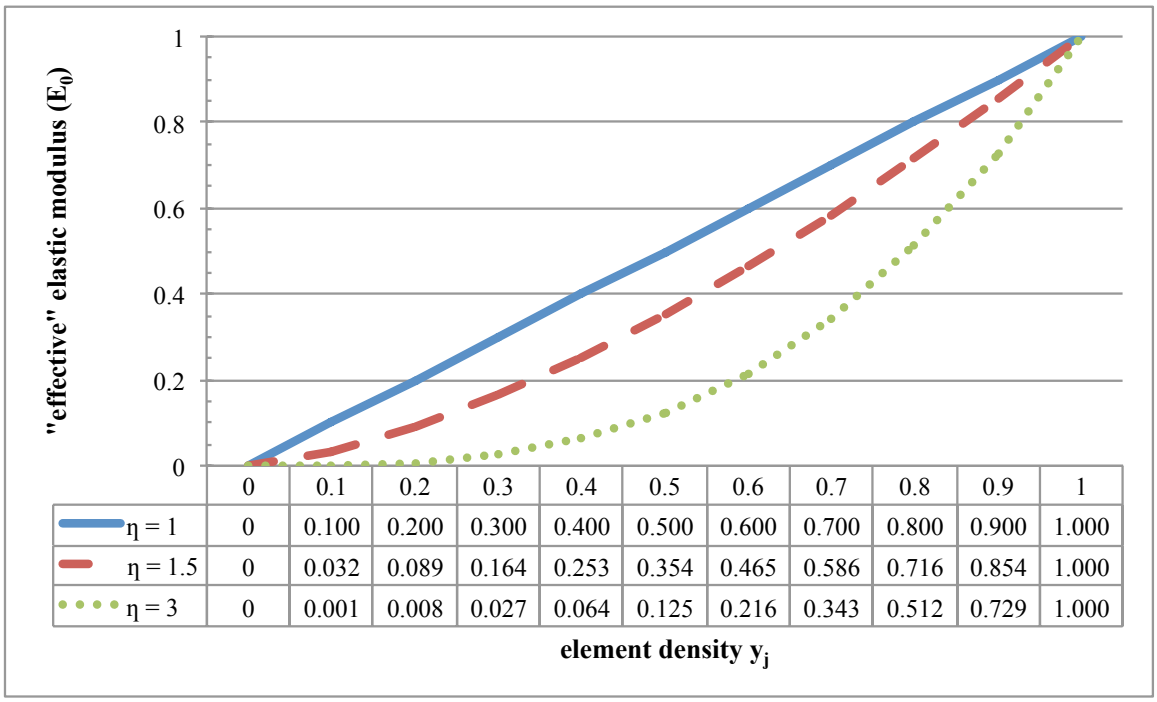

	0	0.1	0.2	0.3	0.4	0.5	0.6	0.7	0.8	0.9	1
η = 1	0	0.100	0.200	0.300	0.400	0.500	0.600	0.700	0.800	0.900	1.000
η = 1.5	0	0.032	0.089	0.164	0.253	0.354	0.465	0.586	0.716	0.854	1.000
η = 3	0	0.001	0.008	0.027	0.064	0.125	0.216	0.343	0.512	0.729	1.000

Figure 2.3. Illustration of penalization power.

Material with Penalization (PAMP) as suggested in [41] is incorporated in the macro-scale. Given any anisotropic material with base material elastic modulus E_0 and an element with density x_i at macro-scale, the modified PAMP interpolation scheme is given by

$$E_i(x_i) = E_{\min} + x_i^p(E_0 - E_{\min}), \quad x_i \in [0,1], \tag{2.18}$$

where p is the penalization power for the PAMP interpolation scheme.

By applying the penalization powers $\eta > 1$ and $p > 1$, the intermediate material densities are penalized to near to either 0 or 1 which lead to a clear black-and-white structure on both scales.

2.2.4 Homogenization Step

The effective material properties of meso-structures are represented by the effective stiffness tensor C^{H}_{ijkl}. The effective stiffness tensor is calculated following the standard homogenization theory [2, 14] by integrating over the base cell volume Y,

$$C^{\mathrm{H}}_{ijkl} = \frac{1}{Y_0}\int_Y \left[C_{ijkl} - C_{ijpq}\frac{\partial \chi^{kl}_p}{\partial y_q}\right] dY. \tag{2.19}$$

Here the characteristic displacement field is the Y-periodic solutions to the equilibrium equations in meso-scale

$$\int_Y C_{ijpq}\frac{\partial \chi^{kl}_p}{\partial y_q}\frac{\partial v_i(\mathbf{y})}{\partial y_j} dY = \int_Y C_{ijpq}\frac{\partial v_i(\mathbf{y})}{\partial y_j} dY, \text{ for all Y-periodic } v. \tag{2.20}$$

By solving the mesoscopic equilibrium equations Eq. 2.20, the characteristic displacement field χ^{kl} is used in Eq. 2.19 to find the effective stiffness tesnor. By assigning different values of k and l to Eqs. 2.19 and 2.20, the element homogenized stiffness matrix $\mathbf{c}^{\mathrm{H}}$ can be found. For 2-D problems (with $i, j, k, l, p, q = 1, 2$) it suffices to solve for three different cases (see Appendix A for details).

The mesoscopic equilibrium equations are solved by FE methods with three load cases[2]

$$\mathbf{k}\boldsymbol{\chi}^{kl} = \mathbf{f}^{kl}, \tag{2.21}$$

where the characteristic displacements field $\boldsymbol{\chi}^{kl}$ are constrained to be Y-periodic, as shown in Fig. 2.4. This is accomplished either by applying a penalty approach, Lagrange multipliers[3], or simply assigning equal node numbers to opposing boundary nodes [48]. The global stiffness matrix $\mathbf{k}$ in the meso-scale is assembled by the element stiffness matrices as usual $\mathbf{k}(\mathbf{y}) = \mathcal{A}_{j=1}^{n}\mathbf{k}_j(\mathbf{y})$ with corrections for periodicity.

The force vector is found from

$$\mathbf{f}^{kl} = \sum_{j=1}^{n}\int_{Y_j} \mathbf{b}^{\mathrm{T}}\mathbf{C}(\mathbf{y})\boldsymbol{\epsilon}^{0(kl)}\, dY, \tag{2.22}$$

[2] six in 3-D problems with $k, l = 1, 2, 3$.

[3] Lagrange multipliers are implemented in this investigation, see Appendix B for details

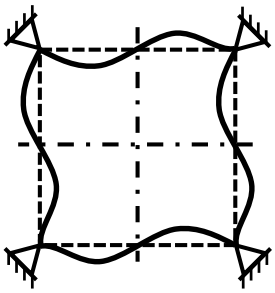

Figure 2.4. Unit cell periodic boundary condition.

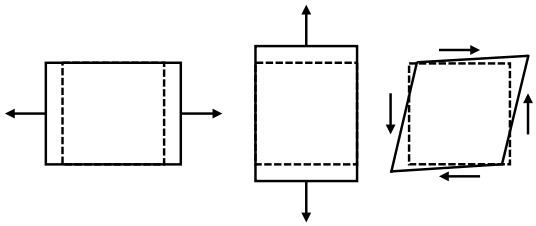

Figure 2.5. Unit test prestrains.

where $\mathbf{b}$ is the FE strain-displacement matrix in the meso-scale. $\mathbf{C}(\mathbf{y})$ is the constitutive matrix in Hook's law with penalization applied as shown in Eq. 2.14, $\boldsymbol{\epsilon}^{0(kl)}$ are the three cases of unit prestrain, as shown in Fig. 2.5

$$\boldsymbol{\epsilon}^{0(11)} = \begin{Bmatrix} 1 \\ 0 \\ 0 \end{Bmatrix}, \qquad \boldsymbol{\epsilon}^{0(22)} = \begin{Bmatrix} 0 \\ 1 \\ 0 \end{Bmatrix}, \qquad \boldsymbol{\epsilon}^{0(12)} = \begin{Bmatrix} 0 \\ 0 \\ 1 \end{Bmatrix}, \tag{2.23}$$

and the FE strain-displacement matrix $\mathbf{b}$ for the quad-4 node element can be found as

$$\mathbf{b} = \begin{bmatrix} \frac{\partial \mathcal{S}_1}{\partial \xi} & 0 & \frac{\partial \mathcal{S}_2}{\partial \xi} & 0 & \frac{\partial \mathcal{S}_3}{\partial \xi} & 0 & \frac{\partial \mathcal{S}_4}{\partial \xi} & 0 \\ 0 & \frac{\partial \mathcal{S}_1}{\partial \eta} & 0 & \frac{\partial \mathcal{S}_2}{\partial \eta} & 0 & \frac{\partial \mathcal{S}_3}{\partial \eta} & 0 & \frac{\partial \mathcal{S}_4}{\partial \eta} \\ \frac{\partial \mathcal{S}_1}{\partial \eta} & \frac{\partial \mathcal{S}_1}{\partial \xi} & \frac{\partial \mathcal{S}_2}{\partial \eta} & \frac{\partial \mathcal{S}_2}{\partial \xi} & \frac{\partial \mathcal{S}_3}{\partial \eta} & \frac{\partial \mathcal{S}_3}{\partial \xi} & \frac{\partial \mathcal{S}_4}{\partial \eta} & \frac{\partial \mathcal{S}_4}{\partial \xi} \end{bmatrix}, \tag{2.24}$$

where $\mathcal{S}$ is the shape function. In terms of the natural coordinates ξ_1 and ξ_2, the shape functions $\mathcal{S}$ are

$$\begin{aligned} \mathcal{S}_1 &= \frac{1}{4}(1-\xi_1)(1-\xi_2), \\ \mathcal{S}_2 &= \frac{1}{4}(1+\xi_1)(1-\xi_2), \\ \mathcal{S}_3 &= \frac{1}{4}(1+\xi_1)(1+\xi_2), \\ \mathcal{S}_4 &= \frac{1}{4}(1-\xi_1)(1+\xi_2). \end{aligned} \tag{2.25}$$

Then, the effective stiffness tensor in FE notation is computed via

$$C^{\mathrm{H}}_{ijkl}(\mathbf{y}) = \frac{1}{Y_0}\sum_{j=1}^{n}(\boldsymbol{\chi}^{0(ij)} - \boldsymbol{\chi}^{ij})^{\mathrm{T}} \int_{Y_j} \mathbf{b}^{\mathrm{T}}\mathbf{C}(\mathbf{y})\mathbf{b}\; dY\; (\boldsymbol{\chi}^{0(kl)} - \boldsymbol{\chi}^{kl}), \tag{2.26}$$

where, Y_0 is the volume of a unit base cell, and $\boldsymbol{\chi}^{0(kl)}$ are the displacements corresponding to the test strains.

Note that for brevity of notation, we omitted the dependence of $C^{\mathrm{H}}_{ijkl}(\mathbf{y})$ on $\boldsymbol{\chi}$.

2.2.5 Sensitivities

The sensitivity of the objective function $\mathcal{P}$ will be given after the $\mathcal{P}$ is defined.

The sensitivity of a component of the effective stiffness tensor Eq. 2.26 with respect to the density of the meso-scale design variable y_j can be found by the adjoint method [1],

$$\frac{\partial C^{\mathrm{H}}_{ijkl}}{\partial y_j} = \frac{1}{Y_0}(\boldsymbol{\chi}^{0(ij)} - \boldsymbol{\chi}^{ij})^{\mathrm{T}} \int_{Y_j} \mathbf{b}^{\mathrm{T}}\frac{\partial \mathbf{C}(\mathbf{y})}{\partial y_j}\mathbf{b}\; dY(\boldsymbol{\chi}^{0(kl)} - \boldsymbol{\chi}^{kl}). \tag{2.27}$$

2.2.6 Optimization Method

As the optimizer, we use the MATLAB implementation of the Method of Moving Asymptotes (MMA) [4] made freely available for research purposes by Krister Svanberg. The iterative design approach is repeated until the change in each design variable in two successive iterations $[(k+1) - k]$ is less than 0.01.

2.2.7 Regularization Techniques

The standard "density approach to topology optimization'' [13] is likely to encounter numerical instabilities if no regularization techniques are applied [49]. If one increases the FE mesh and resolves the problem, the new results will generally not be an improvement of the same design. Rather, each new mesh size will produce a different design. This is called mesh-dependency. Another numerical instability is a so-called checkerboard pattern as shown in Fig. 2.6. For an optimization problem

without an optimal solution, a checkerboard pattern will arise. Another difficulty is the existence of local minima. The SIMP method is applied to achieve black-and-white topology. Convexity is a good property since every local minimum is also global minimum, and the global minimum is what we want. Unfortunately, with penalization power $\eta > 1$ and/or $p > 1$, the optimization problem becomes non-convex. In this case for different starting points, the program may converge to totally different local minima.

The density filter, first introduced by Bruns et al. [50] and further proved mathematically by Bourdin et al. [51] is a commonly used regularization scheme in the SIMP based topology optimization procedure. The standard density filter is given as

$$\tilde{X}_e = \frac{\sum_{e=1}^{N+n} \omega \; v_e \; X_e}{\sum_{e=1}^{N+n} \omega \; v_e}, \tag{2.28}$$

where v_e and X_e denote the volume and density of the design variable e. For example, on the macro-scale, $v_e = v_i$ and $X_e = x_i$, and on the meso-scale, $v_e = v_j$ and $X_e = y_j$. The weight factor ω is given by a linear function as suggested in [50], by

$$\begin{aligned} \omega = \max\{0, \; r_{\min} - \mathrm{dist}(e,h)\}, \\ \{h \in N(\text{or } n) \mid \mathrm{dist}(e,h) \leqslant r_{\min}\}, \quad e = 1, \ldots, N(\text{or } n), \end{aligned} \tag{2.29}$$

where the operator $\mathrm{dist}(e,h)$ is defined as the distance between the center of element e and the center of element h. $r_{\min}$ is the radius or filter size.

An important improvement of the density filter Eq. 2.28 is the Heaviside filter [46, 52, 53]. The original filter is modified with a Heaviside function in order to get approximate black-and-white solutions. The physical density $\bar{X}_e$ is equal to 1 if $\tilde{X}_e > 0$, and is set to its lower bound (void/soft) if $\tilde{X}_e = 0$. The Heaviside function is changed to a smooth function

$$\bar{X}_e = 1 - \mathrm{e}^{-\beta \tilde{X}_e} + \tilde{X}_e \mathrm{e}^{-\beta}. \tag{2.30}$$

The smoothing parameter β governs the smoothness of the approximation function: for β equals zero, the Heaviside filter is exactly same as the original density filter Eq. 2.28; as β goes to infinity, Eq. 2.30 is a true Heaviside step function.

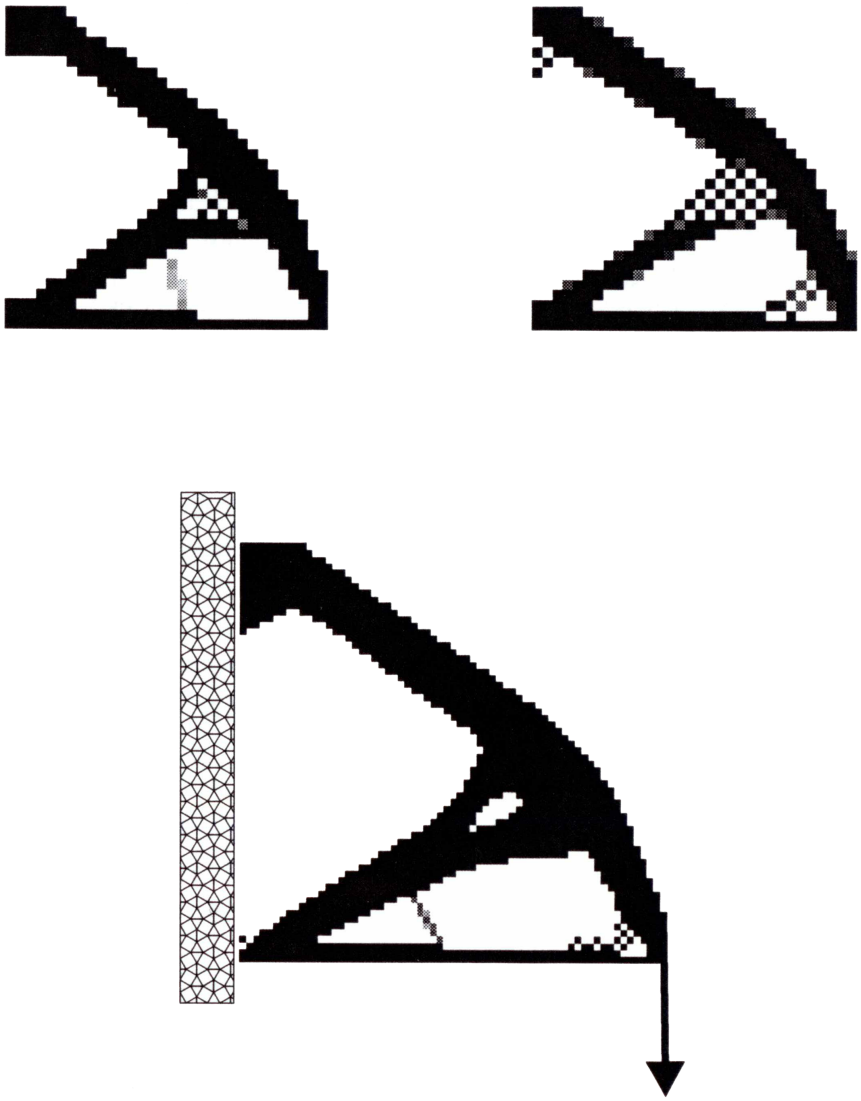

Figure 2.6. Three pictures produced by use of the SIMP method for an ill-posed problem. The *upper two pictures* are produced using the same FE mesh, where a continuation strategy with the penalty exponent p applied in the *left-hand case* but not in the *right-hand case*. The *lower picture* is produced using 4 times the number of elements of the *upper two pictures*. These solutions show mesh-dependency and checkerboards. Figure from [49].

When solving optimization problems like Eq. 2.13, a continuation strategy is used to increase the smoothing parameter β gradually so that it does not approach the

step function too quickly. The continuation scheme suggested in [46] is used: the parameter β starts from 1 and doubles every 50 iterations or when the change of the design variables in two successive designs is less than 1%, until the maximum value of $\beta_{\max} = 500$ has been reached.

However, a disadvantage of the Heaviside filter is that the continuation scheme discussed above must be applied to the continuous approximation. Changing the smoothing parameter β will change the approximation function and the resulting element density X_e. This can lead to non-preservation of volume which is clearly undesirable in the optimization procedure. Combining the Heaviside and Modified Heaviside functions can achieve volume preservation [54]. A more efficient method of eliminating the continuation of smoothing parameter β [53] can be achieved by: (1) using a large constant value of β; and/or (2) relaxing the upper bound on the independent design variable X and slightly modifying the Heaviside approximation function Eq. 2.30 to maintain the densities in the range [0,1]. These algorithms are simpler and more efficient than the original Heaviside filter since β is held constant.

In our implementation, we made use of the first approach using a constant β of large magnitude. One should note that it is recommended that different smoothing parameters are chosen for macro and meso-scale design variables.

The main idea of eliminating beta-continuation [53] is presented below: using a sharp approximation ($\beta \geqslant 20$) to te Heaviside step function Eq. 2.30 leads to great oscillations when applying the default configuration of MMA parameters. To prevent such oscillations, the initial asymptotes of the MMA are tightened as follows:

During the first two iterations ($k < 2.5$), the lower asymptotes (L_e) and upper asymptotes (U_e) for each design variable e are set using the following equations

$$\begin{aligned} L_e^{(k)} &= X_e^{(k)} - s_0(X_e^{\max} - X_e^{\min}), \\ U_e^{(k)} &= X_e^{(k)} + s_0(X_e^{\max} - X_e^{\min}), \end{aligned} \tag{2.31}$$

where k refers to the iteration number. $X_e^{\min}$ and $X_e^{\max}$ are given lower and upper bounds. s_0 denotes the distance of the asymptote from the current point and is usually set $s_0 = 0.6$. To restrain oscillatory behavior,

$$s_0 = \frac{0.5}{\beta + 1}, \tag{2.32}$$

is suggested in [53].

In order to penalize intermediate densities and mitigate the premature convergence to one of the multiple local minima when solving the non-convex problem, a continuation step can be performed on the SIMP-based design. The continuation strategy is previously of [55]

$$p^k = \begin{cases} 1 & k \leqslant 40, \\ \min\{p^{\max}, 1.02p^{k-1}\} & k > 40, \end{cases} \tag{2.33}$$

is used, where $p^{\max}$ is the maximum penalization power.

This methodology is not proven to converge to the global optimum, but it regularizes the algorithm and allows the comparison of different optimization strategies.

2.3 Topology Optimization for Stiff Structures

A structure described as stiff if it has the least possible displacement for a given certain set of boundary conditions. A global measure of the displacement is the Strain Energy (SE) of the structure under the prescribed boundary conditions. The lower SE, the higher the stiffness of the structure. Therefore, the problem statement involves the objective functional of the strain energy which has to be minimized.

2.3.1 Optimization Problem Statement

The Strain Energy (SE) is defined as

$$\text{SE} = \int_\Omega \frac{1}{2}\sigma : \epsilon \; d\Omega, \tag{2.34}$$

where σ and ϵ are fields generated by the input loading. Eq. 2.34 can be discretized as

$$\mathrm{SE} = \frac{1}{2}\mathbf{U}^{\mathrm{T}}\mathbf{K}^{\mathrm{H}}(\mathbf{x},\mathbf{y})\mathbf{U}, \tag{2.35}$$

where $\mathbf{K}^{\mathrm{H}}$ is the homogenized global stiffness matrix dependent on both scales and can be assembled from the homogenized element stiffness matrices

$$\mathbf{K}^{\mathrm{H}}(\mathbf{x},\mathbf{y}) = \mathcal{A}_{i=1}^{N}.\mathbf{K}_i^{\mathrm{H}}(x_i,\mathbf{y}). \tag{2.36}$$

From the knowledge of the FE method, the homogenized element stiffness matrix can be calculated through

$$\mathbf{K}_i^{\mathrm{H}}(x_i,\mathbf{y}) = \int_{\Omega_i} \mathbf{B}^{\mathrm{T}}\mathbf{C}^{\mathrm{H}}(x_i,\mathbf{y})\mathbf{B}\ d\Omega. \tag{2.37}$$

Here $\mathbf{C}^{\mathrm{H}}(x_i,\mathbf{y})$ is the effective stiffness tensor. If we combining Eq. 2.14 and Eq. 2.18, we have

$$\mathbf{C}^{\mathrm{H}}(x_i,\mathbf{y}) = \mathrm{E}_i(x_i)[\mathbf{C}^{\mathrm{H}}(\mathbf{y})]^0. \tag{2.38}$$

where $[\mathbf{C}^{\mathrm{H}}(\mathbf{y})]^0$ is the homogenized effective tensor with unit elastic modulus.

Substituting Eq. 2.38 into Eq. 2.37 yields

$$\begin{aligned}\mathbf{K}_i^{\mathrm{H}}(x_i,\mathbf{y}) &= \mathrm{E}_i(x_i)\int_{\Omega_i}\mathbf{B}^{\mathrm{T}}[\mathbf{C}^{\mathrm{H}}(\mathbf{y})]^0\mathbf{B}\ d\Omega,\\ &= \mathrm{E}_i(x_i)[\mathbf{K}_i^{\mathrm{H}}(\mathbf{y})]^0,\\ &= [\mathrm{E}_{\min} + x_i^p(\mathrm{E}_0 - \mathrm{E}_{\min})][\mathbf{K}_i^{\mathrm{H}}(\mathbf{y})]^0.\end{aligned} \tag{2.39}$$

Therefore, the optimization problem for stiff structures is

$$\begin{aligned} \text{find} \quad & \mathbf{X} = \{\mathbf{x}, \mathbf{y}\} \\ \min \quad & \text{SE} = \sum_{i=1}^{N} (\text{SE})_i = \sum_{i=1}^{N} \mathbf{U}_i^{\text{T}} \mathbf{K}_i^{\text{H}}(x_i, \mathbf{y}) \mathbf{U}_i \\ \text{subject to} \quad & \mathbf{K}^{\text{H}}(\mathbf{x}, \mathbf{y})\ \mathbf{U} = \mathbf{F} \\ & g_1(\mathbf{x}) = \frac{\Omega_e}{\Omega_0} \sum_{i=1}^{N} x_i - \bar{\Omega} \leqslant 0 \\ & g_2(\mathbf{y}) = \frac{Y_e}{Y_0} \sum_{j=1}^{n} y_j - \bar{Y} \leqslant 0 \\ & 0 \leqslant x_i \leqslant \bar{Y}, \quad i = 1, \ldots, N \\ & 0 \leqslant y_j \leqslant 1, \quad j = 1, \ldots, n \end{aligned} \tag{2.40}$$

where $\mathbf{U}_i$ and $\mathbf{K}_i^{\text{H}}$ denote displacement vector and homogenized stiffness matrix of the i^{th} element in macro-scale.

2.3.2 Sensitivity Analysis of Objective Function

The details of sensitivity analysis of the objective function in Eq. 2.40 are given in this subsection.

As stated before, the structural SE is a summation of elemental SE

$$\text{SE} = \sum_{i=1}^{N} (\text{SE})_i = \sum_{i=1}^{N} \mathbf{U}_i^{\text{T}} \mathbf{K}_i^{\text{H}}(x_i, \mathbf{y}) \mathbf{U}_i. \tag{2.41}$$

The product of $\mathbf{U}_i$ and $\mathbf{K}_i^{\text{H}}$ equals to the nodal force vector

$$\mathbf{K}_i^{\text{H}}(x_i, \mathbf{y}) \mathbf{U}_i = \mathbf{F}_i. \tag{2.42}$$

Note that the force vector $\mathbf{F}$ is independent of the design variables $\mathbf{X} = \{\mathbf{x}, \mathbf{y}\}$, i.e. $\mathbf{F} \neq f(\mathbf{X})$. Hence, the derivation of Eq. 2.42 on both side will lead to

$$\frac{\partial \mathbf{K}_i^{\text{H}}}{\partial X} \mathbf{U}_i + \mathbf{K}_i^{\text{H}} \frac{\partial \mathbf{U}_i}{\partial X} = 0. \tag{2.43}$$

Then the derivative of SE with respect to X can be expressed as

$$\frac{\partial \mathrm{SE}}{\partial X} = \frac{\partial \sum_{i=1}^{N} \mathbf{U}_i^{\mathrm{T}} \mathbf{K}_i^{\mathrm{H}}(x_i, \mathbf{y}) \mathbf{U}_i}{\partial X} = \sum_{i=1}^{N} \frac{\partial \mathbf{U}_i^{\mathrm{T}} \mathbf{K}_i^{\mathrm{H}}(x_i, \mathbf{y}) \mathbf{U}_i}{\partial X}. \tag{2.44}$$

The right hand side of Eq. 2.44 can be expand as

$$\frac{\partial \mathbf{U}_i^{\mathrm{T}} \mathbf{K}_i^{\mathrm{H}} \mathbf{U}_i}{\partial X} = \frac{\partial \mathbf{U}_i^{\mathrm{T}}}{\partial X} \mathbf{K}_i^{\mathrm{H}} \mathbf{U}_i + \mathbf{U}_i^{\mathrm{T}} \frac{\partial \mathbf{K}_i^{\mathrm{H}}}{\partial X} \mathbf{U}_i + \mathbf{U}_i^{\mathrm{T}} \mathbf{K}_i^{\mathrm{H}} \frac{\partial \mathbf{U}_i}{\partial X}. \tag{2.45}$$

Utilizing Eq. 2.43, we have

$$\frac{\partial \mathbf{U}_i^{\mathrm{T}} \mathbf{K}_i^{\mathrm{H}} \mathbf{U}_i}{\partial X} = -\mathbf{U}_i^{\mathrm{T}} \frac{\partial \mathbf{K}_i^{\mathrm{H}}}{\partial X} \mathbf{U}_i. \tag{2.46}$$

The combination of Eq. 2.44 and Eq. 2.46 will lead to

$$\frac{\partial \mathrm{SE}}{\partial X} = -\sum_{i=1}^{N} \mathbf{U}_i^{\mathrm{T}} \frac{\partial \mathbf{K}_i^{\mathrm{H}}}{\partial X} \mathbf{U}_i. \tag{2.47}$$

Now, let us consider the derivative of objective function with respect to the macro-scale design variables $\mathbf{x}$. Note that $\mathbf{K}_i^{\mathrm{H}}$ can be expressed in the form of Eq. 2.39.

$$\begin{aligned} \frac{\partial \mathrm{SE}}{\partial x_i} &= -\sum_{i=1}^{N} \mathbf{U}_i^{\mathrm{T}} \frac{\partial \mathbf{K}_i^{\mathrm{H}}(x_i, \mathbf{y})}{\partial x_i} \mathbf{U}_i, \\ &= -\sum_{i=1}^{N} \mathbf{U}_i^{\mathrm{T}} \frac{\partial E_i(x_i)}{\partial x_i} [\mathbf{K}_i^{\mathrm{H}}(\mathbf{y})]^0 \mathbf{U}_i. \end{aligned} \tag{2.48}$$

Since each design variable x_i is independent of each others and the derivatives of Eq. 2.18 is quite straight forward, then the equation above can be simplified as

$$\frac{\partial \mathrm{SE}}{\partial x_i} = -[p x_i^{p-1}(E_0 - E_{\min})] \mathbf{U}_i^{\mathrm{T}} [\mathbf{K}_i^{\mathrm{H}}(\mathbf{y})]^0 \mathbf{U}_i. \tag{2.49}$$

For the same problem, the derivative of objective function with respect to the meso-scale is expressed as

$$\begin{aligned} \frac{\partial \mathrm{SE}}{\partial y_j} &= -\sum_{i=1}^{N} \mathbf{U}_i^{\mathrm{T}} \frac{\partial \mathbf{K}_i^{\mathrm{H}}(x_i, \mathbf{y})}{\partial y_j} \mathbf{U}_i, \\ &= -\sum_{i=1}^{N} \mathbf{U}_i^{\mathrm{T}} E_i(x_i) \frac{\partial [\mathbf{K}_i^{\mathrm{H}}(\mathbf{y})]^0}{\partial y_j} \mathbf{U}_i, \\ &= -\sum_{i=1}^{N} E_i(x_i) \ \mathbf{U}_i^{\mathrm{T}} \left[\int_{\Omega_i} \mathbf{B}^{\mathrm{T}} \frac{\partial [\mathbf{C}^{\mathrm{H}}(\mathbf{y})]^0}{\partial y_j} \mathbf{B} \ d\Omega \right] \mathbf{U}_i. \end{aligned} \tag{2.50}$$

The sensitivity of a component of the effective elastic matrix (Eq. 2.26) with respect to the density design variable y_j can be found by the adjoint method. The resulting sensitivity expression is given by Eq. 2.27.

2.3.3 Measure of Discreteness

In order to tell whether an optimized design has converged to a discrete solution, we introduced a "measure of discreteness" [46]

$$M_{nd} = \frac{\sum_{i=1}^{N} 4\bar{x}_i(1-\bar{x}_i)}{N} \times 100\%, \tag{2.51}$$

where $\bar{x}_i$ is the physical density correspond to macro-scale element i.

The desired value of M_{nd} might differences for each problems. Consider a macro-structure with uniform element density distribution value of 0.50. This will lead to $M_{nd} = 100\%$, as shown in Fig. 2.7. Therefore, the lower M_{nd}, the higher discreteness of final solution.

(a) $M_{nd} = 100\%$. (b) $M_{nd} = 21\%$. (c) $M_{nd} = 0\%$.

Figure 2.7. Illustration of measure of discreteness.

2.3.4 Numerical Example

A classic MBB-beam problem [1] with a concentrated vertical force of $F = 1$ is loaded at center of the top edge and the structure is supported horizontally in the lower right corner. Only half of the MBB-beam is considered due to the axial symmetry, and the macro-scale design domain is sketched as shown in Fig. 2.8. The design domains are discretized into 60×20 elements in the macro-scale and 40×40

elements in the meso-scale. The macro-scale design domain mesh for the structure with homogeneous materials is 300×100. The base material has elastic modulus $E_0 = 1$ and Poisson's ratio $\nu = 0.30$. The filter size of macro-scale is 0.03 times the width of the design domain, and 0.04 times the width of meso-scale design domain for meso-scale. The initial designs already discussed in the previous section.

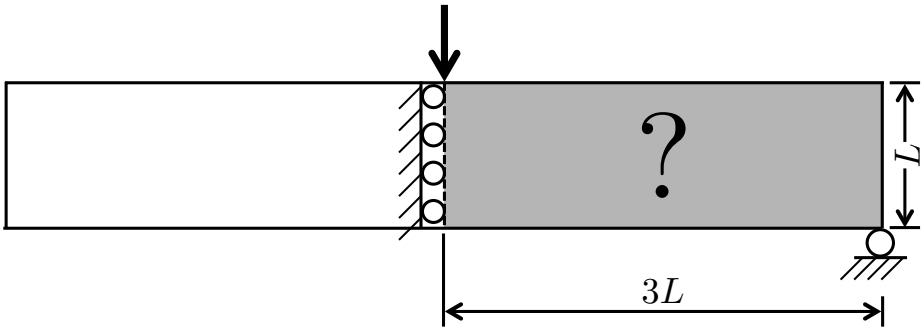

Figure 2.8. Initial design domain for MBB-beam.

Fixed Macro-scale Volume Fraction $\bar{\Omega}$

When we set the macro-scale volume fraction $\bar{\Omega}$ to 0.50, the topologies of structure with homogeneous materials gives us a most black-and-white structure (c.f.Fig. 2.9). Therefore, the macro-scale volume fraction of structure with periodic cellular materials $\bar{\Omega}$ is fixed to be 0.50. The meso-scale volume fraction $\bar{Y}$ changes from 0.075 to 1.000 with step size 0.025. The meso-scale structures range from very thin truss-like structures to completely solid.

Figure 2.9 shows the measure of discreteness for both materials in this example. We notice that when $M_{nd} \geqslant 20\%$, the optimized designs are gray structures, those artificial results are undesirable. When $16\% \leqslant M_{nd} < 20\%$, the results are acceptable. When $M_{nd} < 16\%$, the topologies are clear black-and-white with few gray elements in the structure.

From Fig. 2.9, the structures with homogeneous materials can not get acceptable results until the structure mass is greater than 0.25 (at Mass = 0.25, $M_{nd} = 19.29\%$).

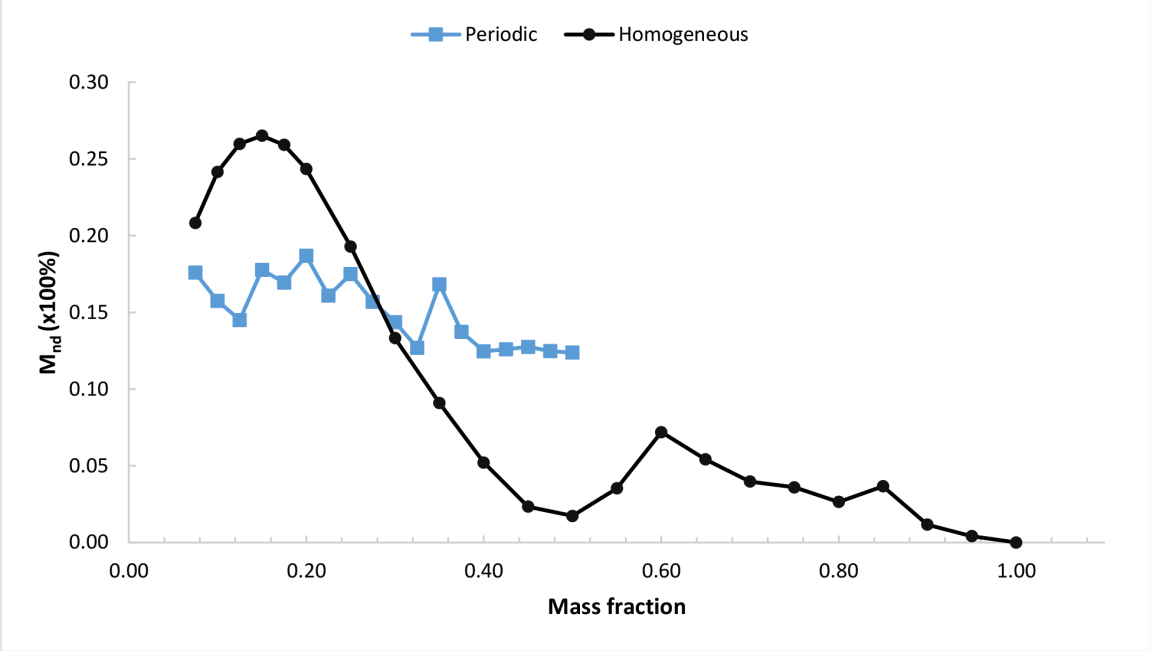

Figure 2.9. Measure of discreteness for stiff structure.

Figure 2.10 shows the Pareto fronts of structure with periodic cellular materials and homogeneous materials. The Pareto fronts of both periodic cellular materials and homogeneous materials are derived based on the experiment data. As from the experiment results(see Fig. 2.9), when mass fraction of macro-scale with homogeneous material goes to a small number (i.e., 0.25 or less), M_{nd} is grater than 20%, the result topologies are undesirable (marked as '$\times$' in Fig. 2.10. Additionally, there are some areas on the plot, referred to as ultra-light structure areas, traditional topology optimization with homogeneous materials can not achieve. Structures with periodic cellular materials are superior to the homogeneous materials on these zones with less structural mass and black-and-white topologies, although the structural performance have not improved comparing to the homogeneous materials. The structure SE for both homogeneous materials and periodic cellular materials at point Mass = 0.50 overlap to became one point which is as predicted. Figure 2.11 gives some selective topologies with periodic cellular materials.

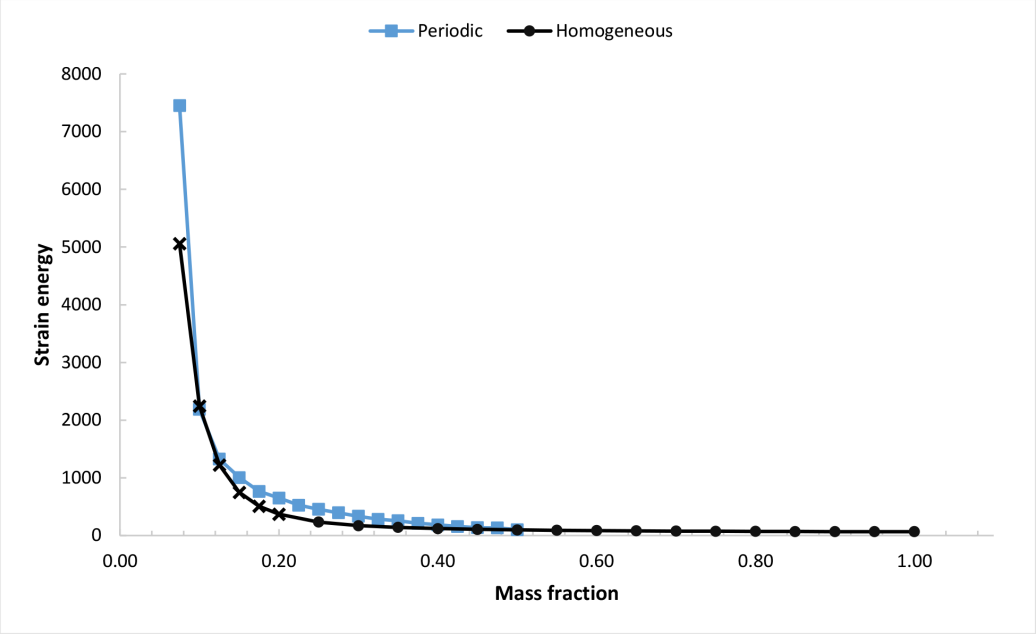

Figure 2.10. Pareto fronts for fixed macro-scale mass fraction.

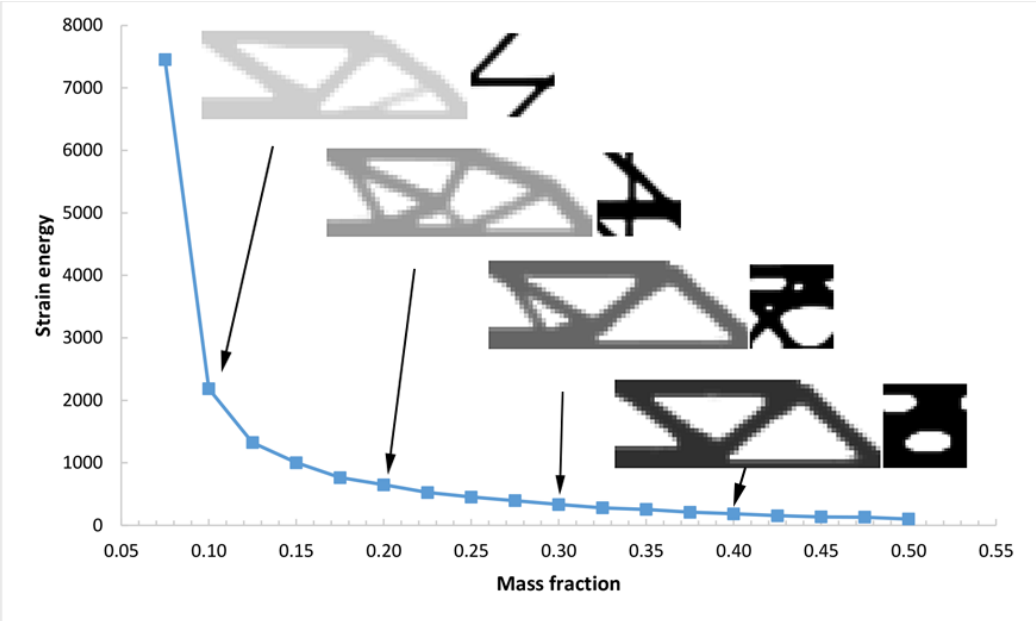

Figure 2.11. Selective topologies for structures using periodic cellular materials with fixed macro-scale mass fraction.

Fixed Meso-scale Volume Fraction $\bar{Y}$

In this example, the meso-scale volume fraction $\bar{Y}$ is prescribed to be 0.40 and we change the macro-scale volume fraction from 0.20 to 1.00 with step size 0.05. The Mass-M_{nd} plot are shown in Fig. 2.12, some test points are abandoned based on M_{nd}. The Pareto fronts for two different material types are shown in Fig. 2.13. As we can see from the figure, the periodic cellular materials are superior to homogeneous materials in the ultra-lightweight structure areas. The results for homogeneous materials in these areas are artificial results. Some selective topologies of the fixed meso-scale volume fraction are shown in Fig. 2.14.

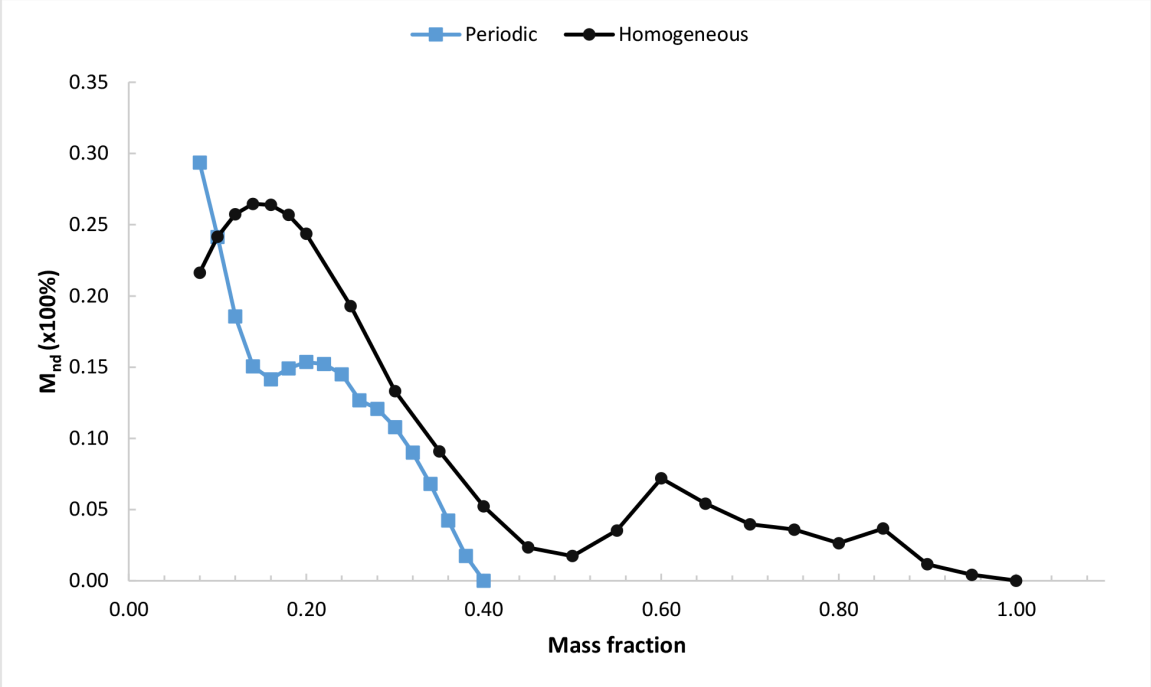

Figure 2.12. Measure of discreteness for stiff structure.

In the most extreme case , the prescribed macro-scale volume fraction is equal to 1.00. The multi-scale topology optimization problem degenerates to a single-scale optimization problem. It means that the optimal periodic cellular material is ev-

erywhere in the macro-scale design domain. The comparisons between multi-scale optimization and single meso-scale optimization are shown in Table 2.1. Comparing the results shown in Table 2.1, when single-scale optimization is applied, the structural SE is 335.0537 with structure mass 0.400. When multi-scale optimization is adopted, the second and third row in Table 2.1 show the topological structures with similar performance while the structure masses are 31.25% and 25.00 % lighter than the homogeneous materials. If the structures are subjected to same mass constraint, the structural SE of periodic cellular materials is 48.64 % less than the homogeneous materials. Those results indicate that the multi-scale optimization is more efficient than single-scale optimization for higher material savings and increased performance.

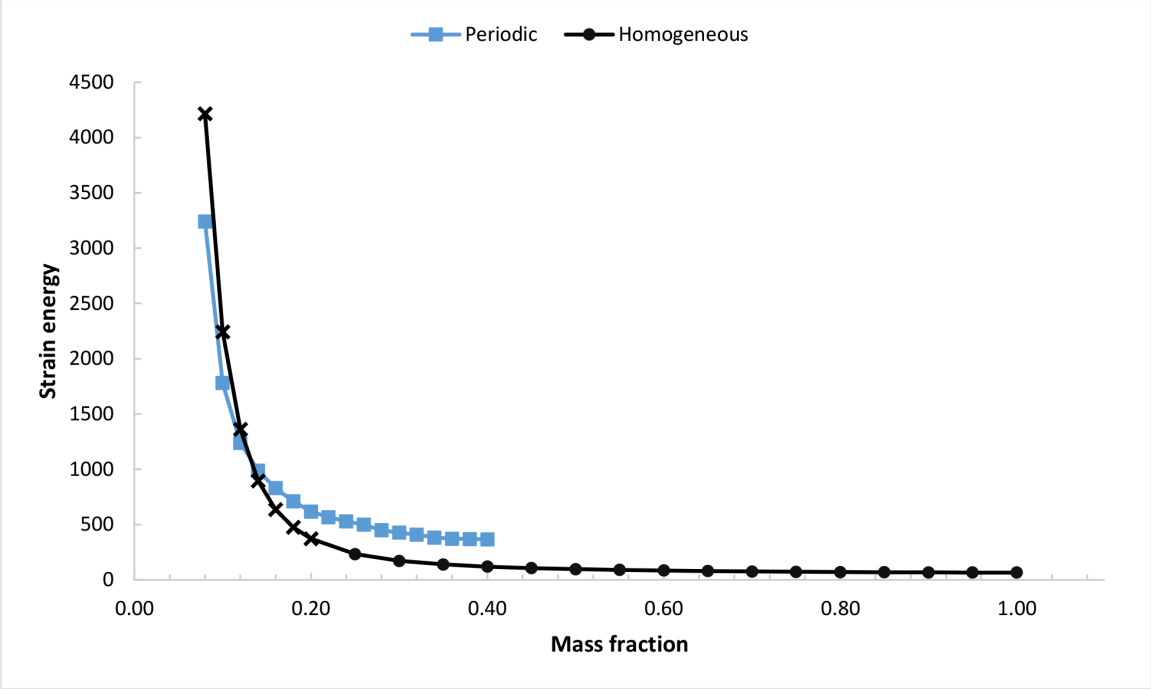

Figure 2.13. Pareto front for fixed meso-scale mass fraction.

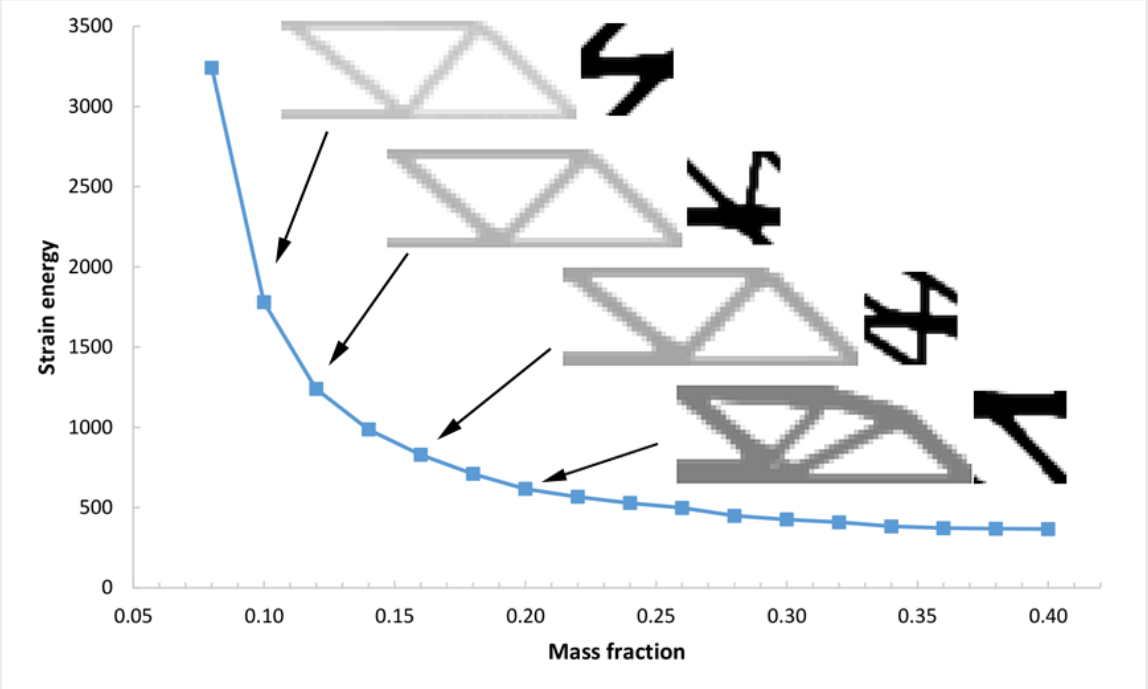

Figure 2.14. Selective topologies for structures using periodic cellular materials with fixed meso-scale mass fraction.

Table 2.1. Topology design of multi-scale and single-scale optimization.

$\bar{\Omega}$	$\bar{Y}$	SE	Mass	Macro-structure	Meso-structure	
					Cell	Tiled 4x4
1.00	0.40	355.0567	0.400			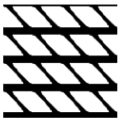
0.50	0.55	375.7559	0.275			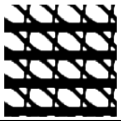
0.50	0.60	321.9504	0.300			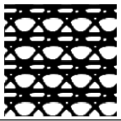
0.50	0.80	182.3487	0.400		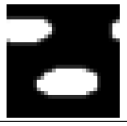	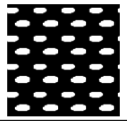

2.4 Topology Optimization for Compliant Synthesis

A compliant mechanism is a morphing structure that undergoes elastic deformation to transform force, displacement, or energy.

2.4.1 Optimization Problem Statement

A typical goal for a compliant mechanism design is to maximize the output port displacement, measured by the Mutual Potential Energy (MPE), which is defined as

$$u_{out} = \text{MPE} = \int_{\Omega} \sigma_d : \epsilon \; d\Omega, \tag{2.52}$$

where σ_d is the stress field produced by a unit dummy load and ϵ is the strain field due to the input load. The expression for MPE can be approximated using the FE method

$$u_{out} = \text{MPE} = \mathbf{U}_d^{\text{T}} \; \mathbf{K}(\mathbf{x}, \mathbf{y})^{\text{H}} \; \mathbf{U}, \tag{2.53}$$

where $\mathbf{U}_d$ is the virtual displacement vector cased by the dummy load and is given by

$$\mathbf{K}(\mathbf{x}, \mathbf{y})^{\text{H}} \; \mathbf{U}_d = \mathbf{L}, \tag{2.54}$$

where $\mathbf{L}$ is a unit length vector with zeros in all dimensions expect for one at the output point.

Hence, the optimization problem to solve compliant synthesis is

$$\begin{aligned}
\text{find} \quad & \mathbf{X} = \{\mathbf{x}, \mathbf{y}\} \\
\min \quad & -u_{out} = -\text{MPE} = -\sum_{i=1}^{N} (\text{MPE})_i = -\sum_{i=1}^{N} \mathbf{U}_{di}^{\text{T}}\ \mathbf{K}_i^{\text{H}}(x_i, \mathbf{y})\ \mathbf{U}_i \\
\text{subject to} \quad & \mathbf{K}^{\text{H}}(\mathbf{x}, \mathbf{y})\ \mathbf{U} = \mathbf{F} \\
& g_1(\mathbf{x}) = \frac{\Omega_e}{\Omega_0} \sum_{i=1}^{N} x_i - \bar{\Omega} \leqslant 0 \\
& g_2(\mathbf{y}) = \frac{Y_e}{Y_0} \sum_{j=1}^{n} y_j - \bar{Y} \leqslant 0 \\
& 0 \leqslant x_i \leqslant \bar{Y}, \quad i = 1, \ldots, N \\
& 0 \leqslant y_j \leqslant 1, \quad j = 1, \ldots, n
\end{aligned} \tag{2.55}$$

where $\mathbf{U}_{di}$ is the virtual displacement vector corresponding to element i.

2.4.2 Sensitivities of the Objective Function

The sensitivities of the objection function in Eq. 2.55 have similar expression as the SE problem. And the resulting sensitivities are

$$\frac{\partial \text{MPE}}{\partial x_i} = -p x_i^{p-1} (\text{E} - \text{E}_{\min}) \mathbf{U}_{di}^{\text{T}}\ [\mathbf{K}_i^{\text{H}}(\mathbf{y})]^0\ \mathbf{U}_i, \tag{2.56}$$

$$\frac{\partial \text{MPE}}{\partial y_j} = -\sum_{i=1}^{N} \text{E}_i(x_i)\ \mathbf{U}_{di}^{\text{T}} \left[\int_{\Omega_i} \mathbf{B}^{\text{T}} \frac{\partial [\mathbf{C}^{\text{H}}(\mathbf{y})]^0}{\partial y_j} \mathbf{B}\ d\Omega \right] \mathbf{U}_i. \tag{2.57}$$

2.4.3 Numerical Example

A well-known example: the Force Inverter [1] is considered as a example of compliant synthesis. The design domain for the force inverter is sketched in Fig. 2.15. The goal is the maximization of the output displacement in the negative horizontal direction due to an input load of $f_{in} = 1$ in the positive direction for different predefined volume fraction of macro- and meso-scale. Due to symmetry, the lower half of the design domain has modeled and discretized into 50×25 elements, and the meso-scale

design domain is discretized into 40×40 elements. The macro-scale design domain for structure with homogeneous materials is discretized into 100×50 elements. The filter size of macro-scale is 0.03 times the width of the design domain, and 0.04 times the width of meso-scale design domain for meso-scale. The input and output springs have a stiffness of 0.01 and 0.01.The base material has elastic modulus $E_0 = 1.0$ and Poisson's ratio $\nu = 0.3$.

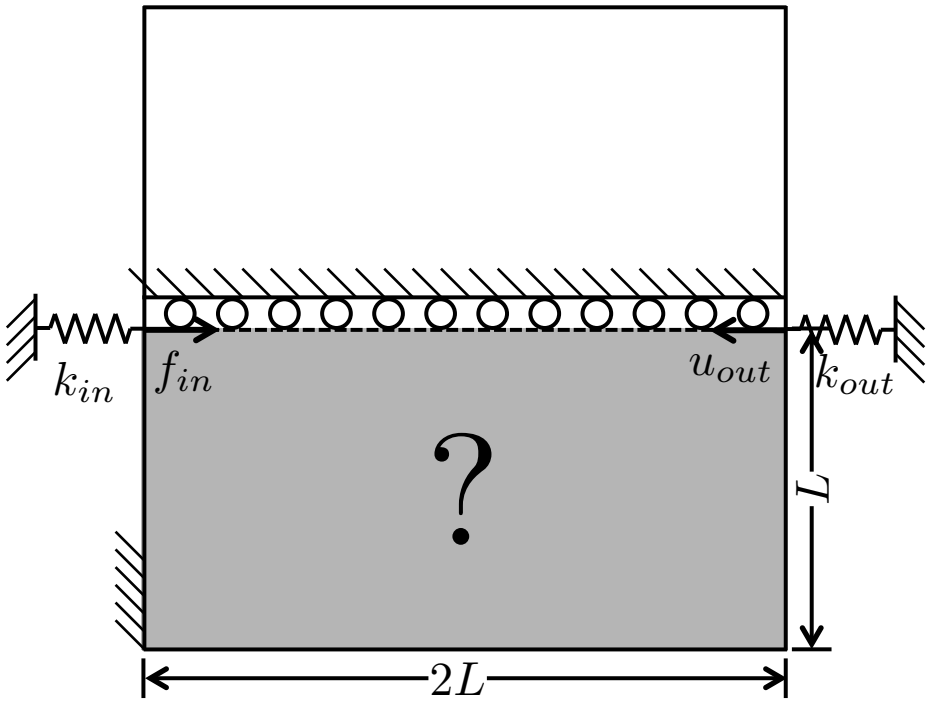

Figure 2.15. Initial design domain for force inverter.

The macro-scale volume fraction of structure with cellular materials $\bar{\Omega}$ is prescribed to 0.30. The periodic cellular materials volume fraction starts with 0.15 with step size 0.015 until the maximum volume fraction is reached, this means the periodic cellular materials become a homogeneous materials. On the other hand, the volume fraction of the structure with homogeneous materials ranges from 0.15 to 1.00. Due to the final designs of cellular materials been highly dependent on the initial design variables of meso-scale, we run the multi-scale topology optimization problem four

times for each identical condition except the initial design variables for meso-scale design domain $\mathbf{y}^{(0)}$ and take the average of the results.

The Mass-M_{nd} plot is shown in Fig. 2.16. In this example, we found that when M_{nd} is greater than 15% the optimized topologies of structures with homogeneous materials become gray structures. When M_{nd} is within 7%, the structures are clear black-and-white with few grays. Based on this observation, we abandon some results (marked as '$\times$' in Fig. 2.17) which are undesirable and unreliable with high percentage of gray structures exist and system performance is poor. One can get better results by either increasing the penalization power(s) and/or increasing the resolution of design domain.

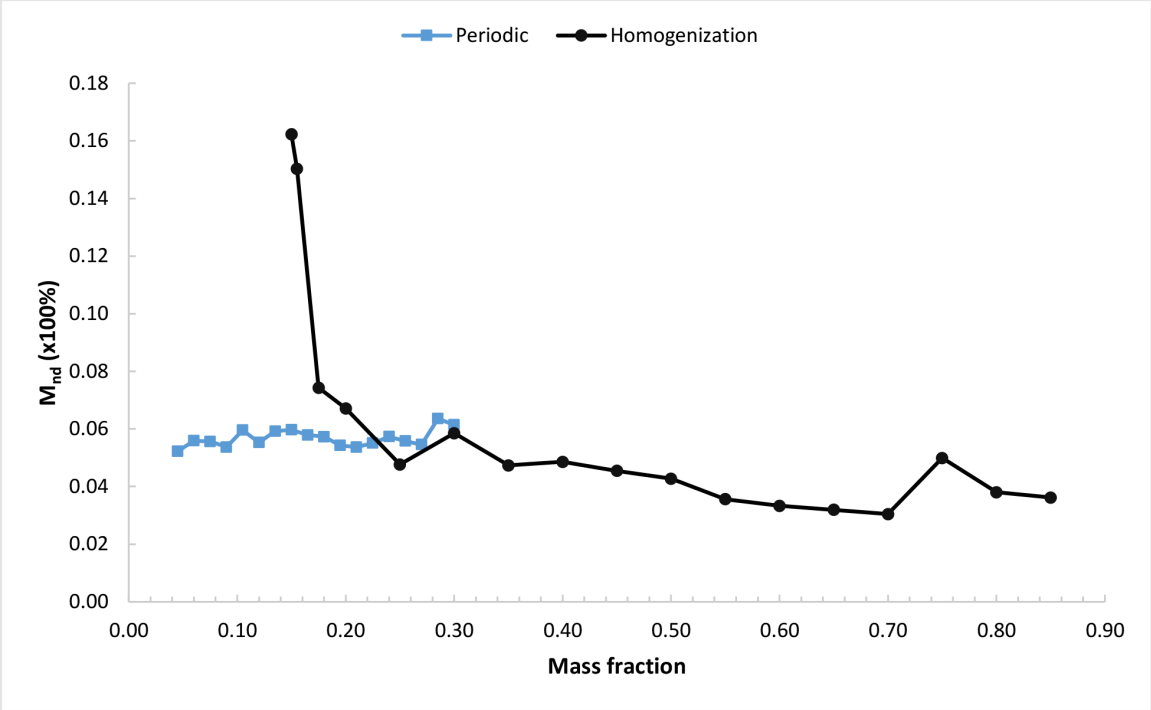

Figure 2.16. Measure of discreteness for force inverter.

Figure 2.17 shows the Pareto fronts for the force inverter design. Same as the design of stiff structure, on the ultra-light structure areas (mass fraction is less than 0.16 in this example), the structural performance and topology of homogeneous ma-

terials are undesirable and unreliable. However, we could get good results in these are with the usage of periodic cellular materials in structure. One interesting observation is that, the trend of Pareto fronts of periodic cellular materials and homogeneous materials are quite different. Some selective results are shown in Fig. 2.18.

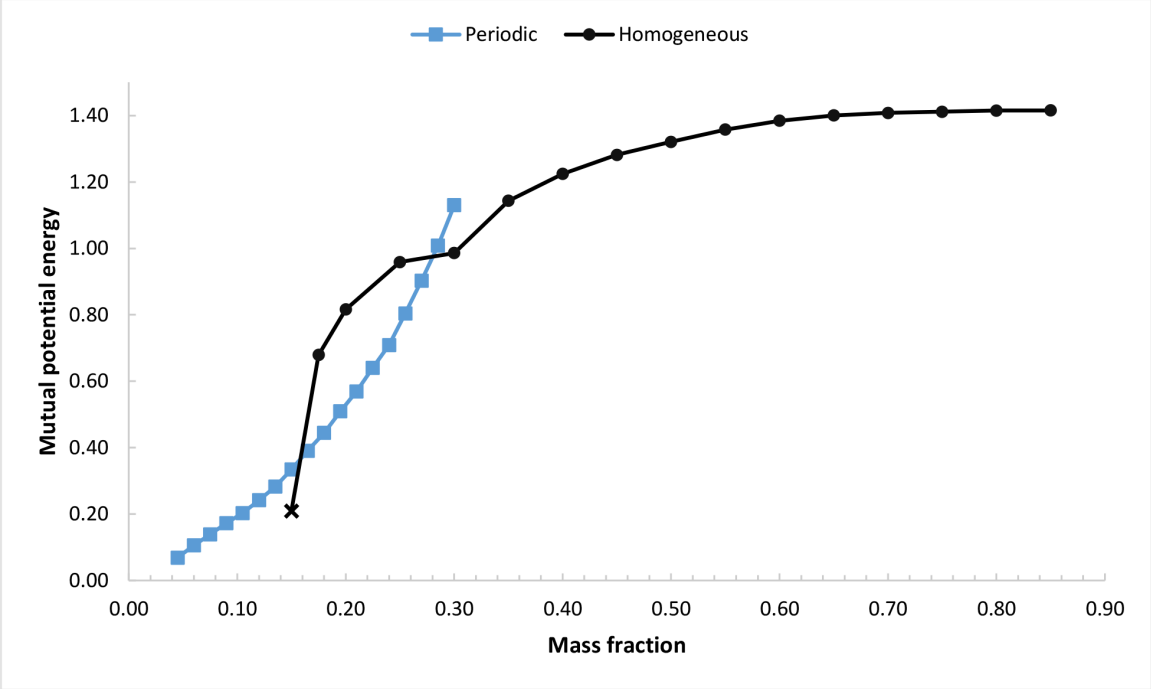

Figure 2.17. Pareto fronts for force inverter.

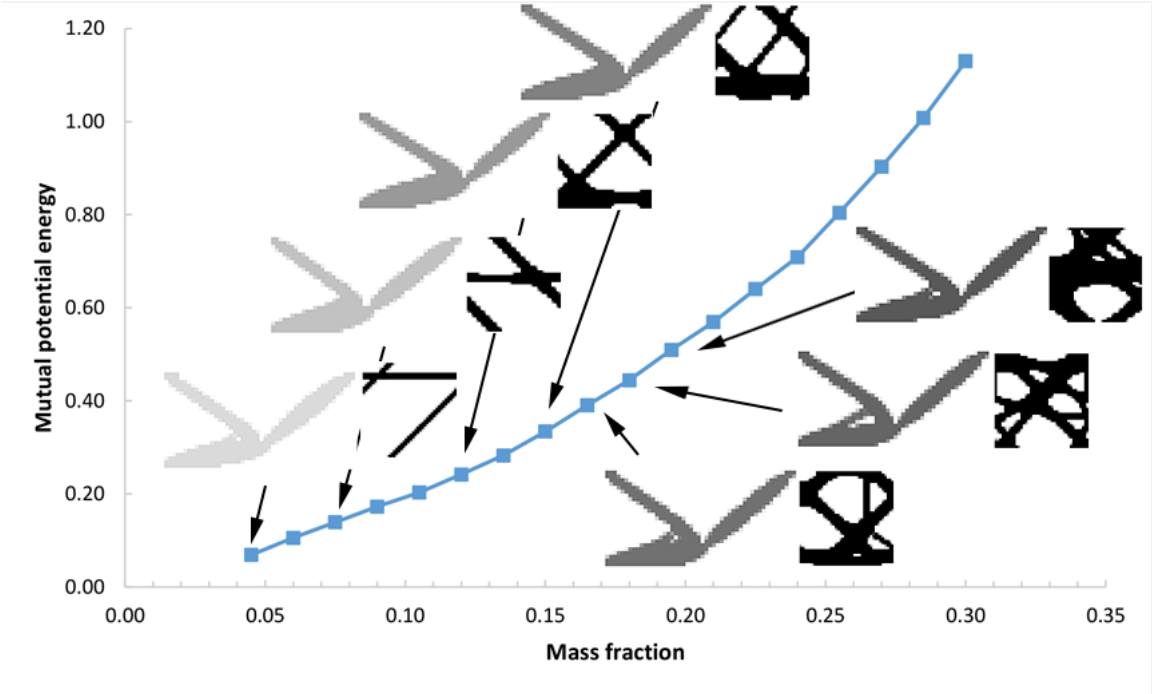

Figure 2.18. Selective topologies of structure with periodic cellular materials.

3. NON-PERIODIC MESO-STRUCTURES

From the results of Pareto fronts shown in the last chapter, we notice that the usage of periodic cellular materials have some advantages. For example, the optimized beam on both the macro and meso-scales are black-and-white structures which is what we expect. However, although using the homogeneous materials results in gray structure, the structural performance in some cases are still better than the periodic cellular materials. The optimized structure and material topologies has been achieved through the multi-scale topology optimization approach discussed above. However, the material topology is optimized based on the overall structure objective; in other words, the meso-structure is uniform over the macro-scale. If we can optimize every element on the macro-scale to derive meso-structure points wisely, what will happen? Will the optimized topology be completely different? Will the structural performance be better than the periodic cellular materials? Will the structural performance be even better than the homogenous material? Those are the main problems we intend to solve in this chapter.

3.1 Problem Statement

The method incorporated in this chapter is derived from the one originally introduced by [35]. The topology optimization problem is decomposed into two related sub-problems. The macro-scale problem corresponding to find the optimal material distribution on macroscopic level for a prescribed design domain and given set of boundary conditions and loading conditions, while the meso-scale problem addresses the optimal meso-structure morphology of every element on macro-scale. Therefore, this methodology is no longer a classical single scale topology optimization problem, instead a multiscale (hierarchical) problem of structure and material design. Two

scales are linked to each other by homogenization theory as discussed in the previous chapter. The effective material properties of meso-structure are derived through the standard homogenization method, while the structure analysis of macro-scale required the information of meso-structure material properties.

3.1.1 Formulation of the Optimization Problem on Macro-scale

An optimization problem on macro-scale including the features mentioned above can be written as

$$\begin{aligned} \text{find} \quad & \mathbf{x} \\ \min \quad & \mathcal{P}(\mathbf{x}, \mathbf{y}^1, \mathbf{y}^2, \ldots, \mathbf{y}^N) \\ \text{subject to} \quad & \mathbf{K}^{\mathrm{H}}(\mathbf{x}, \mathbf{y}^1, \mathbf{y}^2, \ldots, \mathbf{y}^N)\ \mathbf{U} = \mathbf{F} \\ & g_1(\mathbf{x}) = \frac{\Omega_e}{\Omega_0} \sum_{i=1}^{N} x_i - \bar{\Omega} \leqslant 0 \\ & 0 \leqslant x_i \leqslant 1, \quad i = 1, \ldots, N \end{aligned} \tag{3.1}$$

where $\mathbf{x}$ is the vector of macro-scale design variables (i.e. the element densities). $\mathbf{K}^{\mathrm{H}}$ is the homogenized global stiffness matrix dependent on two scales. $\mathbf{U}$ and $\mathbf{F}$ are the global displacement and force vector. $\mathbf{y}^i$ is the meso-scale design variables. Ω_e and Ω_0 are the material volume and design domain volume in macro-scale. N is the number of elements used to discretize the macro-scale design domain Ω. $\bar{\Omega}$ is the prescribed volume fraction on macro-scale, respectively.

If we comparing Eq. 2.13 and Eq. 3.1, we might found out that they are quite similar, the differences is: for the periodic case, the meso-scale design variable matrix has only one, but for the non-periodic case the number of meso-scale design variable matrix is same as number of elements used to discretize the macro-scale design domain.

3.1.2 Formulation of the Optimization Problem on Meso-scale

Generally, the structural property(-ies) $\mathcal{P}$ [e.g. Strain Energy (c.f. Sec. 2.3), Mutual Potential Energy (c.f. Sec. 2.4)] is a summation of the property(-ies) of every component in the structure $\mathcal{P}_i$. Apparently, if we want to minimize a summation, we need to minimize every component of the summation. In the spirit of this, we take advantage of topology optimization methods to find the morphologies of meso-structures.

Given element density x_i and some necessary information from macro-scale $\mathcal{I}(\mathbf{x})$ at each spatial point i on macro-scale, we want to minimize the element properties $\mathcal{P}_i$. Therefore, the meso-scale topology optimization problem for each spatial point i on macro-scale with density x_i can be stated as below

$$\begin{aligned} \text{given} \quad & x_i, \mathcal{I}(\mathbf{x}) \\ \text{find} \quad & \mathbf{y}^i \\ \min \quad & \mathcal{P}_i(x_i, \mathbf{y}^i, \mathcal{I}(\mathbf{x})) \\ \text{subject to} \quad & \mathbf{k}(\mathbf{y}^i)\boldsymbol{\chi}^{kl} = \mathbf{f}^{kl} \\ & g_1(\mathbf{y}^i) = \frac{Y_e}{Y_0}\sum_{j=1}^{n} y_j^i - x_i \leqslant 0 \\ & 0 \leqslant y_j^i \leqslant 1, \quad j = 1, \ldots, n \end{aligned} \tag{3.2}$$

3.2 Numerical Implementation Issues

This section describes the numerical implementation issues of the incorporated mutli-scale topology optimization problem such as initialization, regularization techniques, discontinuities, etc. A program flow chart of the proposed design algorithm is shown in Fig. 3.1 and each individual step of the algorithm is described in the following.

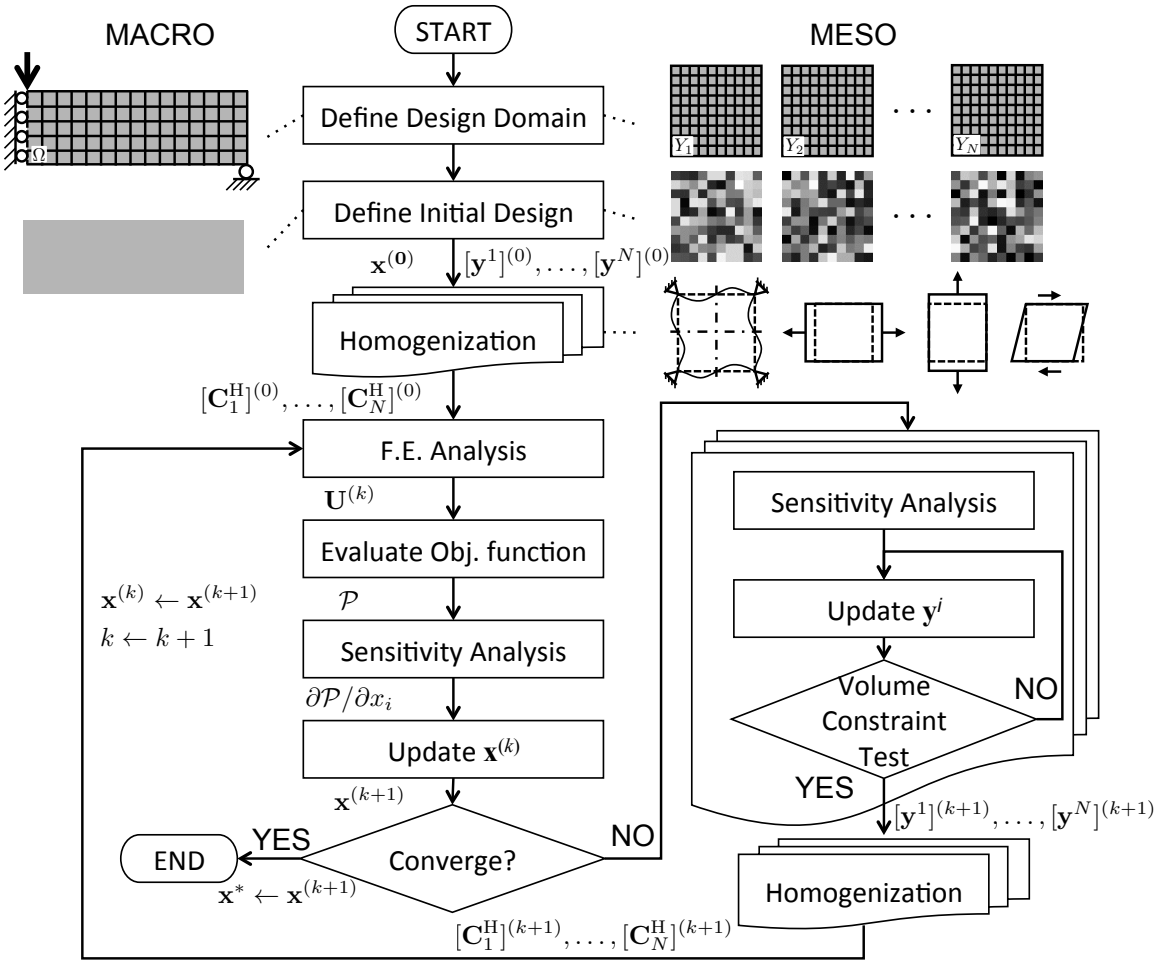

Figure 3.1. Programming flow chart.

3.2.1 Initialization

First we discretize the macro-scale design domain Ω into N elements and the meso-scale design domains Y_i into n elements. Define the boundary conditions and the loading conditions of the macro-structures. Provide the base material properties elastic modulus E_0 and Poisson's ratio ν.

3.2.2 Starting Guess

The initial points of design variables in macro-scale $\mathbf{x}^{(0)}$ can be set uniform with value of macro-scale volume fraction $\bar{\Omega}$. The initial design variables for meso-scale problems $[\mathbf{y^i}]^{(0)}$ must be chosen from a random density distribution. The reason is discussed earlier. However, the optimization procedure can be improved significantly if a good set of initial points can provide to the program.

In order to have a good start, we are solving a small multi-scale topology optimization problem and using the results as the staring points. One should note that this methodology is only applied on convex objective functions. The algorithm is shown in Fig. 3.2 and can be summarized below:

Step 1. A traditional macro-scale topology optimization problem is solved with same boundary conditions, loading conditions, mesh size and material properties as we defined in the initialization step. Since there is no penalization method applied on the macro-scale, the objective function is a convex function which ensures the final results are the global minimum.

Step 2. A total number of N meso-scale optimization problems are solved to find the optimal meso-structure corresponding to the macro-scale solution in *Step 1.*

3.2.3 Homogenization Step

Homogenization method used in this procedure is same as those we discussed before. Please refer to Sec. 2.2.4 for further details.

3.2.4 Regularization Techniques

In order to avoid numerical instabilities, the standard density filter is implemented in the program. The density filter already discussed in previous section. For convince, we restate the equations here

$$\tilde{X}_e = \frac{\sum \omega \; v_e \; X_e}{\sum \omega \; v_e}, \tag{3.3}$$

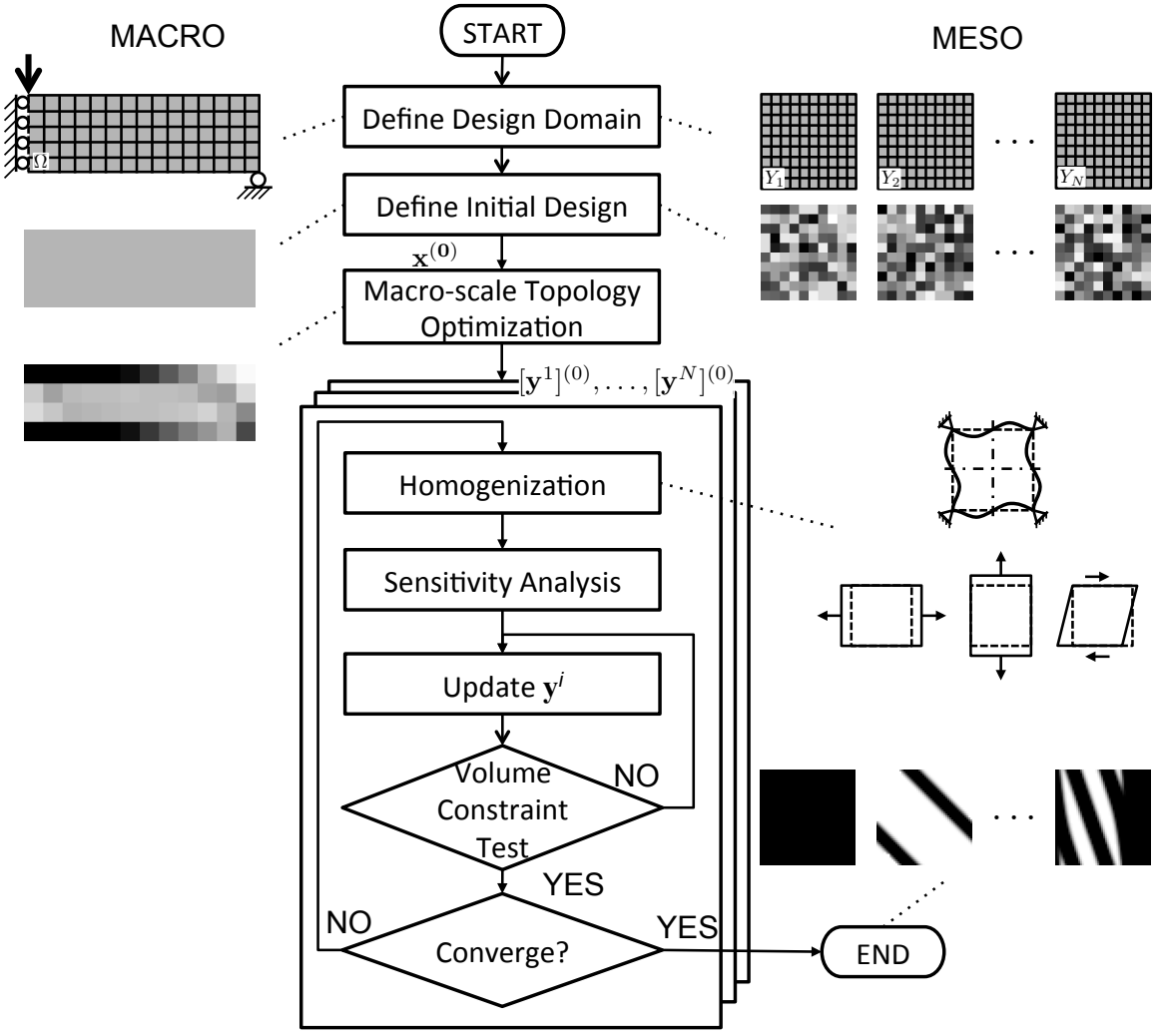

Figure 3.2. Initial points strategy.

where v_e and X_e denotes the volume and density of design variable e. The weight factor ω is given by a linear function as suggested in [50], by

$$\omega = \max\{0,\ r_{\min} - \mathrm{dist}(e,h)\}, \quad \{h \in N(\text{or } n) \mid \mathrm{dist}(e,h) \leqslant r_{\min}\}, \tag{3.4}$$

where the operator $\mathrm{dist}(e,h)$ is defined as the distance between center of element e and center of element h. $r_{\min}$ is the radius or filter size.

3.2.5 Discontinuities

If the meso-structure is assumed identical over macro-scale, there is normally no connection problem between adjacent elements on macro-scale level because the unit cell is imposed with periodic boundary conditions (Fig. 3.1). However, in our study, the meso-structures vary pointwise. From numerical experiments, discontinuities exist between adjacent elements. To address this problem, we proposed a method which converts the distributed load on meso-scale boundaries to 2 concentrated loads on each boundary. This method is illustrated in Fig. 3.3. Figure 3.4 shows the two optimized topologies for different loading cases. There are some differences shown in the meso-structures of two loading cases. However, undesirable element boundaries are generated in the final topologies with the use of concentrated loading cases.

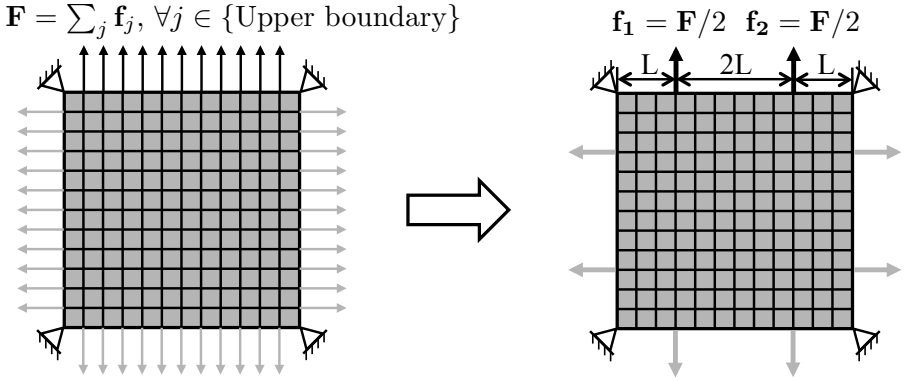

Figure 3.3. Distributed load to Concentrated load.

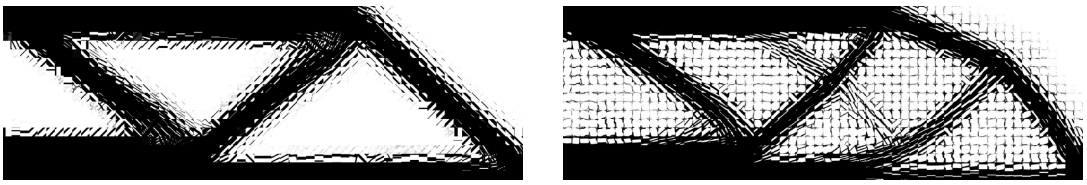

(a) Distributed loading cases. (b) Concentrated loading cases.

Figure 3.4. Resulting topologies for different loading cases.

3.3 Topology Optimization for Stiff Structure

The topology optimization problem and numerical examples of design of stiff structure with non-periodic cellular material are discussed in this section.

3.3.1 Optimization Problem Statement

The optimization problem for stiff structure design on macro-scale is

$$\begin{aligned} \text{find} \quad & \mathbf{x} \\ \min \quad & \text{SE} = \sum_{i=1}^{N} (\text{SE})_i = \sum_{i=1}^{N} \mathbf{U}_i^{\text{T}} \ \mathbf{K}_i^{\text{H}}(x_i, \mathbf{y}^i) \ \mathbf{U}_i \\ \text{subject to} \quad & \mathbf{K}^{\text{H}}(\mathbf{x}, \mathbf{y^1}, \mathbf{y^2}, \ldots, \mathbf{y^N}) \ \mathbf{U} = \mathbf{F} \\ & g_1(\mathbf{x}) = \frac{\Omega_e}{\Omega_0} \sum_{i=1}^{N} x_i - \bar{\Omega} \leqslant 0 \\ & 0 \leqslant x_i \leqslant 1, \quad i = 1, \ldots, N \end{aligned} \tag{3.5}$$

Given the element displacement vector $\mathbf{U}_i$ and element density x_i at each spatial point i on macro-scale, we want to minimize the element SE. Therefore, the meso-scale topology optimization problem for each spatial point i on macro-scale with density x_i can be stated as below

$$\begin{aligned} \text{given} \quad & x_i, \mathbf{U}_i \\ \text{find} \quad & \mathbf{y}^i \\ \min \quad & (\text{SE})_i = \mathbf{U}_i^{\text{T}} \ \mathbf{K}_i^{\text{H}}(x_i, \mathbf{y}^i) \ \mathbf{U}_i \\ \text{subject to} \quad & \mathbf{k}(\mathbf{y}^i)\boldsymbol{\chi}^{kl} = \mathbf{f}^{kl} \\ & g_1(\mathbf{y}^i) = \frac{Y_e}{Y_0} \sum_{j=1}^{n} y_j^i - x_i \leqslant 0 \\ & 0 \leqslant y_j^i \leqslant 1, \quad j = 1, \ldots, n \end{aligned} \tag{3.6}$$

3.3.2 Numerical Examples

The same MBB problem is solved for the case of non-periodic cellular materials as we did in the previous chapter. The details of the problem is defined in the Sec. 2.3.4

Meso-scale Mesh Size Effect

The main objective of this example is to analyze the influence of the mesh size for the meso-scale design domain in the overall structure topologies and in the objective function. As reference, the topology for the homogeneous material is with objective value 207.8551. The meso-scale design domains have different mesh sizes with 20×20, 30×30, 40×40, 50×50, and 60×60 finite elements. As it can be seen from Fig. 3.5, the connection between adjacent elements in macro-scale is smoother with the increasing of mesh size of meso-scale. Figure 3.5 shows the final topologies are mesh-independent, which means the differences between different meso-scale design domain mesh sizes are minor. However, the meso-structures are quite different in different mesh sizes. As predicted, as the discretization of the meso-scale design domain increases, there is an improvement on the overall structural performance see Fig. 3.6.

Periodic vs. Non-periodic vs. Homogeneous

In the previous chapter, we found that the structures with periodic cellular materials on macro-scale level can not completely replace the homogeneous materials especially when higher structural performances are required. However, cellular materials can be used to achieve ultra-lightweight structure with clear black-and-white topologies. In this example, we want to compare the structural performance with structures using periodic cellular materials, non-periodic cellular materials and homogeneous materials.

The details of the problem setting for periodic cellular materials and homogeneous materials can be found in Sec 2.3.4. For the non-periodic problem, the macro-scale

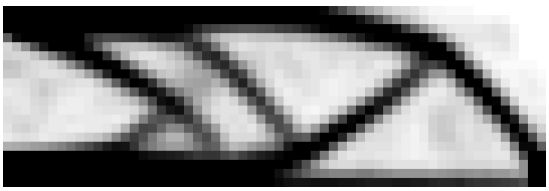

(a) Macro-scale density distributions (20×20).

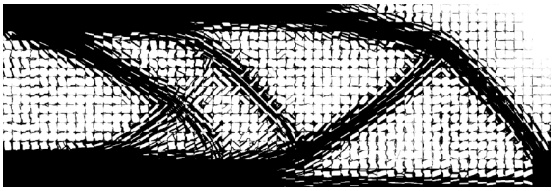

(b) Resulting topology optimized beam (20×20).

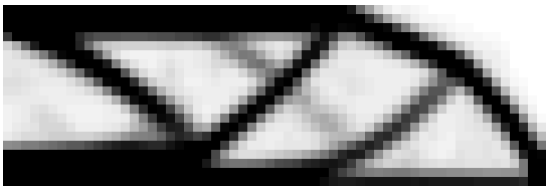

(c) Macro-scale density distributions (30×30).

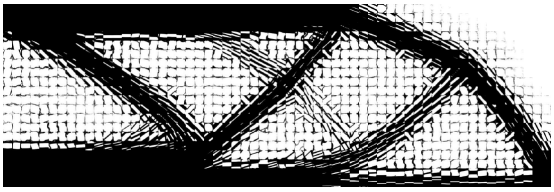

(d) Resulting topology optimized beam (30×30).

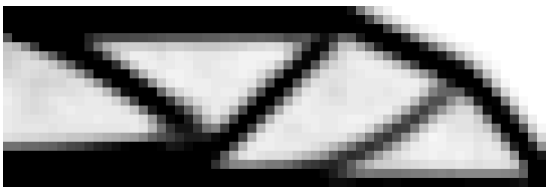

(e) Macro-scale density distributions (40×40).

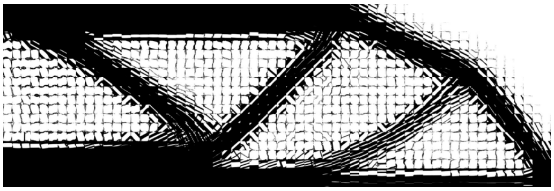

(f) Resulting topology optimized beam (40×40).

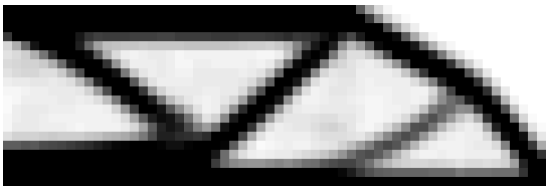

(g) Macro-scale density distributions (50×50).

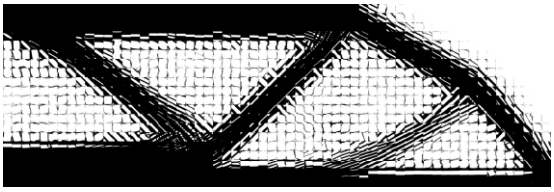

(h) Resulting topology optimized beam (50×50).

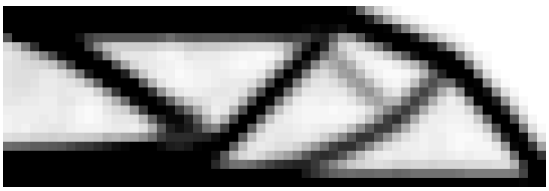

(i) Macro-scale density distributions (60×60).

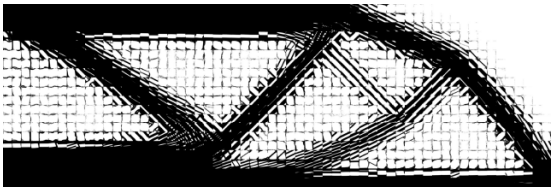

(j) Resulting topology optimized beam (60×60).

Figure 3.5. Selective results for MBB-beam.

design domain is discretized into 30×10 elements, and meso-scale design domain is discretized into 20×20 elements. The Pareto fronts are shown in Fig. 3.7. Speaking to the structural performances as shown in Fig. 3.7, non-periodic materials have

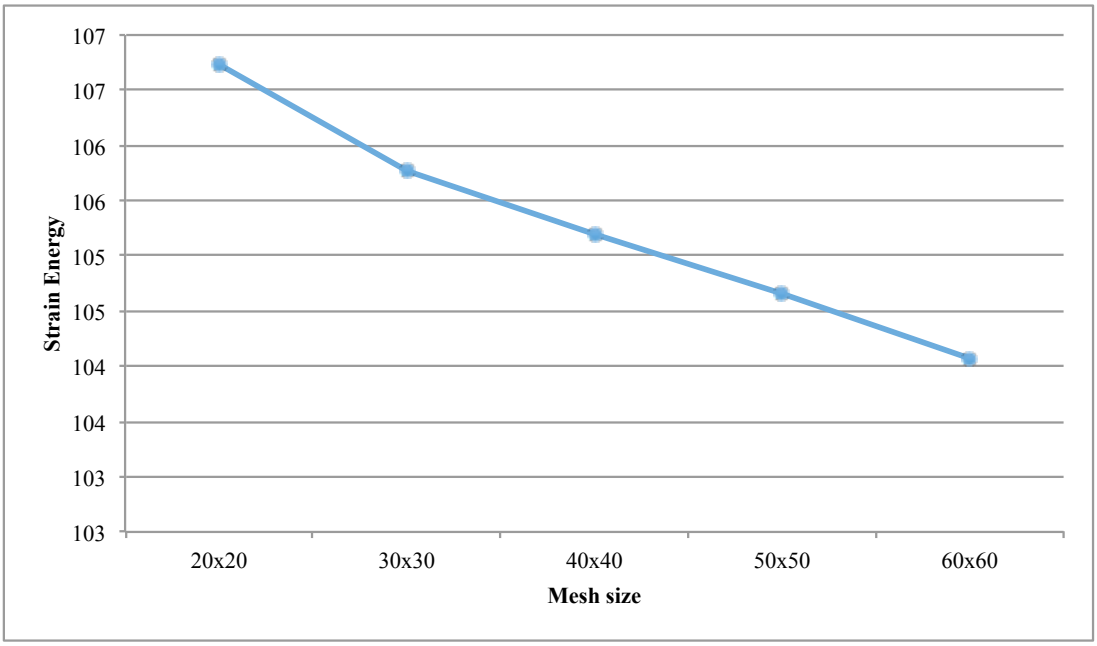

Figure 3.6. SE versus mesh size.

better structural performance compared to the periodic materials. However, when mass fractions are bigger than 0.25 in this example, the structures with homogeneous materials are more preferable (for reason c.f. Sec. 2.3.4) if we combine the structure performance with computing time.

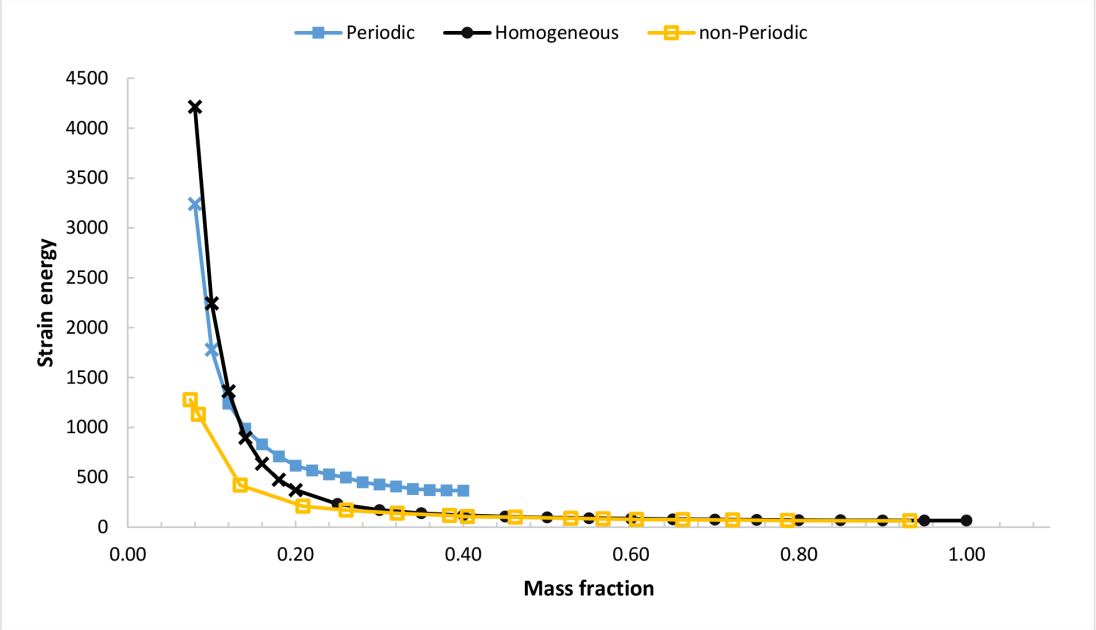

Figure 3.7. Pareto fronts of MBB-beam.

3.4 Topology Optimization for Compliant Mechanism Synthesis

The topology optimization problem and numerical examples of compliant mechanism design with non-periodic cellular material are discussed in this section.

3.4.1 Optimization Problem Statement

The topology optimization problem for compliant synthesis on macro-scale can be defined as

$$\begin{aligned}
&\text{find} && \mathbf{x} \\
&\min && -u_{out} = -\text{MPE} = -\sum_{i=1}^{N}(\text{MPE})_i = -\sum_{i=1}^{N}\mathbf{U}_{di}^{\text{T}}\ \mathbf{K}_i^{\text{H}}(x_i,\mathbf{y}^i)\ \mathbf{U}_i \\
&\text{subject to} && \mathbf{K}^{\text{H}}(\mathbf{x},\mathbf{y^1},\mathbf{y^2},\ldots,\mathbf{y^N})\ \mathbf{U} = \mathbf{F} \\
&&& g_1(\mathbf{x}) = \frac{\Omega_e}{\Omega_0}\sum_{i=1}^{N} x_i - \bar{\Omega} \leqslant 0 \\
&&& 0 \leqslant x_i \leqslant 1, \quad i = 1,\ldots,N
\end{aligned} \tag{3.7}$$

Given the element displacement vector $\mathbf{U}_i$ cased by load input, the element virtual displacement vector $\mathbf{U}_{di}$ produced by dummy load and element density x_i at each spatial point i on macro-scale, the meso-scale topology optimization problem can be stated as below

$$\begin{aligned}
&\text{given} && x_i, \mathbf{U}_i, \mathbf{U}_{di} \\
&\text{find} && \mathbf{y}^i \\
&\min && -(\text{MPE})_i = -\mathbf{U}_{di}^{\text{T}}\ \mathbf{K}_i^{\text{H}}(x_i,\mathbf{y}^i)\ \mathbf{U}_i \\
&\text{subject to} && \mathbf{k}(\mathbf{y}^i)\boldsymbol{\chi}^{kl} = \mathbf{f}^{kl} \\
&&& g_1(\mathbf{y}^i) = \frac{Y_e}{Y_0}\sum_{j=1}^{n} y_j^i - x_i \leqslant 0 \\
&&& 0 \leqslant y_j^i \leqslant 1, \quad j = 1,\ldots,n
\end{aligned} \tag{3.8}$$

3.4.2 Numerical Examples

The force inverter problem is solved again in order to make comparison between homogeneous materials, periodic cellular materials and non-periodic cellular materials. The details of the example are defined in the Sec. 2.4.3. For the non-periodic part, the macro-scale is discretized into 50×25 elements and the meso-scale design domains have 20×20 elements.

Solving the small initial topology optimization problem as stated earlier (see Fig. 3.2) in compliant mechanism problem is not required, since the objective function of compliant mechanism is not convex, which means it cannot guarantee the minima is the global minima. The initial macro-scale design variables $\mathbf{x}^0$ are uniform with value of macro-scale volume fraction $\bar{\Omega}$. The initial design variables for meso-scale $[\mathbf{y}^i]^{(0)}$ start with a random density distribution and the final results are highly dependent on the initial design variables.

The optimized topology is shown in Fig. 3.8. There is a hinger exists in the multiscale optimized structure. The Pareto fronts of periodic cellular materials, non-periodic cellular materials and homogeneous materials are shown in Fig. 3.9. In Fig. 3.9, similar conclusion can be derived as the design of stiff structure problem, and non-periodic cellular materials show more gains than periodic cellular materials in compliant mechanism problems. The trend of Pareto front of non-periodic material is similar with the trend of homogeneous materials. When mass fraction is over 0.35 in this example, using homogeneous materials is more recommended due to the lower computational cost and higher structural performance.

(a) Macro-scale density distributions. (b) Resulting topology optimized force inverter.

Figure 3.8. Selective results for force inverter.

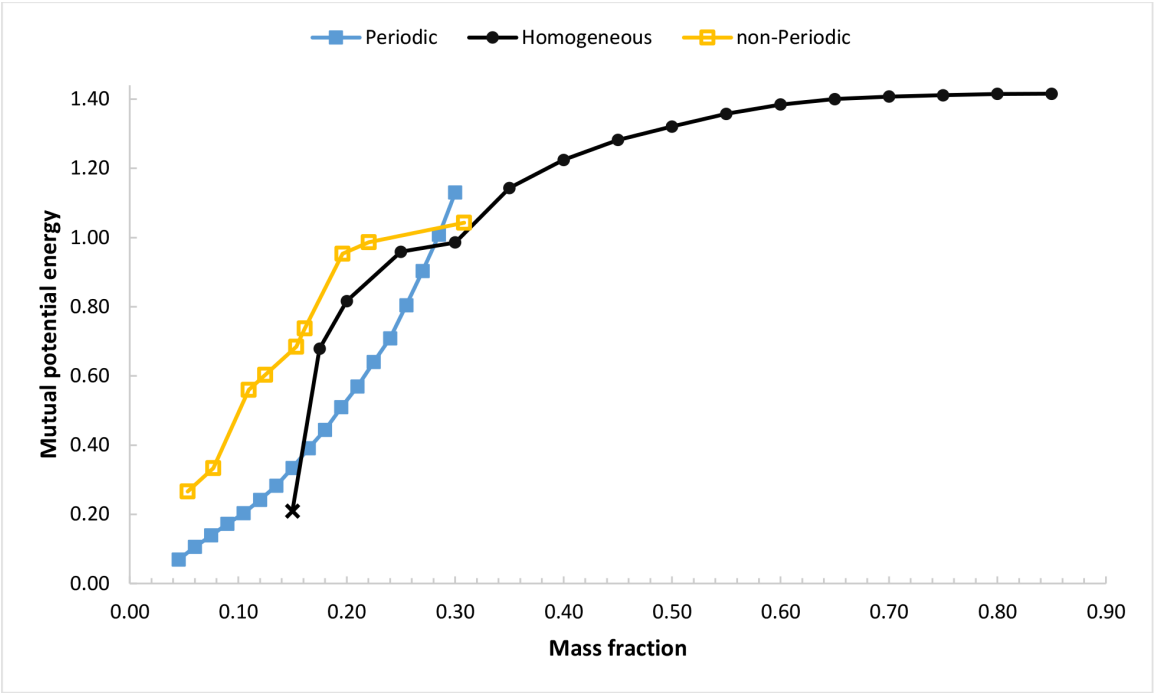

Figure 3.9. Pareto fronts of force inverter.

4. ERROR QUANTIFICATIONS

There are multiple types of errors involved in the structural analysis, for example, errors caused by finite elements, errors involved in the mesh refinement and errors from homogenization of meso-structure properties, etc. How to quantify those errors involved in the analysis is a significant issue. In the previous two chapters, all the structural analyses are based on the macro-scale FE densities and the homogenized meso-structure properties as shown in Fig. 4.1, and we refer those as multi-level designs. In the uni-level design, when we substitute every element on the macro-scale with its own optimized meso-structure, the final design domain becomes a huge domain as shown in Fig. 4.2. If we have the macro-scale design domain discretized into 60×20 elements and the meso-scale design domains into 20×20 elements, then the design domain for uni-level design will have $(60 \times 20) \times (20 \times 20)$ elements.

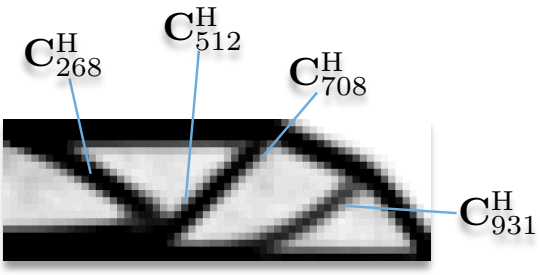

Figure 4.1. Illustration of multi-level design.

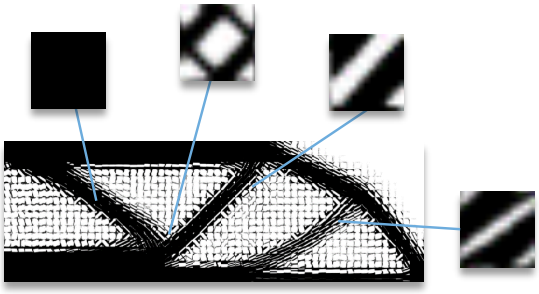

Figure 4.2. Illustration of uni-level design.

4.1 Mesh Refinement Error

In order to understand errors along with the FE mesh-refreshment, we solved the example in the design of stiff structures, and the problem is defined as shown in Fig. 2.8. However, the volume fraction in this example is 1.00 which means the macro-scale design domain is filled with homogeneous materials. The FE mesh size is chosen as 3×1, 6×2, 9×3, $\ldots$, 600×200. The FE mesh size versus Objective value (SE) are shown in Fig. 4.3. As we can see from this figure, the finer the FE mesh of the macro-scale, the higher the objective function.

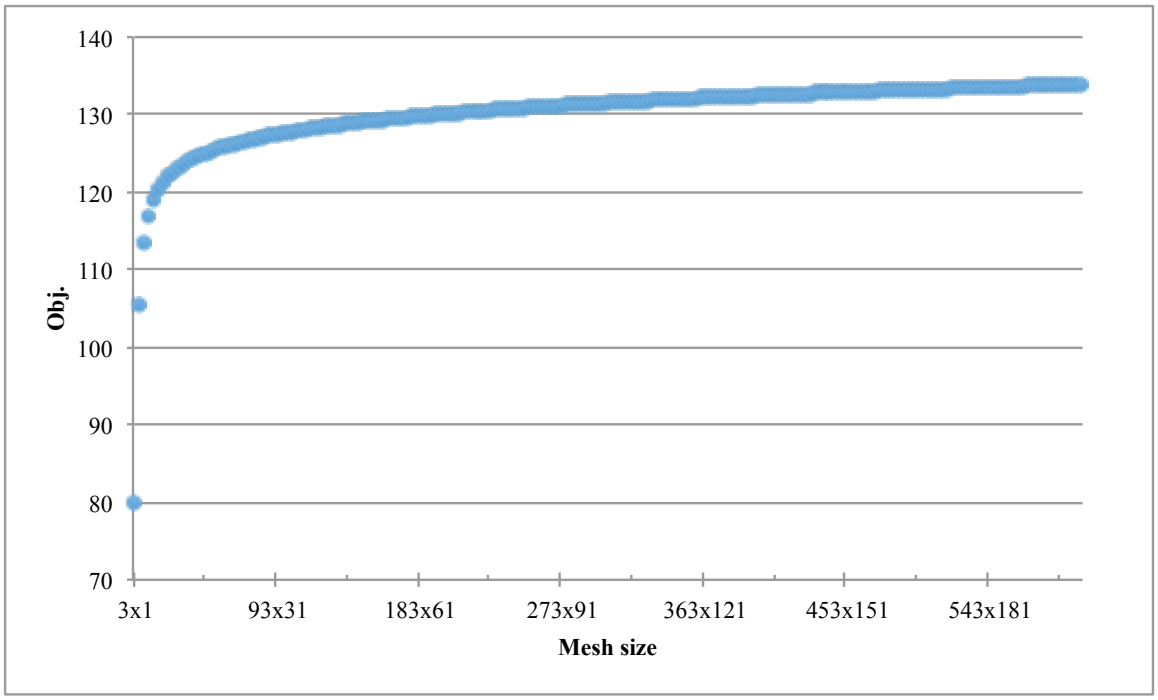

Figure 4.3. Mesh size vs. Objective: a solid structure example.

In our previous discussion, we learned that the meso-scale FE mesh has a positive effect on the structural performance. Tab. 4.1 shows the details of the error corresponding to the meso-scale FE mesh size and Fig. 4.4 shows the mesh-size versus error plot. The same conclusion can be reached as the meso-scale FE mesh size versus the

structural performance; The finer the meso-scale FE mesh size, the lower errors exist between the uni-level approach and the multi-level approach, which is as predicted.

Table 4.1. Meso-scale mesh refinement: a MBB-Beam example.

Macro	**Meso**	**Uni-level**	**Multi-level**	**Error (%)**
60×20	20×20	263.65	213.46	-23.51
	30×30	238.74	211.53	-12.86
	40×40	233.10	209.31	-11.37
	50×50	227.57	208.15	-9.33

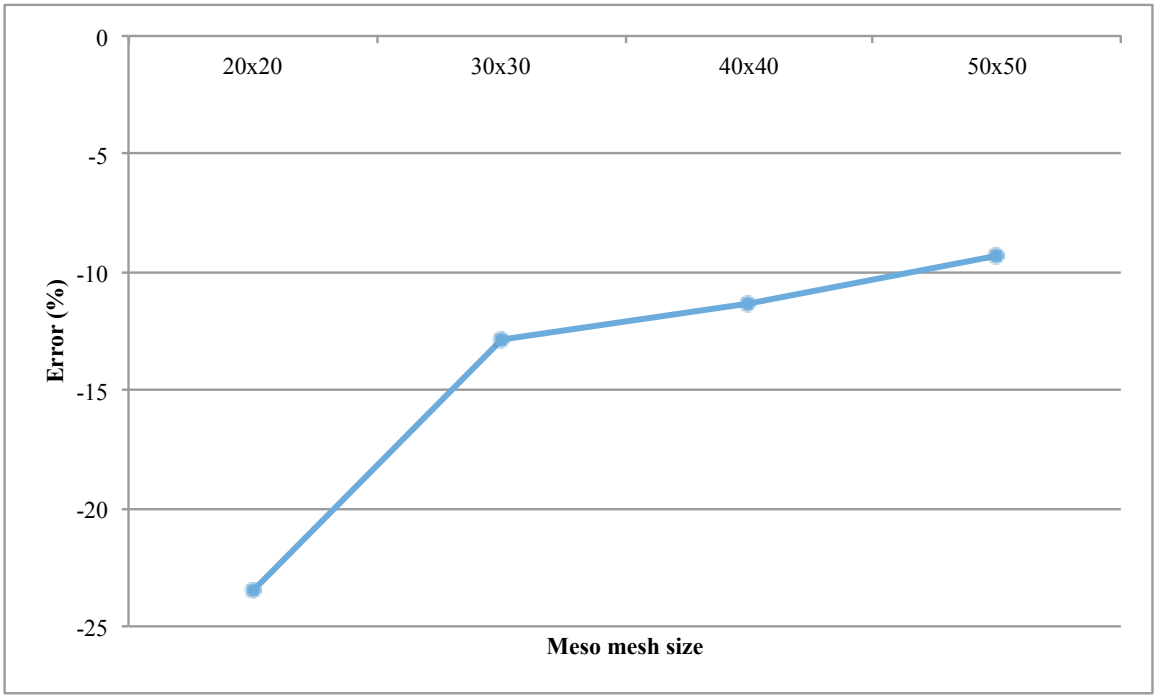

Figure 4.4. Meso-scale mesh refinement: a MBB-Beam example.

4.2 Homogenization Error

In this section, three different numerical examples are solved in order to reveal errors involved in the homogenization process. The basic idea in quantifying the homogenization error is shown in Fig. 4.5. Considering a structure which is constructed by 60×20 elements as shown in Fig. 4.5 in gray scale, one could gather the macro-scale elements into different groups. For example, in Fig. 4.5, we consider every 10×10 element in the macro-scale as a group (meso-structure); then new macro-scale design domain has 6×2 elements and each meso-scale design domain has 10×10 elements. One should note that in this process, the total number of elements used to discretize the design domain remains the same. Therefore, the macro-scale FE mesh size varies with the meso-scale FE mesh size as shown in Tab. 4.2. The meso-scale FE mesh size could be up to 20×20 elements. However, the ratio between meso-scale FE dimension and macro-scale FE dimension is extremely high. We know that the homogenization is based on the assumption that the ratio of the real length of a unit vector in the mesoscopic coordinates to the real length of a unit vector in the macroscopic coordinates is a small parameter ε [2]. Clearly, the ratio in this case is not a small number. Therefore, those ratios bigger than 1 are not considered in the analysis. The objective comparison plot for uni-level design and multi-level design are shown in Fig. 4.6. The errors involved in the homogenization procedure for solid structure are shown in Fig. 4.7.

As we can see, there are very tiny errors shows up in the homogenization of solid structure. What if those structures are not solid structure? There are two designs of stiff structure examples that followed: one is the MBB-Beam problem and the other is a cantilever beam problem.

4.2.1 MBB-Beam

The problem is solved as in Fig. 2.8 with volume fraction prescribed to be 0.50. The final topology is solved using the traditional topology optimization method with

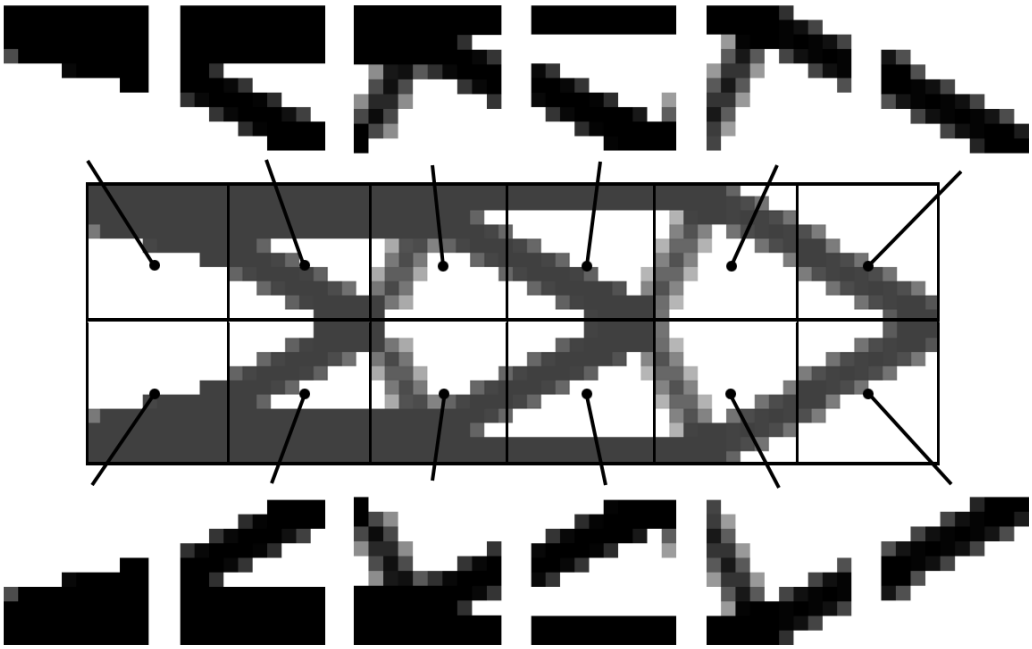

Figure 4.5. Macro-scale design domain partition.

Table 4.2. Macro-scale domain partition: a solid structure example.

Macro	**Meso**	ε	**Obj.**	**Error (%)**
60×20	1×1	0.001	125.68	0.16
30×10	2×2	0.01	123.13	-0.05
15×5	4×4	0.21	119.28	-0.25
12×4	5×5	0.52	117.40	-0.37
6×2	10×10	8.33	106.77	-1.25
3×1	20×20	133.33	82.96	-3.72

homogeneous materials shown in Fig. 4.8. We then use the method as we discussed in Fig. 4.5 to group elements in macro-scale and then homogenize those grouped meso-structures.

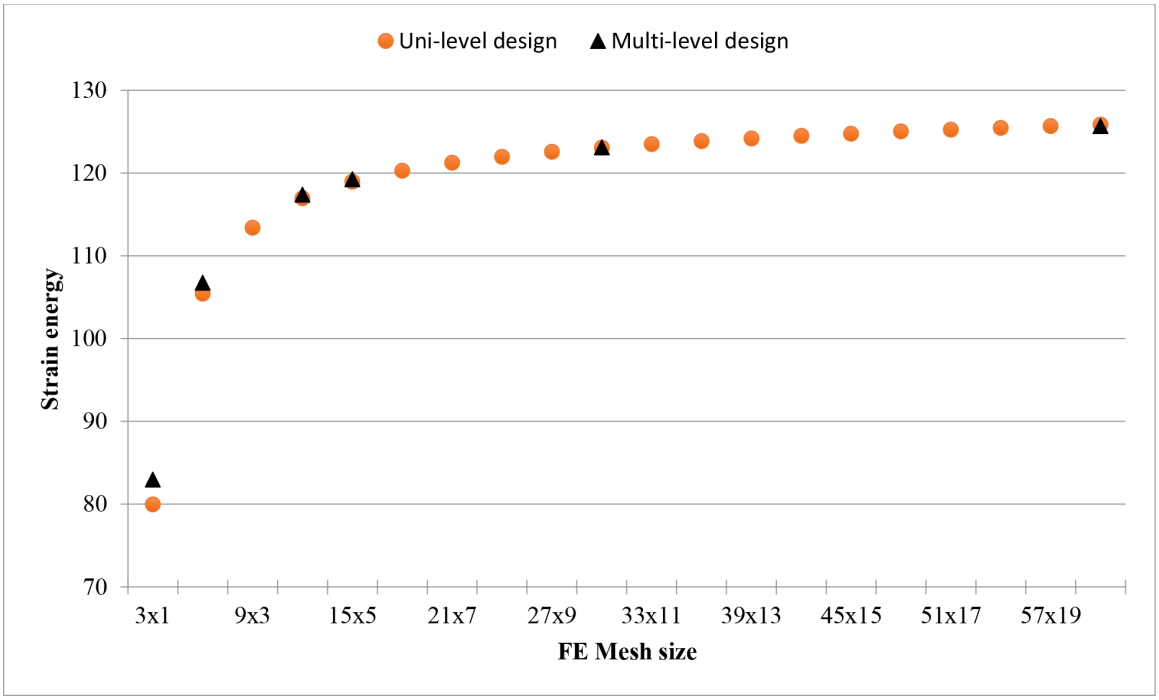

Figure 4.6. Uni-level design objective vs. Multi-level design objective: a solid structure example.

As reference, the Finite Element Analysis (FEA) is done by 99-line code [1] as shown in Tab. 4.3 for homogeneous materials. The FEA results from homogenization are shown in Tab. 4.4, Fig. 4.9 and Fig. 4.10. From Fig. 4.9, the same observation is derived: the smaller the ratio between meso-scale dimension and macro-scale dimension, the smaller the error exists. However, a small error responds to high computational cost as shown in Fig. 4.10.

Table 4.3. FEA results of uni-level design: a MBB-Beam example.

FE Mesh	**Obj.**	**FEA Time (s)**
300×100	196.2777	143.0841

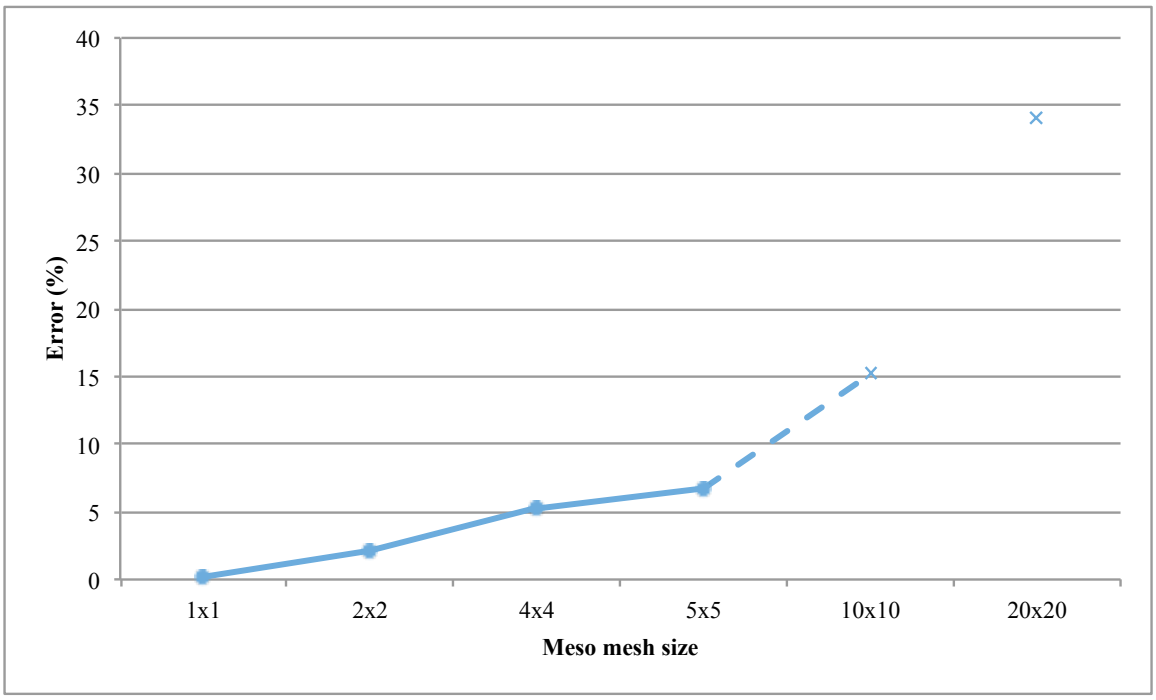

Figure 4.7. Meso mesh size vs. Error: a solid structure example.

Figure 4.8. Uni-level design result for MBB problem, as Fig. 2.8.

4.2.2 Cantilever Beam

The design domain for the cantilever beam example is sketched as shown in Fig. 4.11(a).The domain in Fig. 4.11(a) is fully constrained on the left edge with a downward point load in the center of the domain on the right edge. The optimized beam is shown in Fig. 4.11(b). The macro-scale design domain of Fig. 4.11(b) is then partitioned into different FE mesh sizes of meso-scale as shown in Tab. 4.6.

Table 4.4. FEA results using homogenization: a MBB-Beam example.

Macro	**Meso**	ε	**Obj.**	**FEA Time (s)**	**Error (%)**
300×100	1×1	3.33×10^{-5}	205.85	2881.44	-4.88
150×50	2×2	5.33×10^{-4}	198.33	192.34	-1.05
75×25	4×4	8.53×10^{-3}	192.62	27.05	1.87
60×20	5×5	2.08×10^{-2}	189.28	20.35	3.57
30×10	10×10	3.33×10^{-1}	150.80	15.37	23.17

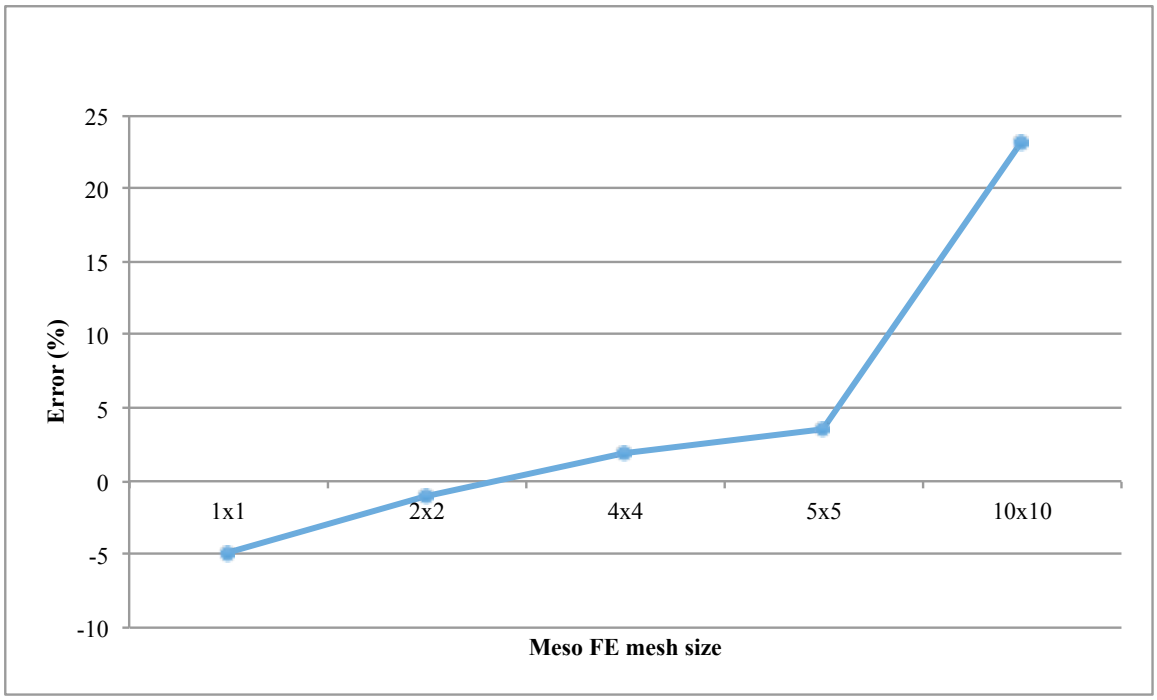

Figure 4.9. Meso mesh size vs. Error: a MBB-Beam example (Homogeneous Materials).

The reference results are shown in Tab. 4.5. Table. 4.6 shows the results through homogenization of the meso-structures. The same conclusions can be derived as the MBB-Beam problem as shown in Fig. 4.12 and Fig. 4.13. However, in this example,

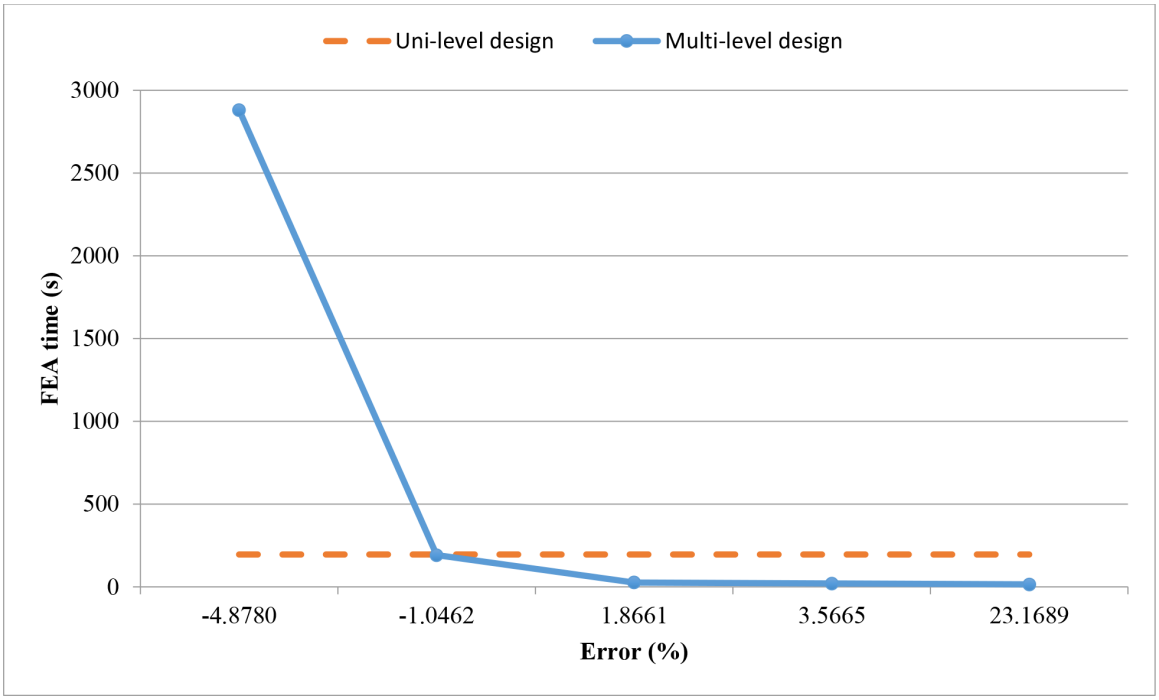

Figure 4.10. Error vs. FEA time: a MBB-Beam example (Homogeneous Materials).

when the meso-macro ratio is 0.25, the error is extremely high. This result indicates that different problems has different desired maximum meso-macro ratios.

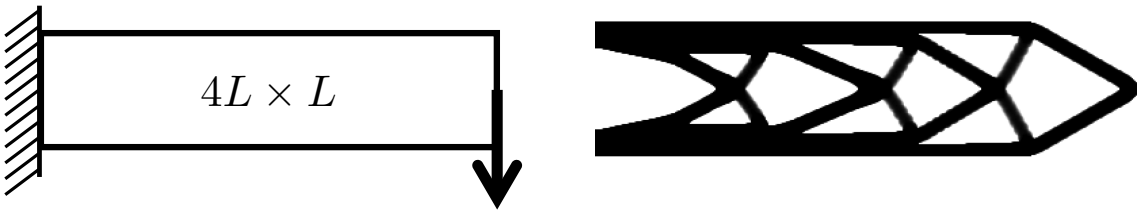

(a) Design domain for cantilever beam. (b) Resulting optimized cantilever beam.

Figure 4.11. A cantilever beam example.

Table 4.5. FEA results of uni-level design: a cantilever beam example.

FE Mesh	**Obj.**	**FEA Time (s)**
400×100	365.2241	263.4223

Table 4.6. FEA results using homogenization: a cantilever beam example.

MACRO	MESO	ε	**Obj.**	**FEA Time**	**Error (%)**
400×100	1×1	2.50×10^{-5}	380.28	2881.44	-4.12
200×50	2×2	4.00×10^{-4}	363.99	192.34	0.34
100×25	4×4	6.40×10^{-3}	348.94	27.05	4.46
80×20	5×5	1.56×10^{-2}	335.64	20.35	8.10
40×10	10×10	2.50×10^{-1}	5265727.23	15.37	1441879.78

4.3 Errors Involved in the Multi-scale Topology Optimization

Actually, it is hard to isolate the errors from mesh refinement and the errors from the homogenization procedure. In this section, we want to quantify the quality of the final topologies, which we achieved through the multi-scale topology optimization methodologies. The error is calculated through the following equation

$$\frac{\mathrm{OBJ}_{\mathrm{multi}} - \mathrm{OBJ}_{\mathrm{uni}}}{\mathrm{OBJ}_{\mathrm{multi}}} \times 100\% \tag{4.1}$$

4.3.1 MBB-Beam

The same problem is solved as before using periodic cellular materials and non-periodic cellular materials. The final topologies are shown in Fig. 4.14 for the periodic cellular materials and Fig. 4.15 for the non-periodic cellular materials. In the case of Fig. 4.14(b), all the macro-scale element densities that equal to 1 (solid) are replaced by the optimized meso-structure. The comparison results are shown in Tab. 4.7. As

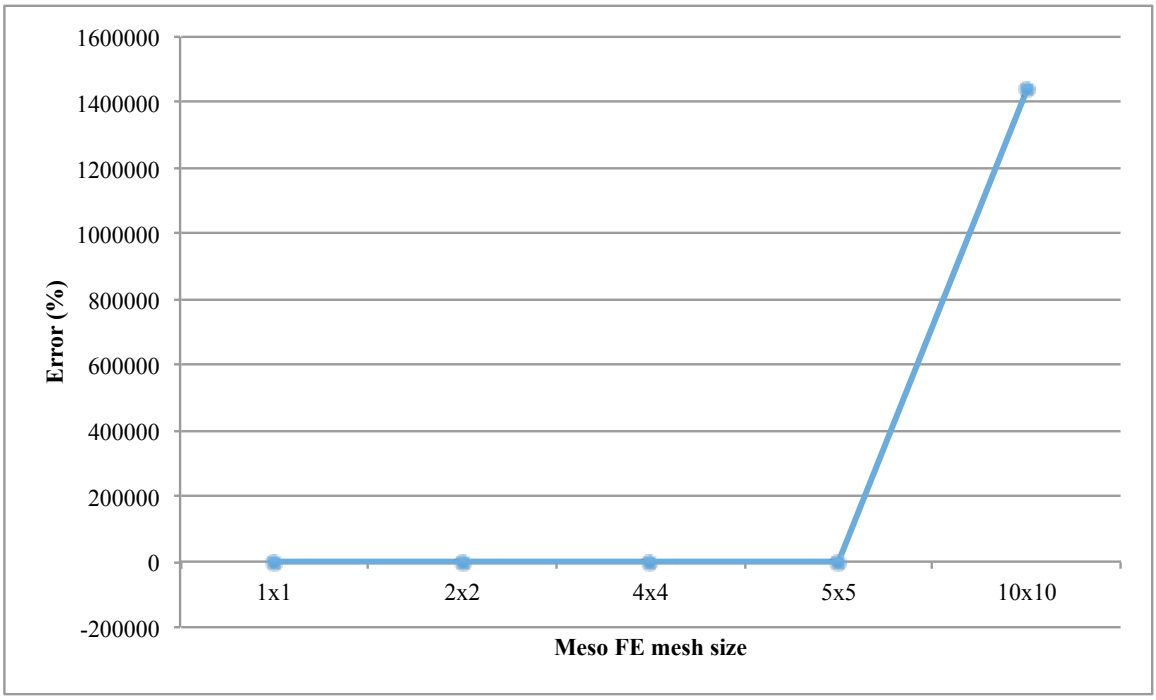

Figure 4.12. Meso mesh size vs. Error: a cantilever beam example (Homogeneous materials).

reference, the solid structure is solved and the results are given in the first row of Tab. 4.7. In the previous discussion (c.f. Tab. 4.4) the homogenization errors for solid structure are very small (normally within 1%); that is, the error mainly exists in the mesh refinement. As we can see in Tab. 4.7 the error in periodic cellular materials significantly shows up while the error in non-periodic cellular materials is reduced. The difference between solid structure and non-periodic cellular materials is within 2%, which in another way indicates that the usage of non-periodic cellular materials possesses more accuracy than periodic cellular materials.

4.3.2 Cantilever Beam

The same test example is used here as in the previous section, the comparisons are summarized in Tab. 4.8 and the final topologies are shown in Figs. 4.16 and 4.17.

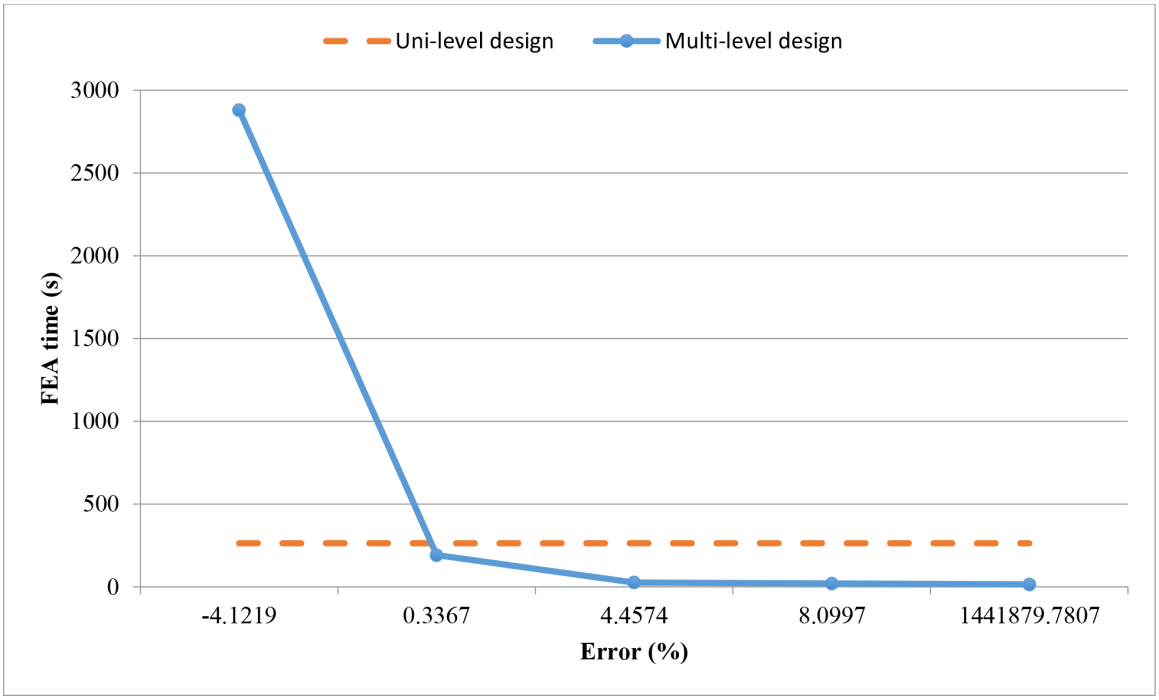

Figure 4.13. Error vs. FEA Time: a cantilever beam example (Homogeneous materials).

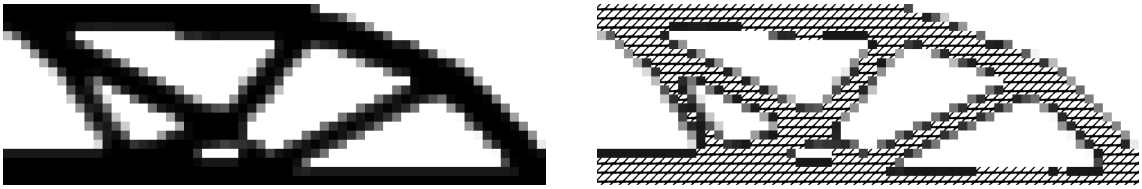

(a) Macro-scale topology for multi-level design.

(b) Macro-scale topology for uni-level design.

Figure 4.14. Final topologies for MBB-Beam with periodic cellular materials.

The error of non-periodic cellular materials has a much greater reduction than those with periodic cellular materials.

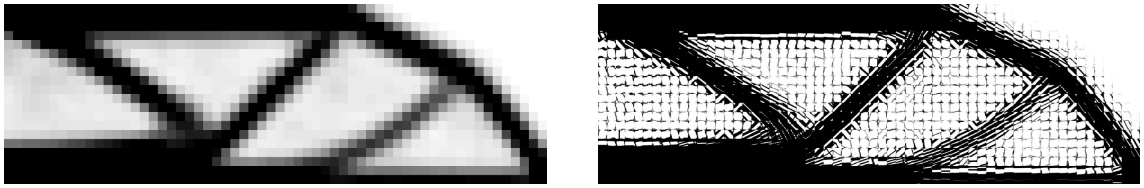

(a) Macro-scale topology for multi-level design. (b) Macro-scale topology for uni-level design.

Figure 4.15. Final topologies for MBB-Beam with non-periodic cellular materials.

Table 4.7. FEA results using homogenization: a MBB-Beam example.

	MACRO		**MESO**		**Obj.**	**Error (%)**
	nelx	**nely**	**nelx**	**nely**		
Solid structure	60×20	20×20	-	-	138.62	-10.02
	60	20	20	20	126.00	
Periodic	60×20	20×20	-	-	955.95	19.59
	60	20	20	20	1188.90	
Non-periodic	60×20	20×20	-	-	233.10	-11.37
	60	20	20	20	209.31	

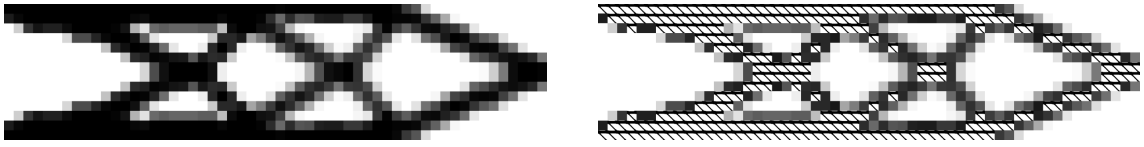

(a) Macro-scale topology for multi-level design. (b) Macro-scale topology for uni-level design.

Figure 4.16. Final topologies for Cantilever beam with periodic cellular materials.

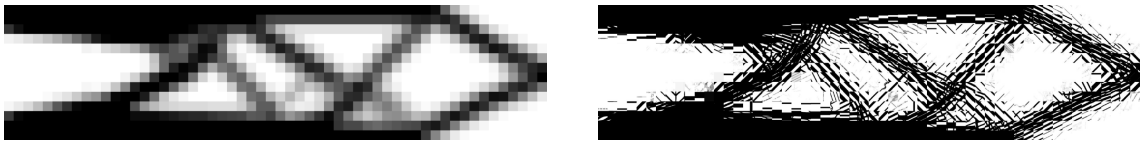

(a) Macro-scale topology for multi-level design. (b) Macro-scale topology for uni-level design.

Figure 4.17. Final topologies for Cantilever beam with non-periodic cellular materials.

Table 4.8. FEA results using homogenization: a cantilever beam example.

	Macro		**Meso**		**Obj.**	**Error (%)**
	nelx	**nely**	**nelx**	**nely**		
Solid structure	60×20	20×20	-	-	120.42	-2.12
	60	20	20	20	117.92	
Periodic	60×20	20×20	-	-	1329.60	-11.83
	60	20	20	20	1188.90	
Non-periodic	60×20	20×20	-	-	436.10	2.35
	60	20	20	20	446.60	

5. SUMMARY AND RECOMMENDATIONS

This present work studies the multi-scale topology optimization methodologies for structures with periodic cellular materials and non-periodic cellular materials. In the design of periodic cellular materials, since the meso-structure is assumed uniform on the macro-scale, it meets todays manufacturing requirements. The formulations of multi-scale topology optimization for stiff structures and compliant mechanism synthesis are discussed and the structural analyses are presented. The optimal structures and materials are derived concurrently without solving sub-problems. Therefore, the efficiency of the optimization procedure is greatly improved. Penalization methods are adopted on both scales: modified Porous Anisotropic Material with Penalization on the macro-scale and modified Solid Isotropic Material with Penalization on the meso-scale to achieve clear black-and-white topologies. Additionally, regularization techniques are deployed in order to avoid numerical instabilities, such as mesh-dependency, checkerboard pattern and local minima. Although applying periodic cellular materials on the meso-scale with low mass fraction drives black-and-white solutions, the structural performances are unsatisfactory.

Non-periodic cellular materials on the meso-scale are then applied due to the unideal accomplishment of periodic meso-structures. In this case, optimized structures and materials are obtained iteratively. The total number of sub-problems is equal to the number of elements used to discretize the macro-scale design domain. Numerical results prove the viability of using non-periodic cellular materials. The optimized topologies are very similar on the macro-scale for both periodic cellular materials and non-periodic cellular materials; however the morphologies of the meso-structure vary even on the same spatial point of the macro-scale. The optimal search effects every element on the macro-scale to achieve the final meso-structures while only one single representative unit cell is optimized on the meso-scale when using pe-

riodic cellular materials; hence, the structural performances of non-periodic cellular materials are better than the usage of periodic cellular materials. When requiring high structural performance, the traditional topology optimization method is more efficient since the results are the same as using non-periodic cellular materials; in addition, it does not need to solve sub-problems. When the designer is pursuing ultra-light weight structure (e.g. 0.25 mass fraction for stiff structure design example, 0.35 mass fraction for compliant synthesis example), the multi-scale topology optimization procedure using non-periodic cellular materials will provide black-and-white topologies and improved structural performance over homogeneous materials. However, we believe that the structural performance of homogenous materials should be very similar when designing ultra-light weight structures if we have: 1) good theory to address problems with low mass fraction using homogeneous materials and/or 2) a very strong computer to work through large-scale topology optimization problems.

Finally, the idea of quantifying the errors involved in the multi-scale topology optimization approach, such as mesh refinement errors, homogenization errors is suggested. Multiple numerical examples are performed in order to learn how mesh size and/or homogenization effects the final design. Errors are calculated via the differences between uni-level design and multi-level design. Uni-level design means that every element on the macro-scale is replaced by its own optimized mesh structure, then the final problem becomes a large-scale Finite Elements Analysis (FEA) problem. On the other hand, multi-level design does not really care about the meso-structures, the meso-structure material properties are represented by the effective stiffness tensor which is implemented in the macro-scale structural analysis. From numerical experiments, when the meso-scale dimension to macro-scale dimension ratio within a reasonable range (depends on specific problem), the errors from the homogenization procedure are very small (normally within 1%), which means the errors between uni-level design and multi-level design are mainly caused by mesh refinement.

The superiorities of using cellular materials with high mass fraction are limited under deterministic design if only the structural performances are considered. Even

so, structures with cellular materials are always considered as multi-functional objectives. We believe that the cellular materials will perform better than the homogenous materials under uncertainty, which could be the next step of this work. In additional, manufacturing constraints could be adopted on both scales to ensure the manufacturability of resulting structures and materials. Furthermore, the computational cost of non-periodic cellular materials optimization is extremely high since the total number of sub-problems need to be solved is same as the number of finite elements used to discretize the macro-scale design domain. Parallel computing will be a perfect solution for these type of problems since every sub-problem is independent of each other. A simple local computer has a limitation of 12 cores to run the program simultaneously while a single GPU card typically has hundreds of processors, which makes GPU very suitable to highly parallel problems and everyone has access to a personal supercomputer. Thus, GPU computing on this multi-scale topology optimization method using non-periodic cellular materials is worth developing. The 3D topology optimization for non-periodic cellular materials has already been implemented while the usage of periodic cellular materials in 3D, which can obtain optimized structures and materials synchronously, has not yet been developed. 3D application will be another interesting continuation of this investigation.

LIST OF REFERENCES

LIST OF REFERENCES

[1] M. P. Bendsøe and O. Sigmund. *Topology optimization: theory, method and applications*. Springer, 2003.

[2] M. P. Bendsøe and N. Kikuchi. Generating optimal topologies in structural design using a homogenization method. *Computer Methods in Applied Mechanics and Engineering*, 71(2):197–224, 1988.

[3] S. Nishiwaki, M. I. Frecker, S. Min, and N. Kikuchi. Topology optimization of compliant mechanisms using the homogenization method. *International Journal for Numerical Methods in Engineering*, 42:535–559, 1998.

[4] K. Svanberg. The method of moving asymptotes-a new method for structural optimzation. *International Journal for Numerical Methods in Engineering*, 24:359–373, 1987.

[5] M. Bruyneel, P. Duysinx, and C. Fleury. A family of mma approximations for structural optimization. *Structural and Multidisciplinary Optimization*, 24:263–276, 2002.

[6] V. B. Venkayya. Optimality criteria: a basis for multidisciplinary design optimization. *Computational Mechanics*, 5(1):1–21, 1989.

[7] Y. Xie and G. P. Steven. *Evolutionary structural optimization*. Springer, 1997.

[8] S. Patil, S. Zhou, and Q. Li. Design of periodic microstructural materials by using evolutionary structural optimization method. *Advanced Materials Research*, 32:279–283, 2008.

[9] M. Y. Wang, X. Wang, and D. Guo. A level set method for structural topology optimization. *Computer Methods in Applied Mechanics and Engineering*, 192(1-2):227–246, 2003.

[10] G. Allaire, F. Jouve, and A.-M. Toader. Structural optimization using sensitivity analysis and a level-set method. *Journal of Computational Physics*, 194(1):363–393, 2004.

[11] A. Tovar, N. M. Patel, G. L. Niebur, M. Sen, and J. E. Renaud. Topology optimization using a hybrid cellular automation method with local control rules. *Journal of Mechanical Design, Transactions of the ASME*, 128(6):1205–1216, 2006.

[12] A. Tovar, N. M. Patel, A. K. Kaushik, and J. E. Renaud. Optimality conditions of the hybrid cellular automata for structural optimization. *AIAA Journal*, 45(3):673–683, 2007.

[13] M. P. Bendsøe. Optimal shape design as a material distribution problem. *Structural and Multidisciplinary Optimization*, 1(4):193–202, 1989.

[14] J. M. Guedes and N. Kikuchi. Preprocessing and postprocessing for materials based on the homogenization method with adaptive finite element methods. *Computer Methods in Applied Mechanics and Engineering*, 83(2):143–198, 1990.

[15] O. Sigmund. Materials with prescribed constitutive parameters-an iverse homogenization problem. *International Journal of Solids and Structures*, 31(17):2313–2329, 1994.

[16] D. Fujii, B. C. Chen, and N. Kikuchi. Composite material design of two-dimensional structures using the homgenization design method. *International Journal for Numerical Methods in Engineering*, 50:2031–2051, 2001.

[17] X. Huang, S. Zhou, Y. Xie, and Q. Li. Topology optimization of microstructures of cellular materials and composites for macrostructures. *Computational Materials Science*, 67:397–407, 2013.

[18] O. Sigmund and S. Torquato. Composites with extremal thermal expansion coefficients. *Applied Physics Letters*, 69(21):3203–3203, 1996.

[19] O. Sigmund and S. Torquato. Design of materials with extreme thermal expansion using a three-phase topology optimization method. *Proceedings of SPIE - The International Society for Optical Engineering*, 3040:52–60, 1997.

[20] G. P. Steven, Q. Li, and Y. M. Xie. Evolutionary topology and shape design for general physical field problems. *Computational Mechanics*, 26(2):129–139, 2000.

[21] Y. Chen, S. Zhou, and Q. Li. Multiobjective topology optimization for finite periodic structures. *Computers and Structures*, 88(11-12):806–811, 2010.

[22] O. Sigmund. Tailoring materials for specific needs. *Journal of Intelligent Material Systems and Structures*, 5(6):736–742, 1994.

[23] O. Sigmund. Tailoring materials with prescribed elastic properties. *Mechanics of Materials*, 20(4):351–368, 1995.

[24] G. H. Paulino, E. C. N. Silva, and C. H. Le. Optimal design of periodic functionally graded composites with prescribed properties. *Structural and Multidisciplinary Optimization*, 38(5):469–489, 2009.

[25] S. R. M. Almeida, G. H. Paulino, and E. C. N. Silva. Layout and material gradation in topology optimization of functionally graded structures: A global-local approach. *Structural and Multidisciplinary Optimization*, 42(6):855–868, 2010.

[26] M. P. Bendsøe, L. Erik, and O. Niels. Topology optimization-broadening the areas of application. *Control and Cybernetics*, 34:7–35, 2005.

[27] J. E. Cadman, S. Zhou, Y. Chen, and Q. Li. On design of multi-functional microstructural materials. *Journal of Materials Science*, 48(1):51–66, 2013.

[28] P. G. Coelho, P. R. Fernandes, J. M. Guedes, and H. C. Rodrigues. A hierarchical model for concurrent material and topology optimisation of three-dimensional structures. *Structural and Multidisciplinary Optimization*, 35(2):107–115, 2008.

[29] C. Seepersad. *A Robust Topological Preliminary Design Exploration Method With Materials Design Applications*. PhD thesis, Georgia Institute of Technology, 2004.

[30] H. Wang. *A unit cell approach for lightweight structure and compliant mechanism*. PhD thesis, Georgia Institute of Technology, 2005.

[31] M. Stolpe and T. Stidsen. A hierarchical method for discrete structural topology design problems with local stress and displacement constraints. *International Journal for Numerical Methods in Engineering*, 69(5):1060–1084, 2007.

[32] F. Schury, M. Stingl, and F. Wein. Efficient two-scale optimization of manufacturable graded structures. *SIAM Journal on Scientific Computing*, 34(6):B711–B733, 2012.

[33] C.S. Andreasen and O. Sigmund. Multiscale modeling and topology optimization of poroelastic actuators. *Smart Materials and Structures*, 21, 2012.

[34] S. Xu and G. Cheng. Optimum material design of minimum structural compliance under seepage constraint. *Structural and Multidisciplinary Optimization*, 41(4):575–587, 2010.

[35] H. C. Rodrigues, J. M. Guedes, and M. P. Bendsøe. Hierarchical optimization of material and structure. *Structural and Multidisciplinary Optimization*, 24(1):1–10, 2002.

[36] J. Zowe, M. Kočvara, and M. P. Bendsøe. Free material optimization via mathematical programming. *Mathematical Programming*, 79(1-3):445–466, 1997.

[37] P. S. Theocaris and G. E. Stavroulakis. Optimal material design in composites: An iterative approach based on homogenized cells. *Computer Methods in Applied Mechanics and Engineering*, 169(1-2):31–42, 1999.

[38] P. G. Coelho, P. R. Fernandes, H. C. Rodrigues, J. B. Cardoso, and J. M. Guedes. Numerical modeling of bone tissue adaptation-a hierarchical approach for bone apparent density and trabecular structure. *Journal of Biomechanics*, 42(7):830–837, 2009.

[39] C. H. Le, T. E. Bruns, and D. A. Tortorelli. Material microstructure optimization for linear elastodynamic energy wave management. *Journal of the Mechanics and Physics of Solids*, 60(2):351–378, 2012.

[40] Y. Liu, Y. Yin, and Z. Guo. Static and dynamic design based on hierarchical optimization for materials and structure of porous metals. *Science China Technological Sciences*, 55(10):2808–2814, 2012.

[41] L. Liu, J. Yan, and G. Cheng. Optimum structure with homogeneous optimum truss-like material. *Computers and Structures*, 86(13-14):1417–1425, 2008.

[42] B. Niu, J. Yan, and G. Cheng. Optimum structure with homogeneous optimum cellular material for maximum fundamental frequency. *Structural and Multidisciplinary Optimization*, 39:115–132, 2009.

[43] J. Deng, J. Yan, and G. Cheng. Multi-objective concurrent topology optimization of thermoelastic structures composed of homogeneous porous material. *Structural and Multidisciplinary Optimization*, 47(4):583–597, 2013.

[44] O. Sigmund. A 99 line topology optimization code written in matlab. *Structural and Multidisciplinary Optimization*, 21(2):120–127, 2001.

[45] M. R. Hestenes and E. Stiefel. Methods of conjugate gradients for solving linear systems. *Journal of Research of the National Bureau of Standards*, 49(6), 1952.

[46] O. Sigmund. Morphology-based black and white filters for topology optimization. *Structural and Multidisciplinary Optimization*, 33:401–424, 2007.

[47] M. P. Bendsøe and O. Sigmund. Material interpolations in topology optimization. *Archive of Applied Mechanics*, 69:635–654, 1999.

[48] R. D. Cook, D. S. Malkus, and M. E. Plesha. *Concepts and application of finite element analysis*. Wiley, 1989.

[49] P. W. Christensen and A. Klarbring. *An introduction to structural optimization*. Springer, 2009.

[50] T. E. Bruns and D. A. Tortorelli. Topology optimization of non-linear elastic structures and compliant mechanisms. *Computer Methods in Applied Mechanics and Engineering*, 190(26-27):3443–3459, 2001.

[51] B. Bourdin. Filters in topology optimization. *International Journal for Numerical Methods in Engineering*, 50(9):2143–2158, 2001.

[52] J. K. Guest, J. H. Prevost, and T. Belytschko. Achieving minimum length scale in topology optimization using nodal design variables and projection functions. *International Journal for Numerical Methods in Engineering*, 61:238–254, 2004.

[53] J. K. Guest, A. Asadpoure, and S.-H. Ha. Elimiating beta-continuation from heaviside projection and density filter algorithms. *Structural and Multidisciplinary Optimization*, 44:443–453, 2011.

[54] S. Xu, Y. Cai, and G. Cheng. Volume preservig nonlinear density filter based on heaviside functions. *Structural and Multidisciplinary Optimization*, 41:495–505, 2010.

[55] A. A. Groenwold and L. F. P. Etman. A quadratic approximation for structural topology optimization. *International Journal for Numerical Methods in Engineering*, 82(4):505–524, 2010.

APPENDICES

A. EXPANDING THE MESOSCOPIC EQUILIBRIUM EQUATIONS

A.1 Three Cases for Solving the Mesoscopic Equilibrium Equations

Applying different values of k and l, there would be three different cases (**a:** $k = l = 1$, **b:** $k = l = 2$ and **c:** $k = 1, l = 2$) for Eqs. 2.19 and 2.20.

case a: $k = 1, l = 1$

For simplicity, by using the compact notation $1 \leftarrow 11, 2 \leftarrow 22, 6 \leftarrow 12$ and $\Phi_1 \leftarrow \chi_1^{11}, \Phi_2 \leftarrow \chi_2^{11}$

Expanding Eq. 2.20 and applying the symmetric properties of the material and removing the zero coefficients, we get

$$\begin{aligned}\int_Y \Bigg[\left(C_{11}\frac{\partial\Phi_1}{\partial y_1} + C_{12}\frac{\partial\Phi_2}{\partial y_2}\right)\frac{\partial v_1}{\partial y_1} + C_{66}\left(\frac{\partial\Phi_1}{\partial y_2} + \frac{\partial\Phi_2}{\partial y_1}\right)\left(\frac{\partial v_1}{\partial y_2} + \frac{\partial v_2}{\partial y_1}\right) + \\ \left(C_{12}\frac{\partial\Phi_1}{\partial y_1} + C_{22}\frac{\partial\Phi_2}{\partial y_2}\right)\frac{\partial v_2}{\partial y_2}\Bigg] dY = \int_Y \left(C_{11}\frac{\partial v_1}{\partial y_1} + C_{12}\frac{\partial v_2}{\partial y_2}\right) dY,\end{aligned} \tag{A.1}$$

and considering the case $i = 1, j = 1$ in Eq. 2.19

$$C_{11}^{\mathrm{H}} = \frac{1}{Y_0}\int_Y \left(C_{11} - C_{11}\frac{\partial\Phi_1}{\partial y_1} - C_{12}\frac{\partial\Phi_2}{\partial y_2}\right) dY, \tag{A.2}$$

and the case $i = 2, j = 2$

$$C_{21}^{\mathrm{H}} = \frac{1}{Y_0}\int_Y \left(C_{21} - C_{21}\frac{\partial\Phi_1}{\partial y_1} - C_{22}\frac{\partial\Phi_2}{\partial y_2}\right) dY. \tag{A.3}$$

case b: $k = 2, l = 2$

Similarly, in this case from Eq. 2.20, by assuming $\Psi_1 \leftarrow \chi_1^{22}, \Psi_2 \leftarrow \chi_2^{22}$ we get

$$\begin{aligned}\int_Y \Bigg[\left(C_{11}\frac{\partial\Psi_1}{\partial y_1} + C_{12}\frac{\partial\Psi_2}{\partial y_2}\right)\frac{\partial v_1}{\partial y_1} + C_{66}\left(\frac{\partial\Psi_1}{\partial y_2} + \frac{\partial\Psi_2}{\partial y_1}\right)\left(\frac{\partial v_1}{\partial y_2} + \frac{\partial v_2}{\partial y_1}\right) + \\ \left(C_{21}\frac{\partial\Psi_1}{\partial y_1} + C_{22}\frac{\partial\Psi_2}{\partial y_2}\right)\frac{\partial v_2}{\partial y_2}\Bigg] dY = \int_Y \left(C_{12}\frac{\partial v_1}{\partial y_1} + C_{22}\frac{\partial v_2}{\partial y_2}\right) dY,\end{aligned} \tag{A.4}$$

and for Eq. 2.19 with $i = 1, j = 1$

$$C_{12}^{\mathrm{H}} = \frac{1}{Y_0}\int_Y \left(C_{12} - C_{11}\frac{\partial \Psi_1}{\partial y_1} - C_{12}\frac{\partial \Psi_2}{\partial y_2} \right) dY, \tag{A.5}$$

and the case $i = 2, j = 2$

$$C_{22}^{\mathrm{H}} = \frac{1}{Y_0}\int_Y \left(C_{22} - C_{21}\frac{\partial \Psi_1}{\partial y_1} - C_{22}\frac{\partial \Psi_2}{\partial y_2} \right) dY. \tag{A.6}$$

case c: $k = 1, l = 2$

Following the same procedure and assuming $\Theta_1 \leftarrow \chi_1^{12}, \Theta_2 \leftarrow \chi_2^{12}$, Eq. 2.20 results in

$$\begin{aligned} \int_Y \Bigg[\left(C_{11}\frac{\partial \Theta_1}{\partial y_1} + C_{12}\frac{\partial \Theta_2}{\partial y_2} \right)\frac{\partial v_1}{\partial y_1} + C_{66}\left(\frac{\partial \Theta_1}{\partial y_2} + \frac{\partial \Theta_2}{\partial y_1} \right)\left(\frac{\partial v_1}{\partial y_2} + \frac{\partial v_2}{\partial y_1} \right) + \\ \left(C_{12}\frac{\partial \Theta_1}{\partial y_1} + C_{22}\frac{\partial \Theta_2}{\partial y_2} \right)\frac{\partial v_2}{\partial y_2} \Bigg] dY = \int_Y \left(C_{66}\frac{\partial v_1}{\partial y_1} + C_{22}\frac{\partial v_2}{\partial y_2} \right) dY, \end{aligned} \tag{A.7}$$

and for $i = 1, j = 2$, Eq. 2.19 becomes

$$C_{66}^{\mathrm{H}} = \frac{1}{Y_0}\int_Y C_{66}\left(1 - \frac{\partial \Theta_1}{\partial y_2} - \frac{\partial \Theta_2}{\partial y_1} \right) dY. \tag{A.8}$$

A.2 Matrix Notation

Now, let us define

$$\boldsymbol{\epsilon}(\cdot) = \begin{Bmatrix} \frac{\partial (\cdot)_1}{\partial y_1} \\ \frac{\partial (\cdot)_2}{\partial y_2} \\ \frac{\partial (\cdot)_1}{\partial y_2} + \frac{\partial (\cdot)_2}{\partial y_1} \end{Bmatrix}, \tag{A.9}$$

and

$$\mathbf{C} = \begin{bmatrix} \mathbf{c}_1 & \mathbf{c}_2 & \mathbf{c}_3 \end{bmatrix}, \tag{A.10}$$

Here $\mathbf{c}_1$, $\mathbf{c}_2$ and $\mathbf{c}_3$ are the columns of the constitutive matrix $\mathbf{C}$

$$\mathbf{c}_1 = \begin{Bmatrix} C_{11} \\ C_{12} \\ 0 \end{Bmatrix}, \qquad \mathbf{c}_2 = \begin{Bmatrix} C_{21} \\ C_{22} \\ 0 \end{Bmatrix}, \text{ and} \qquad \mathbf{c}_3 = \begin{Bmatrix} 0 \\ 0 \\ C_{66} \end{Bmatrix}. \tag{A.11}$$

If we rearrange Eq. A.1, it will becomes

$$\begin{aligned}\int_Y \begin{bmatrix} \frac{\partial v_1}{\partial y_1} & \frac{\partial v_2}{\partial y_2} & \frac{\partial v_1}{\partial y_2} + \frac{\partial v_2}{\partial y_1} \end{bmatrix} \begin{bmatrix} C_{11} & C_{12} & 0 \\ C_{12} & C_{22} & 0 \\ 0 & 0 & C_{66} \end{bmatrix} \begin{Bmatrix} \frac{\partial \Phi_1}{\partial y_1} \\ \frac{\partial \Phi_2}{\partial y_2} \\ \frac{\partial \Phi_1}{\partial y_2} + \frac{\partial \Phi_2}{\partial y_1} \end{Bmatrix} dY \\ = \int_Y \begin{bmatrix} \frac{\partial v_1}{\partial y_1} & \frac{\partial v_2}{\partial y_2} & \frac{\partial v_1}{\partial y_2} + \frac{\partial v_2}{\partial y_1} \end{bmatrix} \begin{Bmatrix} C_{11} \\ C_{12} \\ 0 \end{Bmatrix} dY.\end{aligned} \tag{A.12}$$

By using the definition above, we have

$$\int_Y \boldsymbol{\epsilon}^{\mathrm{T}}(\mathbf{v})\ \mathbf{C}\ \boldsymbol{\epsilon}(\boldsymbol{\Phi}) dY = \int_Y \boldsymbol{\epsilon}^{\mathrm{T}}(\mathbf{v})\ \mathbf{c}_1\ dY, \text{ for all Y-periodic } \mathbf{v}, \tag{A.13}$$

and similarly for Eq. A.2 and Eq. A.3

$$C_{11}^{\mathrm{H}} = \frac{1}{Y_0} \int_Y \Big[C_{11} - \mathbf{c}_1^{\mathrm{T}} \boldsymbol{\epsilon}(\boldsymbol{\Phi}) \Big] dY, \tag{A.14}$$

$$C_{21}^{\mathrm{H}} = \frac{1}{Y_0} \int_Y \Big[C_{21} - \mathbf{c}_2^{\mathrm{T}} \boldsymbol{\epsilon}(\boldsymbol{\Phi}) \Big] dY. \tag{A.15}$$

If we apply the same procedure to **case b** and **case c**, Eqs. A.4 - A.8 yield to

$$\int_Y \boldsymbol{\epsilon}^{\mathrm{T}}(\mathbf{v})\ \mathbf{C}\ \boldsymbol{\epsilon}(\boldsymbol{\Psi}) dY = \int_Y \boldsymbol{\epsilon}^{\mathrm{T}}(\mathbf{v})\ \mathbf{c}_2\ dY, \text{ for all Y-periodic } \mathbf{v}, \tag{A.16}$$

$$C_{12}^{\mathrm{H}} = \frac{1}{Y_0} \int_Y \Big[C_{12} - \mathbf{c}_1^{\mathrm{T}} \boldsymbol{\epsilon}(\boldsymbol{\Psi}) \Big] dY, \tag{A.17}$$

$$C_{22}^{\mathrm{H}} = \frac{1}{Y_0} \int_Y \Big[C_{22} - \mathbf{c}_2^{\mathrm{T}} \boldsymbol{\epsilon}(\boldsymbol{\Psi}) \Big] dY, \tag{A.18}$$

and

$$\int_Y \boldsymbol{\epsilon}^{\mathrm{T}}(\mathbf{v})\ \mathbf{C}\ \boldsymbol{\epsilon}(\boldsymbol{\Theta}) dY = \int_Y \boldsymbol{\epsilon}^{\mathrm{T}}(\mathbf{v})\ \mathbf{c}_3\ dY, \text{ for all Y-periodic } \mathbf{v}, \tag{A.19}$$

$$C_{66}^{\mathrm{H}} = \frac{1}{Y_0} \int_Y \Big[C_{66} - \mathbf{c}_3^{\mathrm{T}} \boldsymbol{\epsilon}(\boldsymbol{\Theta}) \Big] dY. \tag{A.20}$$

B. PERIODIC BOUNDARY CONDITIONS

The Periodic Boundary Conditions (PBCs) for unit cell is shown in Fig. 2.4. The computational efficiency can be improved by taking advantage of symmetry boundary conditions. An isotropic unit cell means having identical values of a property in all directions; i.e. isotropic unit cell is symmetric to all axes. On the other hand, the material properties of an orthotropic unit cell are different along each axis; in other words, orthotropic unit cell has symmetry relative to only one axis or both axes. For 2D plane-stress, Figs. B.1(a) and B.1(b) indicate the boundary conditions for isotropic unit cell or orthotropic unit cell is considered.

To impose the proper boundary constraints on unit cell, one can utilize the methods applied to the repeatable structures. For example, simply assigning equal node numbers to opposing boundary nodes. Alternatively, the penalty method or Lagrange multiplier method can be applied [48]. The Lagrange multiplier is implemented in this investigation. For completeness, the concept of Lagrange multiplier which is copied from [48] is presented in this appendix.

B.1 Constraints

A constraints either prescribes the value of a Degree of Freedoms (d.o.f.) (as in imposing a support condition) or prescribes a relationship among d.o.f. In common terminology, a single-point constraint sets a single d.o.f. to a known value (often zero), and a multipoint constraint imposes a relationship between two or more d.o.f.

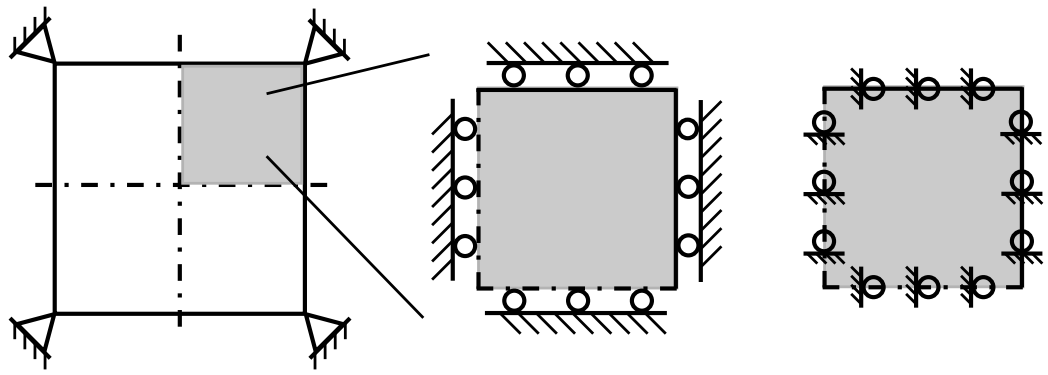

(a) Illustration of 1/4 symmetry boundary conditions for unit cell.

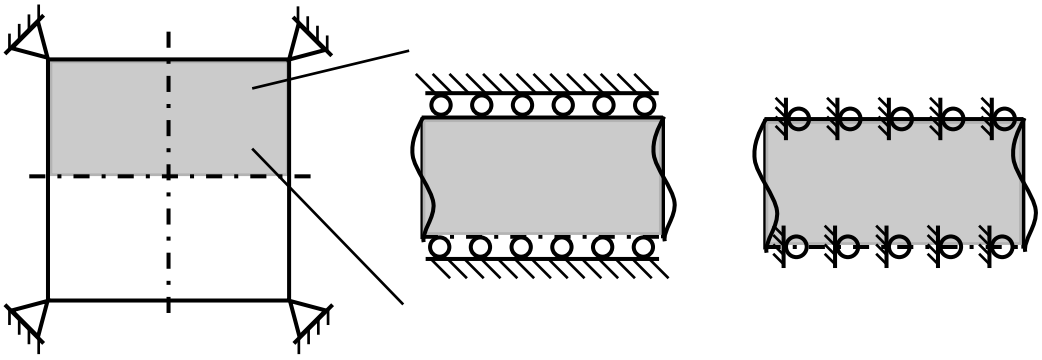

(b) Illustration of 1/2 symmetry boundary conditions for unit cell.

Figure B.1. Illustration of periodic boundary conditions for unit cell.

B.2 Transformation Equations

Constraint equations that couple d.o.f. in $\mathbf{D}$ can be written in the form

$$\mathbf{C}_\lambda \mathbf{D} = \mathbf{Q}, \tag{B.1}$$

where $\mathbf{C}_\lambda$ and $\mathbf{Q}$ contain constants. There are more d.o.f. in $\mathbf{D}$ than constraint equations, so $\mathbf{C}_\lambda$ has more columns than rows.

B.3 Concept of the Lagrange Multipliers

Lagrange method of undetermined multipliers is used to find the maximum or minimum of a function whose variables are not independent but have some prescribed

relation. In structural mechanics the function is potential energy Π_p and the variables are Degree of Freedoms (d.o.f.) in $\mathbf{D}$, system unknowns become $\mathbf{D}$ and the Lagrange multipliers.

The theory is easy to describe. We write the constraint equation as the homogeneous equation $\mathbf{C}_\lambda\mathbf{D}-\mathbf{Q}=\mathbf{0}$ and multiply its left-hand side by a row vector $\boldsymbol{\lambda}^{\mathrm{T}}$ that contains as many Lagrange multipliers λ_i as there are constraint equations. Next we add the result to the potential expression,

$$\Pi_p = \frac{1}{2}\mathbf{D}^{\mathrm{T}}\mathbf{K}\mathbf{D} - \mathbf{D}^{\mathrm{T}}\mathbf{F} + \boldsymbol{\lambda}^{\mathrm{T}}(\mathbf{C}_\lambda\mathbf{D}-\mathbf{Q}). \tag{B.2}$$

The expression in parentheses is zero, so we have adding nothing to Π_p. Next we make Π_p stationary by writing the equations $\partial\Pi_p/\partial\mathbf{D}=\mathbf{0}$ and $\partial\Pi_p/\partial\boldsymbol{\lambda}=\mathbf{0}$, following differentiation rules. The result is

$$\begin{bmatrix} \mathbf{K} & {\mathbf{C}_\lambda}^T \\ \mathbf{C}_\lambda & \mathbf{0} \end{bmatrix} \begin{Bmatrix} \mathbf{D} \\ \boldsymbol{\lambda} \end{Bmatrix} = \begin{Bmatrix} \mathbf{R} \\ \mathbf{Q} \end{Bmatrix}. \tag{B.3}$$

The lower partition of Eq. B.3 is Eq. B.1, the equation of constraint. Eq. B.3 are solved for both $\mathbf{D}$ and $\boldsymbol{\lambda}$. The λ_i may be interpreted as forces of constraint (see the following example problem).

B.4 Numerical Example

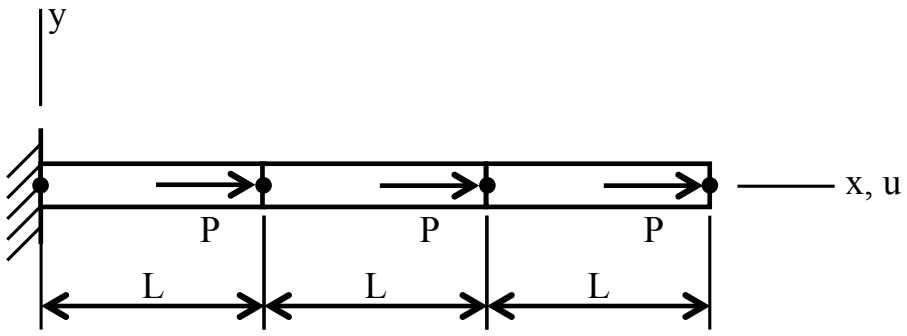

Figure B.2. Three identical bar elements, each of axial stiffness $k = AE/L$.

Consider the three-element structure of Fig. B.2. With only axial deformation allowed, and after the support condition $u = 0$ is imposed at $x = 0$, the structural equations are

$$\begin{bmatrix} 2k & -k & 0 \\ -k & 2k & -k \\ 0 & -k & k \end{bmatrix} \begin{Bmatrix} u_1 \\ u_2 \\ u_3 \end{Bmatrix} = \begin{Bmatrix} P \\ P \\ P \end{Bmatrix}. \tag{B.4}$$

If no constraint applied, the displacements for three nodes are

$$\begin{Bmatrix} u_1 \\ u_2 \\ u_3 \end{Bmatrix} = \begin{Bmatrix} 3P/k \\ 5P/k \\ 6P/k \end{Bmatrix}. \tag{B.5}$$

Imagine that the constraint $u_1 = u_2$ is to be imposed. The constraint matrix $\mathbf{C}_\lambda$ is

$$\mathbf{C}_\lambda = \begin{bmatrix} 1 & -1 & 0 \end{bmatrix}. \tag{B.6}$$

Then Eq. B.3 becomes

$$\begin{bmatrix} 2k & -k & 0 & 1 \\ -k & 2k & -k & -1 \\ 0 & -k & k & 0 \\ 1 & -1 & 0 & 0 \end{bmatrix} \begin{Bmatrix} u_1 \\ u_2 \\ u_3 \\ \lambda \end{Bmatrix} = \begin{Bmatrix} P \\ P \\ P \\ 0 \end{Bmatrix}. \tag{B.7}$$

The solution of Eq. B.7 is

$$\begin{Bmatrix} u_1 \\ u_2 \\ u_3 \\ \lambda \end{Bmatrix} = \begin{Bmatrix} 3P/k \\ 3P/k \\ 4P/k \\ -2P \end{Bmatrix}. \tag{B.8}$$

The result $\lambda = -2P$ can be regarded as the force of constraint applied through the now rigid link 1-2. The algebraic sign of λ is not significant: had we written $\mathbf{C}_\lambda = [-1 \quad 1 \quad 0]$ in Eq. B.6, we would obtain $\lambda = +2P$ but the same values of u_1, u_2, u_3.

C. GAUSSIAN-QUADRATURE NUMERICAL INTEGRATION

C.1 Basic Concept

The integrals in this investigation are computed numerically through Gauss-quadrature numerical integration. A n-point Gaussian-quadrature rule, named after Carl Friedrich Gauss, is a quadrature rule constructed to yield an exact result for polynomials of degree $2n-1$ or less by a suitable choice of the sampling points ζ_s and weights ω_s for $s = 1, \ldots, m$, as shown in Tab. C.1. The domain of integration for such a rule is conventionally taken as $[-1, 1]$, so the rule is stated as

$$\int_{-1}^{1} f(\zeta) d\zeta \approx \sum_{s=1}^{m} \omega_s f(\zeta_s). \tag{C.1}$$

For an integral over $[a, b]$ must be changed into integral over $[-1, 1]$ before applying the Gauss-quadrature rule. This change of interval can be done in the following way

$$\int_{a}^{b} f(\zeta) d\zeta = \frac{b-a}{2} \int_{-1}^{1} f\Big(\frac{b-a}{2} z + \frac{a+b}{2}\Big) dz. \tag{C.2}$$

After applying the Gaussian-Quadrature rule, the following approximation is

$$\int_{a}^{b} f(\zeta) d\zeta \approx \frac{b-a}{2} \sum_{s=1}^{m} \omega_s f\Big(\frac{b-a}{2} z_s + \frac{a+b}{2}\Big). \tag{C.3}$$

C.2 Examples

E.g.1 Approximate $\int_{-1}^{1} x^3 + 2x \; dx$ using Gauss-quadrature integration.

Solution: First, rewriting the function using Eq. C.1 and applying 2×2 Gauss-quadrature sampling points.

$$\int_{-1}^{1} x^3 + 2x \; dx \approx 1 \times \left[\left(-\frac{\sqrt{3}}{3} \right)^3 + 2 \times \left(-\frac{\sqrt{3}}{3} \right) \right] + 1 \times \left[\left(\frac{\sqrt{3}}{3} \right)^3 + 2 \times \left(\frac{\sqrt{3}}{3} \right) \right] = 0. \tag{C.4}$$

Table C.1. Sampling points ζ_s and weighting factors ω_s used in Gauss-quadrature

Number of points m	**Points location** ζ_s	**Weights** ω_s
1	0	2
2	$\pm\sqrt{3}/3$	1
3	0 $\pm\sqrt{3/5}$	8/9 5/9
4	$\pm\sqrt{\left(3-2\sqrt{6/5}\right)/7}$ $\pm\sqrt{\left(3+2\sqrt{6/5}\right)/7}$	$\frac{18+\sqrt{30}}{36}$ $\frac{18-\sqrt{30}}{36}$
5	0 $\pm\frac{1}{3}\sqrt{5-2\sqrt{10/7}}$ $\pm\frac{1}{3}\sqrt{5+2\sqrt{10/7}}$	128/225 $\frac{322+13\sqrt{70}}{900}$ $\frac{322-13\sqrt{70}}{900}$

Analytical solution is

$$\int_{-1}^{1} x^3 + 2x \; dx = \frac{1}{4}x^4 \Big|_{-1}^{1} + x^2 \Big|_{-1}^{1} = 0. \tag{C.5}$$

E.g.2 Approximate $\int_1^{1.5} x^2 \ln 2x \; dx$ using Gauss-quadrature integration.

Solution: First, we need change the interval from over $[1, 1.5]$ to over $[-1, 1]$ using Eq. C.2

$$\int_1^{1.5} f(x) \; dx = \frac{1.5-1}{2} \int_{-1}^{1} f\left(\frac{1.5-1}{2}z + \frac{1+1.5}{2}\right) \; dz = \frac{1}{4}\int_{-1}^{1} f\left(\frac{x+5}{4}\right) dx. \tag{C.6}$$

Then applying 2×2 Gauss-quadrature sampling points and Eq. C.1 or C.3, we have

$$\int_1^{1.5} f(x)\, dx \approx \frac{1}{4}\left\{ \left[\left(\frac{-\frac{\sqrt{3}}{3}+5}{4} \right)^2 \ln\left[2\left(\frac{-\frac{\sqrt{3}}{3}+5}{4} \right) \right] + \left(\frac{\frac{\sqrt{3}}{3}+5}{4} \right)^2 \ln\left[2\left(\frac{\frac{\sqrt{3}}{3}+5}{4} \right) \right] \right\} = 0.7410. \tag{C.7}$$

Analytical solution is

$$\int_1^{1.5} x^2 \ln 2x\, dx = \left. \frac{x^3 \ln 2x - 1/3}{3} \right|_1^{1.5} = 0.7410. \tag{C.8}$$

D. VERIFICATION OF THE HOMOGENIZED ELASTIC TENSOR

D.1 MATLAB® Program `HOMOG`

An off-the-shelf program (`HOMOG`) for computing the effective elastic matrix was written in MALTAB® based on the techniques discussed in the previous two appendices. The main program is called from the MATLAB® prompt by the line

$$[\mathrm{Ch}, \mathrm{dCh11}, \mathrm{dCh12}, \mathrm{dCh22}, \mathrm{dCh66}] = \mathrm{HOMOG}(\mathrm{E0}, \mathrm{nu}, \mathrm{y}, \mathrm{penal})$$

and the parameters corresponding to `HOMOG` are listed in Table D.1.

D.2 Soft and Hard Isotropic Composite Materials

The homogenized elastic tensor, C^{H}_{ijkl}, was computed by `HOMOG` and compared with the results from [2]. For the first example, the base cell consists of two different materials. The soft materials have Young's modulus $\mathrm{E}_{soft} = 10$ and the hard materials have Young's modulus $\mathrm{E}_{hard} = 1000$ and both of them have same Poisson's ratio $\nu = 0.30$. The base cell is illustrated in Fig. D.1. The comparison of the homogenized elastic tensor is shown in Tab. D.2.

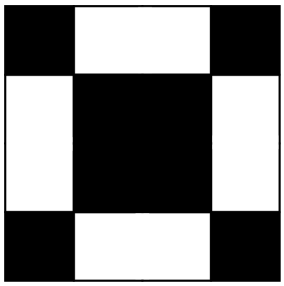

Figure D.1. Structure of example 1.

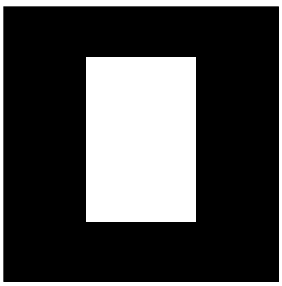

Figure D.2. Structure of example 2.

Table D.1. List of parameters in `HOMOG`.

Input variables	**Description**
`E0`	base material Young's modulus
`nu`	base material Poisson's ratio
`y`	unit cell density distrituion
`penal`	penalization power
Output variables	**Description**
`Ch`	homogenized elastic matrix
`dCh11`	first components of derivatives of homogenized elastic matrix with respect to design variable $y_j,\ j = 1, \ldots, n$
`dCh12`	second components of derivatives of homogenized elastic matrix with respect to design variable $y_j,\ j = 1, \ldots, n$
`dCh22`	third components of derivatives of homogenized elastic matrix with respect to design variable $y_j,\ j = 1, \ldots, n$
`dCh66`	fourth components of derivatives of homogenized elastic matrix with respect to design variable $y_j,\ j = 1, \ldots, n$

Table D.2. The comparison of the homogenized elastic tensor: soft and hard materials.

Mesh	C_{11}^{H}	C_{12}^{H}	C_{22}^{H}	C_{66}^{H}
16×16 [2]	149.80	71.61	149.80	87.12
1^{st} Adapt [2]	127.12	62.91	127.12	75.90
2^{nd} Adapt [2]	125.79	62.62	125.79	75.28
`HOMOG` (16×16)	149.80	71.61	149.80	87.13

D.3 Unit Cell with Rectangular Hole in the Center

For verification of HOMOG, the second case is a rectangular hole in the central with 0.4×0.6 as shown in Fig. D.2 with material properties $C_{11} = C_{22} = 30$ and $C_{12} = C_{66} = 10$. The comparison is shown in Tab. D.3

Table D.3. The comparison of the homogenized elastic tensor: unit cell with rectangular hole.

Mesh	C^{H}_{11}	C^{H}_{12}	C^{H}_{22}	C^{H}_{66}
20×20 [2]	13.02	3.24	17.55	2.79
1^{st} Adapt [2]	12.91	3.18	17.47	2.71
2^{nd} Adapt [2]	12.87	3.15	17.44	2.68
3^{rd} Adapt [2]	12.84	3.13	17.42	2.67
HOMOG (20×20)	13.06	3.26	17.58	2.81